Tectono-metamorphic history of the reworked, high-grade Maud Belt at central-Eastern H.U. Sverdrupfjella, Antarctica

Gregory Byrnes

Supervised by Dr J. F. A. Diener and co-supervised by Dr Å. Fagereng

a dissertation submitted for the degree of
Master of Science
at the University of Cape Town, Cape Town,
South Africa

2015

The financial assistance of the National Research Foundation (NRF) towards this research is hereby acknowledged. Opinions expressed and conclusions arrived at, are those of the author and are not necessarily to be attributed to the NRF.

Abstract

The reworking of granulites by amphibolite- to granulite-facies metamorphism can complicate the interpretation of their geological history because the event that reached higher peak P-T conditions will either completely overprint earlier peak assemblages or prevent the formation of new 'peak' minerals. The extent of reworking in granulites is controlled by three main factors, namely: (1) the pressures and temperatures reached in earlier and later metamorphic events, (2) the extent of deformation during subsequent events, and (3) the amount of fluid influx into the system during subsequent metamorphic events. Extensive reworking will occur if the peak temperature of the later event exceeds that of the earlier event, but if it does not, reworking will be less pervasive, and restricted to areas of deformation and/or fluid influx. The Salknappen nunatak in central-Eastern H.U. Sverdrupfjella, Antarctica forms a part of the high-grade Maud Belt that was formed by a granulite facies Grenvillian orogeny and was variably overprinted by high-grade metamorphism (eclogite to amphibolite facies) during the Pan-African orogeny. The degree of reworking during the Pan-African has been a contentious issue for some time, with early workers assigning the metamorphic peak to the Grenvillian, whereas others assigned it to the Pan-African.

Mineral assemblages and textures preserved in metapelitic and metamafic rocks preserve evidence of only one prograde to retrograde metamorphic cycle with peak mineral assemblages that are characteristic of granulites. Sillimanite in metapelitic rocks forms pseudomorphs after kyanite whereas garnet breakdown microstructures and in both metapelitic and metamafic rocks formed as a result of near-isothermal decompression. Garnet and hornblende display retrograde zoning profiles whereas retrograde cummingtonite, hornblende, plagioclase and ilmenite in metamafic rocks moderately constrain retrograde conditions. Pseudosection modelling with THERMOCALC on peak mineral assemblages from metapelitic and metamafic samples collected at Salknappen provides a robust peak P-T estimate (M1) of 760 – 790 ºC at 8.5 – 10 kbar. Phase diagram modelling of more subtle retrograde assemblages constrain retrograde metamorphic conditions (M2) to between ~550 – 750 °C and ~2 – 5 kbar. Both M1 and M2 likely occurred during the Grenvillian in a single orogenic cycle along a clockwise metamorphic path, where peak metamorphism was followed by near-isothermal decompression of ~5 kbar. Recrystallised quartz in melt leucosomes confirms that retrogression (M2) occurred after peak metamorphism. M2 was followed by the intrusion of megacrystic leucogranite dykes that most likely formed during the Pan-African in response to

melt migration as a result of melting deeper in the crust. These dykes and earlier gneisses were intruded by the Dalmation granites at c. 470 Ma, at which point the Salknappen nunatak was at crustal conditions approximating the brittle-ductile transition.

The study area in central-Eastern H.U. Sverdrupfjella preserves the peak and retrograde metamorphic assemblages from the Grenvillian orogeny and does not display evidence of reworking by a later granulite facies event. Salknappen does not display evidence of reworking during the Pan-African because peak metamorphism did not exceed peak temperatures attained during the Grenvillian orogeny and also did not form discrete, localised deformation zones with a significant influx of fluid during the Pan-African orogeny. This study presents a case where the effects of mid-crustal reworking by a high-grade metamorphic event are not shown due to the lack of rehydration, pervasive deformation and an elevated residuum solidus as a result of higher peak temperatures in an earlier granulite facies metamorphic event. When working with polymetamorphic terranes that have been subjected to more than one granulite facies orogenic cycle, the interpretation of the geological history of such an area should be done with caution and P-T estimates should be done with methods that are less affected by the long retrograde histories.

Acknowledgements

The author would like to acknowledge the National Research Foundation (NRF) for sponsoring the field trip to Antarctica and for providing the funding needed to initiate the Master's programme at the University of Cape Town and would also like to express his gratitude in receiving the Research Associateship Award and additional funding support from the University of Cape Town to further studies in this project. Opinions expressed and conclusions arrived at, are those of the author and are not necessarily to be attributed to the NRF or the University of Cape Town.

The author is also extremely thankful for the support received by Dr Diener. I am in particular thankful for Dr Diener's critical feedback, his support with preparation for the field, on-going support throughout the year and for his approach to challenges encountered throughout the lifespan of this project. Dr Fagereng is also thanked for his on-going support, advice and feedback throughout the duration of the project. I am extremely privileged to have had the opportunity to work with both of these talented academics.

I would also like to thank the 2013/2014 SANAP take-over personnel for providing the logistical support needed to carry out the research and data collection for this project. In particular, I would like to thank Dr Geoff Grantham for accommodating me on this trip and for the lengthy, insightful discussions about the geology of the Antarctica. I learnt a lot from Dr Grantham's wealth of knowledge and experience in the region. Mike Knoper and Erasmus Burger are also thanked for their support in the field.

Plagiarism Declaration for Master of Science Dissertation: Tectono-metamorphic history of the reworked, high-grade Maud Belt at central, Eastern H.U. Sverdrupfjella, Antarctica.

According to the Merriam-Webster Online Dictionary, to "plagiarize" means

- to steal and pass off (the ideas or words of another) as one's own
- to use (another's production) without crediting the source
- to commit literary theft
- to present as new and original an idea or product derived from an existing source.

In other words, plagiarism is an act of fraud. It involves both stealing someone else's work and lying about it afterwards.

Please read this and sign:

1. Plagiarism is to use another's work and to pretend that it is one's own. I know that plagiarism is wrong.
2. I have used a standard (Harvard) referencing convention for citation and referencing. Each significant contribution to, and quotation in, this submission from the work, or works of other people, has been attributed, and has been cited and referenced.
3. This submission is my own work.
4. I have not allowed, and will not allow anyone to copy my work with the intention of passing it off as his or her own work.
5. I acknowledge that copying someone else's submission, or part of it, is wrong, and declare that this is my own work.

Name: Gregory

Surname: Byrnes

Student No: BYRGRE002

Course: GEO5000W (MSc Geology)

Date: 30-01-2015

Signature:

Contents

1. Introduction

Antarctica contains a vast geological history that contributes to the understanding of the evolution of ancient and more recent supercontinents - Rodinia and Gondwana, (e.g. Harley *et al.*, 2013). Various studies throughout Antarctica have focussed on the tectono-metamorphic histories, configuration and ages of collision zones that were formed during the formation of various supercontinents to assist with supercontinent reconstruction (du Toit, 1937; Dalziel, 1992; Fitzsimons, 2000; Jacobs *et al.* 2003) or to understand the extent of deformation and metamorphism related to specific orogenic events (Grantham *et al.*, 1995; Moyes and Groenewald, 1996; Jacobs *et al.* 1998; Board *et al.*, 2005; Liu *et al.*, 2013). These interpretations are typically more complicated in high-grade polymetamorphic regions that have been subjected to more than one orogenic event, (e.g. Dasgupta *et al.*, 2001; Diener *et al.*, 2008; Phillips *et al.*, 2009). The complications are caused by the difficulty of assigning peak metamorphic assemblages, compositions and ages to a particular event; particularly since the protolith composition can be significantly modified through melt loss between the two high grade events and the peak composition of minerals can further be altered during the long retrograde history following the final high grade event (Harley *et al.*, 1992; Goscombe *et al.*, 1998; Hand and Buick, 2001; White and Powell, 2002).

The Maud Belt in East Antarctica formed at *c.* 1000 Ma in response to a high grade orogenic event that produced granulite-facies metamorphism during the assembly of Rodinia and was reworked during the Gondwana amalgamation (Fitzsimons, 2000 and references therein). Studies have revealed that the overprint of a high grade Neoproterozoic event is generally pervasive in central Dronning Maud Land in the Prydz Belt and Lützow Holm Belt (Shiraishi *et al.*, 1994; Fitzsimons, 2000; Liu *et al.*, 2013), whereas the Maud Belt in western Dronning Maud Land largely preserves the effects of the Mesoproterozoic tectono-metamorphic event; however, recent studies on the Maud Belt in western Dronning Maud Land have suggested that the overprint of the Neoproterozoic event is more pervasive than previously thought (Moyes and Groenewald, 1996; Board *et al.*, 2005). The extent of the tectono-metamorphic overprint of the Neoproterozoic event in the Maud Belt still remains a contentious issue and studies are further complicated by intermittent outcrop exposure due to ice cover in the region. Reworking during the Neoproterozoic was followed by a period of extension during the break-up of Gondwana (Fitzsimons, 2000). This study addresses the issues related to determining the metamorphic histories in an area that was subjected to more than one high grade metamorphic

event and uses a combination of structural and metamorphic constraints to elucidate the geological history at the Salknappen nunatak in Eastern H.U. Sverdrupfjella, Antarctica.

1.1 Aims of this study

The characteristics of high-grade metamorphism in regions subjected to orogenesis are fairly well understood and have been reviewed in detail, (e.g. Brown, 2001); however, the effects of more than one orogenic event on high grade metamorphic terranes has not been studied in as much detail. This study reviews polymetamorphism in the mid- to lower-crust where medium- to high pressure and temperature conditions prevail. It also reviews how structural events and an accurate pressure-temperature evolution derived from more updated and reliable methods can assist in reconstructing a metamorphic history. Additionally, the study will review factors that control reworking during polymetamorphism and will point out the uncertainty involved with deciphering geological histories in reworked high grade metamorphic terranes.

By focusing on the Salknappen nunatak situated in Eastern H.U. Sverdrupfjella – a part of the reworked high grade Maud Belt in Eastern Antarctica – this study uses a combination of structural and metamorphic observations to investigate the tectono-metamorphic history at Salknappen. The orientations of lithology contacts, foliations, lineations, intrusions and their temporal relationships to one another will be used to infer the kinematics of deformation. On a smaller scale, the study attempts to use microstructures and in particular quartz microstructures to estimate the flow stress in the crust during peak metamorphism as well as the effect of large competent lenses on the dynamically recrystallised grain sizes of quartz during peak metamorphism. Quartz microstructures will also be used to comment on the likelihood of retrogression after peak metamorphism.

The main focus of this work will be the metamorphic history of Salknappen because metamorphic data can provide more accurate constraints on the geological history in the area. Peak and retrograde assemblages will be inferred by using a combination of mineral chemistries and microstructural relationships on selected metapelitic and metamafic samples. Calculated pseudosections will be used to quantify pressure-temperature conditions and derive a better constrained pressure-temperature for the area. These results will be discussed in relation to previous studies in the Sverdrupfjella area of the Maud Belt.

Finally, the study will comment on the likely timing of metamorphism in the area and attempt to reconstruct a geological history, or at least parts thereof, for the central part of Eastern H.U. Sverdrupfjella.

2. Theoretical background on high-grade polymetamorphism and structural aspects used to elucidate deformation history

This study investigates poly-metamorphic and deformed mid-crustal rocks and it is therefore necessary to introduce fundamental concepts related to these topics to facilitate the discussion. The extent of crustal *reworking* (Holdsworth *et al.*, 2001) and the conditions required to rework high-grade rocks during subsequent metamorphic events is the main focus of this project and will therefore be reviewed in more detail. The main aspects of orogenic metamorphism will also be introduced briefly.

2.1 Characteristics of orogenic metamorphism

Orogenesis occurs during the collision of two convergent margins and is characterised by a substantial thickening and heating of the continental crust within the collision zone as the convergent margins are thrust upon one another (Jamieson and Beaumont, 2013). Different stages of orogens (i.e. large hot orogens, transitional orogens and small cold orogens) occur in collision zones and the P-T conditions of each stage varies markedly (Jamieson and Beaumont, 2013). Ultimately, orogenesis results in substantial burial of the lithologies at the base of the orogeny, with burial typically occurring faster than the rocks can thermally equilibrate. Therefore peak pressures are reached before peak temperatures resulting in a characteristic clockwise P-T path, as shown in Figure 2.1 (England and Thompson, 1984).

Crustal thickening has a profound effect on the crustal strength, since crustal thickening is typically accompanied by an increase in heat flux in the orogenic zone and subsequent partial melting of the rock mass deep in the crust (Brown, 2001). An increase in heat flow and possible introduction of a melt phase in the lower crust significantly weakens the crust and results in a period where crustal thickening can no longer be accommodated (Dewey, 1988). This period typically coincides with peak metamorphism. Once the weakened orogen can no longer sustain the mass of the overburden, the orogen is characterised by a period of collapse and exhumation (Dewey, 1988). Orogenic collapse causes a rapid unloading of the crustal lithosphere and rapidly reduces the pressures exerted on the rocks being exhumed faster than they can be thermally equilibrated. This near-isothermal decompression (Fig. 2.1) occurs rapidly and reduces the pressures at about 0.05 – 0.2 kbar / C° (England and Thompson, 1984).

During orogenesis, there is a period where no thickening or collapse occurs. This is followed by a period of orogenic collapse and exhumation, the granulites that formed at the base of the orogeny evolve through a clockwise P-T path (Fig. 2.1), (Brown, 2001).

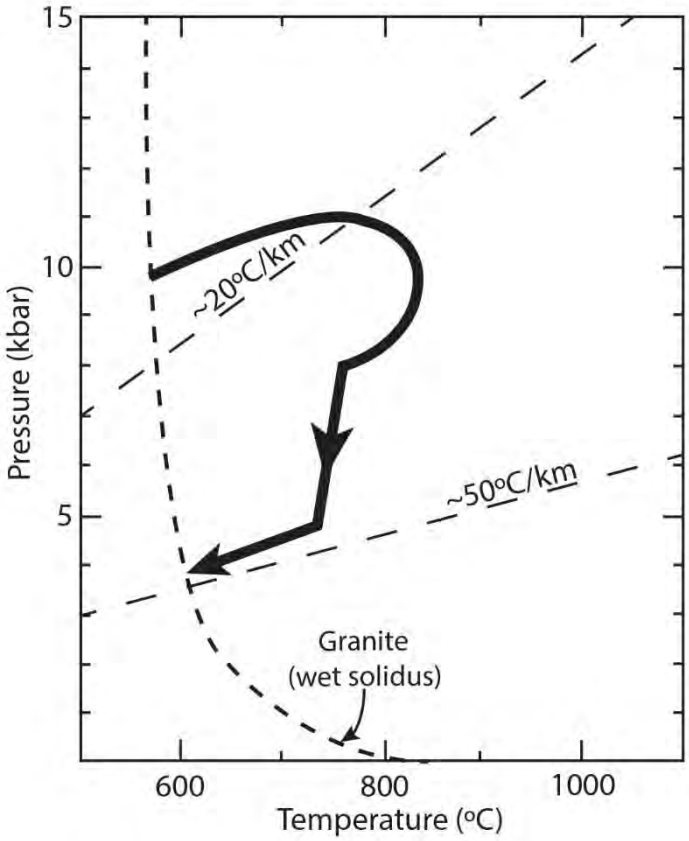

Figure 2.1: Schematic P-T path typical of an orogenic tectonic setting characteristic of lower granulite facies metamorphism followed by near-isothermal decompression. Note: Peak metamorphism is characterised by P-T conditions well into the anatectic zone (above the wet solidus). Diagram modified after Brown (2001).

2.2 Polymetamorphism and reworking of the mid- to lower-crust

Granulite facies metamorphism formed through orogenic events will be focussed on in more detail because in possible polymetamorphic terranes the orogenic zones are preferentially reactivated and reworked. This is because pre-existing fabrics – common in orogenic fronts, can form weaknesses, which can lead to preferred areas for subsequent metamorphism, (e.g. Ring, 1994; Vauchez *et al.*, 1997).

In terranes that have only been subjected to one high grade metamorphic event the rock fabrics, metamorphic assemblages and collection of isotopic dates obtained are relatively simple to interpret when compared to the difficulties associated with disentangling subsequent

metamorphic events with earlier ones, (e.g. Board *et al.* 2005; Sarkar *et al.* 2007; Dutch *et al.* 2010). Difficulties in interpreting the geological history in these reworked terranes stem from the fact that subsequent orogenies in the same region can completely overprint (e.g. Board *et al.*, 2005; Sommer *et al.*, 2005; Bisnath *et al.*, 2006), partially overprint, (e.g. Dziggel *et al.* 2012) or have little effect (e.g. Harley *et al.,* 1992), on high grade assemblages formed from earlier tectonic episodes. This depends on the similarity of the peak P-T conditions for both events as some minerals can be preserved better than others (e.g. Cross, 2013) and is also dependent on the extent of deformation (Tenczer *et al.*, 2006; Diener *et al.*, 2008) and fluid infiltration (Watson, 1973; Tenczer *et al.*, 2006) during subsequent metamorphic events.

2.2.1 Methods used to reconstruct geological histories in reworked terranes

Attempts to reconstruct geological histories have involved using a combination of geological techniques that include looking at structures (Watson, 1973; Goscombe, 1992; Sarkar *et al.*, 2007; Dutch *et al.*, 2010; McGibbon, 2014), metamorphic histories (Scrimgeour and Raith, 2001; Zhao *et al.*, 2001; Sarkar *et al.*, 2007; Dutch *et al.*, 2010; Dziggel *et al.*, 2012) and isotopic dating (Shaw *et al.*, 1997; Manhica *et al.* 2001; Parrish, 2001; Simmat and Raith, 2008; Geng *et al.*, 2012). Although some authors have exclusively used one method to elucidate the geological history of an area, i.e. isotopic dating (Geng *et al.*, 2012), others have used a combination of methods, (e.g. Board *et al.* 2005; Dutch *et al.* 2010). Each of these methods has advantages to determining to geological history of a polymetamorphic terrane but could also have several drawbacks, depending on the nature of each of the tectonic episodes.
This study combines metamorphic and structural aspects to piece together a geological history and therefore their application to reworked terranes will be reviewed in more detail.

2.2.1.1 Structural reconstruction

In high-grade polymetamorphic terranes, the geometry of fabrics and structures from earlier tectonic events can be overprinted by subsequent events. If the structures and fabrics related to the overprinting event have markedly different geometries to earlier events, they are easily distinguishable, (e.g. Sarkar *et al.*, 2007); however, where the geometry of structures from both events are similar it is challenging to identify which fabrics are related to a specific event. In the case of the Maud Belt this is particularly challenging because the dominant fabrics and

large-scale structures have similar orientations and are defined by the same mineral assemblages (Grantham *et al.*, 1995; McGibbon, 2014).

2.2.1.2 Reconstruction by investigating the metamorphic history

The metamorphic histories in granulites have been unravelled in the past using conventional thermobarometry, and more recently, pseudosections. Conventional thermobarometry relies on the actual preserved composition of minerals to be able to make any P-T estimate. The problem with this is that the composition of minerals in an exhumed metamorphosed rock is typically not a reflection of the composition that the minerals were at peak metamorphic conditions in granulite facies rocks where there is a longer cooling history and therefore more time to allow retrogression to occur (Harley *et al.*, 1992; White and Powell, 2002; 2010). Therefore, the peak mineral compositions need to be estimated in granulite facies minerals that are used to estimate P-T conditions through conventional methods and consequently creates large uncertainties when calculating the metamorphic history of rocks.

Calculated pseudosections are more useful and potentially a lot more precise than conventional methods because they graphically portray a map of stable mineral assemblages as fields in P-T space that can easily be related to reaction microstructures, overprinting criterion over various P-T ranges (Kelsey, 2008; Powell and Holland, 2008). Pseudosections also do not require original mineral compositions to be able to construct a phase diagram for a particular rock – they rely only on the bulk composition of a particular equilibration volume (Powell and Holland, 2008). Therefore pseudosections are a particularly useful tool to estimate peak P-T conditions in granulites and polymetamorphic rocks because the peak composition of minerals are seldom preserved.

A combination of conventional methods and more recently, pseudosection modelling have been used to reconstruct P-T paths and the geological histories of granulite facies terranes that have been reworked at amphibolite or granulites facies P-T conditions (Harley *et al.*, 1992; Board *et al.*, 2005; Scrimgeour, 2005; Sarkar *et al.*, 2007; Diener *et al.*, 2008; Dutch *et al.*, 2010; Thomas, 2014). Unravelling the evolution of polymetamorphic rocks using a metamorphic approach requires the preservation of metamorphic assemblages, textures and compositions indicative of P-T conditions for each metamorphic event. These methods have been employed on several reworked, high-grade metamorphic terranes; however, little work

has been done on the factors that are thought to control the extent of reworking in granulites, which will be briefly elaborated on in the next section.

2.2.2 Controls on the extent of reworking in high-grade rocks

The degree of reworking of the crust in subsequent metamorphic events is dependent on several factors that include: the water content in the rock during reworking (Watson, 1973; Tenczer *et al.*, 2006), the degree of deformation (Tenczer *et al.*, 2006; Diener *et al.*, 2008), the amount of melt loss during the earlier metamorphic episodes (White and Powell, 2002) and the peak P-T conditions reached during each event (Diener *et al.*, 2008).

An increase in pressures and temperatures to high grades is accompanied by dehydration reactions and the loss of H_2O from rocks (Connolly, 1997; Guiraud *et al.*, 2001); however, small amounts of water can still be chemically bound in hydrous minerals, even at ultrahigh temperature conditions (e.g. Kelsey, 2008). The devolatilisation of rocks during the prograde history precludes or inhibits the re-equilibration of minerals during retrogression or a subsequent metamorphic event unless a volatile phase is re-introduced from an external source, (e.g. Tenczer *et al.*, 2006; Diener *et al.*, 2008; Dziggel *et al.*, 2012). The addition of water to rocks that have been subjected to granulite facies metamorphism assists with the re-equilibration of minerals during reworking (Watson, 1973; Van Reenen *et al.*, 1987; Guiraud *et al.*, 2001).

Although the addition of a volatile phase assists with reworking, it is not always necessary to rehydrate the rock to re-equilibrate the minerals. This can also be achieved through recrystallisation as rocks are strained in response to deformation, (e.g. Tenczer *et al.*, 2006; Diener *et al.*, 2008). The formation and preservation of granulites in pelitic rocks in an orogenic environment is characterised by partial melting and melt loss (e.g. Fyfe, 1973; Sawyer, 2001; White and Powell, 2002). A consequence of substantial melt loss, where 50-70 % (White and Powell, 2002) of the melt produced is lost, is that more volatiles are removed from the system. Consequently, granulites that had significant amounts of melt removed preserve mineral assemblages formed at near-peak metamorphic conditions where the melt was extracted. Peak assemblages are well preserved in most granulites exposed at the Earth's surface today (Brown, 2002).

A consequence of forming dry, refractory granulites is that subsequent metamorphic events need to fulfil certain requirements in order to re-equilibrate or partially re-equilibrate the granulite mineral assemblages. Other than partially rehydrating the rocks, they can also be deformed (Tenczer *et al.*, 2006; Diener *et al.*, 2008); however, deforming granulites is difficult because melt removal strengthens granulites by 50-400 % when compared to unmelted, amphibolite-facies rocks of similar composition (Diener and Fagereng, 2014).

It is intuitive that re-equilibration could be achieved if subsequent metamorphic events reach P-T conditions similar to or greater than those where partial melting stopped in the previous granulite-forming event (e.g. Vielzeuf *et al.*, 1990). This would once again introduce melt into the system and significantly weaken the rocks (e.g. Paterson, 2001; Diener and Fagereng, 2014) and therefore assist with the re-equilibration of minerals during the reworking of older granulites. Should subsequent metamorphic events subject the granulites to higher pressures and temperatures than earlier metamorphic events, the later metamorphic mineral assemblages could completely overprint granulite facies mineral assemblages formed during earlier events (Board *et al.*, 2005); however if subsequent metamorphic events did not attain pressures and temperatures as high as earlier events, then the later event would not re-equilibrate the mineral assemblages (e.g. Harley *et al.*, 1992).

This complicates the interpretation of reworked metamorphic terranes where an area has been subjected to multiple high-grade metamorphic events because the mineral assemblages preserved could reflect either the first event or any subsequent event thereafter.

2.3 Introduction to concepts used to describe the deformation history

Piecing together a deformation history of an area involves looking at the scale, geometry and kinematics of structures, i.e. rock fabrics and the cross-cutting relationships between various structures.

2.3.1 *Deformation mechanisms in the mid to lower crust*

In the mid to lower crust, deformation is accommodated by quasi-plastic mechanisms that include dislocation creep and diffusive mass transfer (Passchier and Trouw, 2005). A combination of laboratory and field studies have been done on quartz aggregates to understand the development of quartz microstructures at different conditions (Hirth and Tullis, 1992; Hirth *et al.*, 2001; Stipp *et al.*, 2002a; Stipp *et al.*, 2002b). Quartz microstructures indicative of viscous deformation by dislocation creep can be classified into three main *regimes*, namely regimes 1, 2 and 3 (Hirth and Tullis, 1992). The dynamic recrystallisation of quartz in each regime has different mechanical properties, occurs at different temperatures (Fig. 2.2), different strain rates, and is characterised by different grain sizes and flow stresses (Fig. 2.2), (Hirth and Tullis, 1992; Stipp *et al.*, 2002a; Stipp and Tullis, 2003).

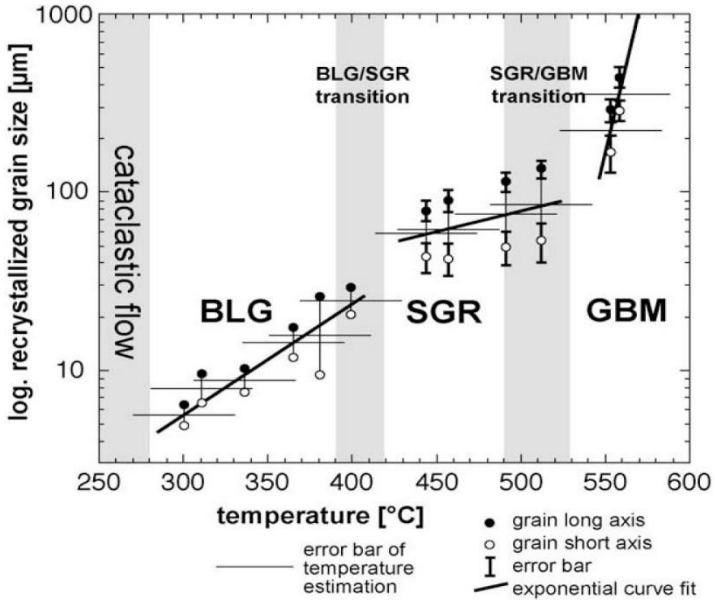

Figure 2.2: A plot of temperature versus recrystallised grain size highlighting the different dislocation creep deformation mechanisms. Image source: (Stipp *et al.*, 2002b).

In regime 1, quartz is deformed by bulging recrystallisation (BLG) whereas quartz is deformed by subgrain rotation (SGR) and grain boundary migration (GBM) in regimes 2 and 3 (Fig. 2.2). The transition from regime 1 to regime 3 occurs at increased temperatures or reduced strain

rates to produce larger recrystallised grain sizes (Fig. 2.2), (Hirth and Tullis, 1992; Stipp *et al.*, 2002b).

Once a melt phase is introduced into the rock at higher temperatures, deformation by dislocation creep is no longer applicable and the rock deforms by diffusion creep, (e.g. Paterson, 2001).

2.3.2 Stresses and strength in the crust derived from microstructures

Stresses close to the Earth's surface in the brittle crust can be measured directly close to the Earth's surface whereas stresses in the deeper, dominantly viscous crust have been inferred from a various methods that includes experimental rock deformation tests at a range of P-T conditions (e.g. Hirth and Tullis, 1992; Dunlap *et al.*, 1997; Stipp *et al.*, 2002a) on samples collected from the field (e.g. Stipp *et al.*, 2002b). These studies typically use the dynamically recrystallised grain size of quartz as a proxy for the differential stress under which the quartz recrystallised – these are termed 'grain size piezometers' (Stipp and Tullis, 2003). In quartz that has been dynamically recrystallised, an increase in grain size corresponds to a decrease in *flow stress*, i.e. stress when deformation occurs at a constant strain rate (Fig. 2.3).

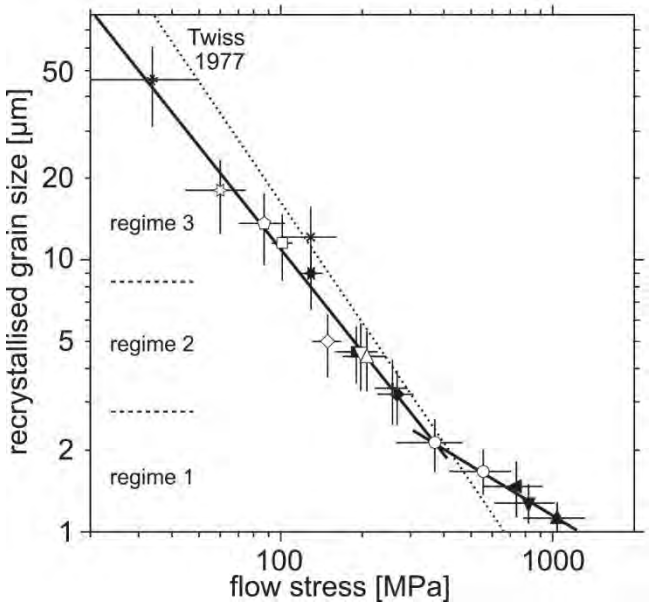

Figure 2.3: Grain size piezometer for quartz modified after Stipp and Tullis (2003). Piezometer from Twiss (1977) is included for comparison.

The grain size piezometer for quartz in Figure 2.3 is only applicable for rocks that do not contain melt. When melt is introduced into a rock, it will significantly weaken the rocks as long as a melt phase is present (Diener and Fagereng, 2014; and references therein). The addition of

a melt phase into high grade rocks also has an impact on the deformation mechanisms that accommodate strain.

2.3.3 Melt transport in the crust and formation of melt pathways

Melt is formed in the mid to lower crust in response to partial melting and is typically transported to higher levels in the crust where it cools down and is emplaced (Petford *et al.*, 2000). After melt segregation, melt is transported away from its source in a pervasive melt network in response to forces driven by buoyancy and dilatancy (Vanderhaeghe, 2001). In the viscous crust, rocks dilate in response to an increase in melt pressure as melt volumes build up prior to instantaneous fracturing (Davidson *et al.*, 1994). As the melt migrates further up the crust, the crustal temperatures decrease forcing melt flow to be more focused in larger conduits because melt in small, narrow conduits will freeze at lower temperatures. Large conduits exist in dykes (Petford *et al*, 1993) or shear zones (Brown and Solar, 1998a), depending on where it is easiest for the melt to pass through. Dykes can also form parallel to pre-existing weaknesses such as foliations, mineral lineations and bedding planes (Hutton, 1988; Weinberg, 1999), otherwise they will form as new fractures are formed through melt-enhanced embrittlement (Davidson *et al.*, 1994; Brown and Solar, 1998a). If the melt ceases to rise further it is emplaced in the crust along structural or rheological traps (Petford *et al.*, 2000).

If in an orogenic setting we assume that rocks in the crust are homogenous and intact, dykes would propagate perpendicular to the minimum compressive stress - σ_3, (Brown and Solar, 1998b). Assuming that dykes are formed in an Andersonian stress regime (Anderson, 1951), then in an orogenic setting (where σ_3 is vertical) dykes would be subhorizontal and in an extensional setting (where σ_3 is horizontal) they would be subvertical. In reality, rocks are not isotropic and may contain pre-existing fabrics that make them anisotropic, e.g. a strong foliation formed in crustal-scale shear zones. Melt can also be transported within areas of relative dilation in pre-existing weaknesses to form strain-related melt-bearing structures if the melt pressure is high enough to facilitate temporary embrittlement and the formation of shear or tensile fractures (Brown and Solar, 1998b).

3. Regional geology of western Dronning Maud Land

Western Dronning Maud Land in East Antarctica comprises the Mesoproterozoic and Neoproterozoic Maud Belt along with the Archaean Kaapvaal-Grunehogna Craton which is mostly covered by low-grade supracrustals (Fig. 3.1).

The Maud Belt is the focus of this study and is a NE-SW-trending, high-grade polymetamorphic terrain that borders the eastern margin of the Jutulstraumen – Pencksökket glacier field (Fig. 3.1). Early work in Western Dronning Maud Land (WDML) identified the Maud Belt as a high grade metamorphic terrane that formed at *c.* 1000 Ma (Wolmarans and Kent, 1982; Grantham et al., 1988). Later investigations in the region revealed that a major thermal thermotectonic event could overprint the *c.* 1000 Ma event at *c.* 500 Ma (Moyes et al., 1993; Bisnath and Frimmel, 1995; Grantham et al., 1995; Groenewald et al., 1995; Jacobs et al., 1995; Harris, 1999; Jackson, 1999; Golynsky and Jacobs, 2001; Board et al., 2005).

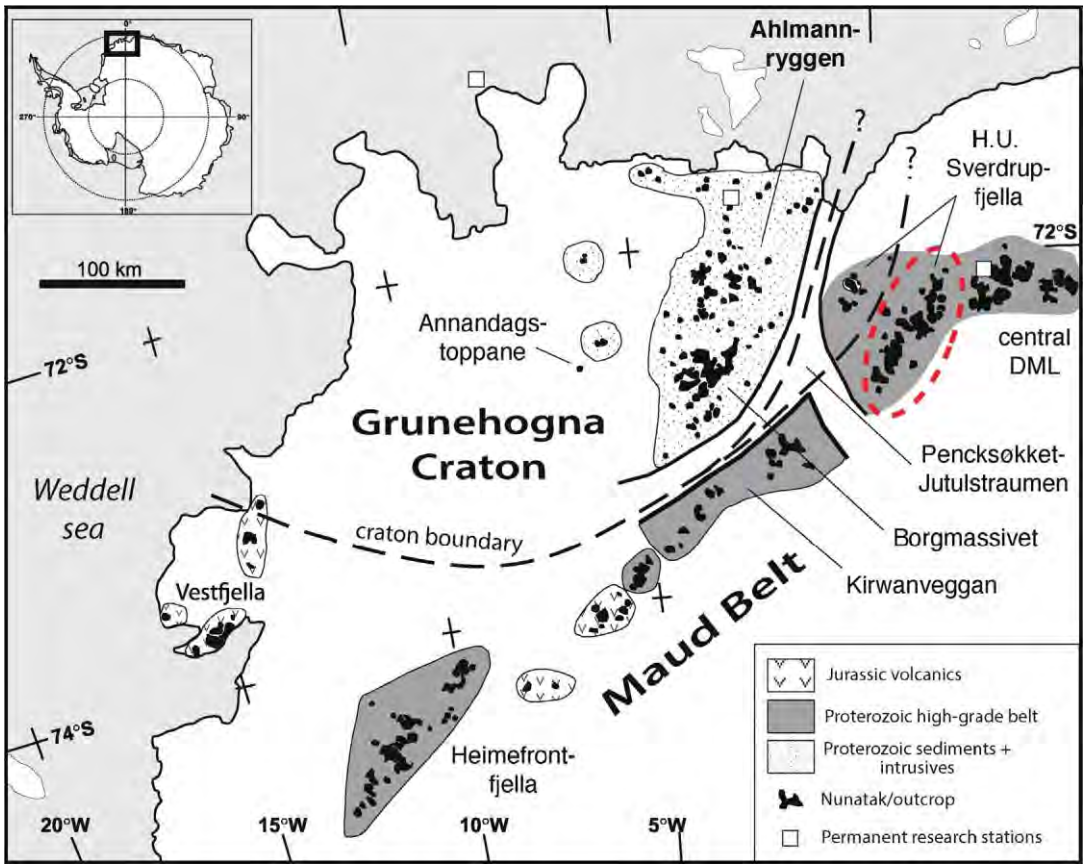

Figure 3.1: Map showing the location of important geological terranes in western Dronning Maud Land. Eastern H.U. Sverdrupfjella is situated within the red dashes. Image modified after Marschall et al. (2013).

The geology of the Grunehogna Province and terranes in the Maud Belt will be described briefly before the history of H.U. Sverdrupfjella will be reviewed in more detail. Focus will be placed on the lithologies, structural framework and metamorphic history in H.U. Sverdrupfjella, as well as how our understanding of the geological history in the region has evolved.

3.1 Introduction to terranes surrounding H.U. Sverdrupfjella

3.1.1 Grunehogna Province

The Grunehogna Province constitutes the oldest known rocks in the region and comprises the Archaean Grunehogna Craton basement which is overlain by the Mesoproterozoic, low-grade Ritschersflya Supergroup. *c.* 3000 Ma granites (Halpern, 1970; Barton *et al.*, 1987; Marschall *et al.*, 2010) only found at a confined outcrop at Annandagstoppane were inferred to represent the Grunehogna Craton basement (Wolmarans and Kent, 1982). The Grunehogna Craton is a fragment of the Kalahari Craton that became detached during the break-up of Gondwana (Martin and Hartnady, 1986; Groenewald *et al.*, 1991; Jacobs *et al.*, 1993; Krynauw, 1996).

The Grunehogna Craton is largely concealed by the ~2000 m – thick Ritscherflya Supergroup (Wolmarans and Kent, 1982). The Ritscherflya Supergroup is comprised of the sedimentary Ahlmannryggen Group which is covered by the sedimentary-volcanogenic Jutulstraumen Group that was later intruded by syn-diagenetic mafic sills (Wolmarans and Kent, 1982; Moyes *et al.*, 1995; Curtis and Riley, 2003). These sediments were deposited in close proximity to an active volcanic arc that was formed by westward subduction along the eastern margin of the Kalahari-Grunehogna Craton (Grosch *et al.*, 2007; Grantham *et al.*, 2011; Marschall *et al.*, 2013). The age of the Ritscherflya Supergroup was constrained to be between 1135 Ma (Frimmel, 2004; Marschall *et al.*, 2013) and 1107 Ma (M. Knoper, unpubl. data). The Ritscherflya Supergroup has subsequently experienced low-grade sub-greenschist to greenschist metamorphic conditions and is relatively undeformed with layers generally dipping ~10º to the NE and SE (Wolmarans and Kent, 1982; Groenewald *et al.*, 1995). Steep, localised, N-S oriented, *c.* 525 Ma shear zones have been identified close to the Jutulstraumen glacier field and are ascribed to have formed due to collision during the *'Pan-African'* event (Peters *et al.*, 1991; Jacobs and Thomas, 2004).

3.1.2 The Maud Belt

The Maud Belt extends from Heimefrontfjella in the south-west, through the Kirwanveggen to H.U. Sverdrupfjella in the north-east between ~70ºS – 75ºS and ~15ºW – 03ºE.

Heimefrontfjella

Heimefrontfjella is characterised by three separate geological terranes (Kottas, Vardeklettane, Sivorg), that contain *c.* 1150 - 2000 Ma layered metasedimentary and metavolcanic gneisses that were intruded by *c.* 1130 Ma granitoids (Arndt *et al.*, 1991; Jacobs *et al.*, 1996; Jacobs *et al.*, 1999). The Kottas Terrane is made up of amphibolite-facies metavolcanics that were deposited in an island-arc environment, whereas the Vardeklettane Terrane mostly consists of orthogneisses and some quartzites that were deposited in close proximity to an older craton (Arndt *et al.*, 1991). The Sivorg Terrane is made up of a combination of metavolcanics and metasediments that were deposited in a back-arc basin (Jacobs *et al.*, 1996).

Kirwanveggen

The Kirwanveggen is divided into three main domains, namely: northern, central and southern Kirwanveggen (Wolmarans and Kent, 1982; Grantham *et al.*, 1995), and comprise *c.* 1130 Ma high-grade orthogneiss and paragneiss that were generated in an island arc environment (Wolmarans and Kent, 1982; Harris *et al.*, 1995; Harris, 1999; Jackson, 1999). High-grade gneisses were subsequently metamorphosed in discrete shear zones at *c.* 500 Ma during rapid exhumation (Harris, 1999). Low-grade metapelites that constitute the Urfjell Group predominantly make up the southern Kirwanveggen (Aucamp *et al.*, 1972; Wolmarans and Kent, 1982). Although the northern and central Kirwanveggen are generally characterised by discrete, moderately SE-dipping shear zones, several deformation episodes were identified by Grantham *et al.* (1995) based on structural grounds.

The northern Kirwanveggen is dominated by garnet-biotite migmatites interleaved by orthogneisses and intruded by megacrystic orthogneiss and amphibolite dykes. Kyanite and sillimanite are also locally present (Harris, 1999). Ferrar (1995) identified four major metamorphic events in the northern Kirwanveggen where peak conditions for Mesoproterozoic (*c.* 1000 Ma) metamorphic events M1 and M2 were estimated to be ~650-700 ºC at 12-13 kbar and ~720 ºC at 6-10 kbar, respectively. Harris (1999) estimated similar M2 (Mn+1) conditions to be to be between 710-760 ºC and 7.8-8.5 kbar; whereas M3 (Mn+2) conditions were approximated at 630-690 ºC and 6.0-7.4 kbar.

The central Kirwanveggen is similar to the northern section of the Kirwanveggen and is also made up of *c.* 1150 Ma (Wolmarans and Kent, 1982) garnet-biotite gneisses and orthogneisses that were later intruded by megacrystic orthogneiss and leucogranites. Rocks in the central Kirwanveggen have been metamorphosed to amphibolite facies conditions (Jackson, 1999). Discrete, top-to-NW shear zones with collinear fabric plunging shallowly to the SE are found in this region (Grantham *et al.*, 1995; Jackson, 1997).

The southern Kirwanveggen has a variety of lithological units that include *c.* 1000 Ma high-grade gneisses (Kleinschmidt *et al.*, 2000), Urfjell Group sediments and Jurassic lavas (Aucamp *et al.*, 1972; Harris *et al.*, 1990). The most prominent of these is the *c.* 500 Ma Urfjell Group that consists of relatively undeformed and unmetamorphosed sediments (Moyes *et al.*, 1997; Kleinschmidt *et al.*, 2000). Kleinschmidt *et al.* (2000) have suggested that the Urfjell Group was deposited as a result of the Pan African event at *c.* 500 Ma based on K-Ar and Ar-Ar ages.

3.2 The geology of H.U. Sverdrupfjella

Early work in H.U. Sverdrupfjella by Roots (1969) and Hjelle (1972) identified several lithological differences in the region (Fig. 3.2) which were expanded upon by Grantham *et al.* (1988). Sverdrupfjella is sub-divided into an eastern and western section based on lithology, peak metamorphic conditions and structural constraints (Groenewald and Hunter, 1991; Grantham *et al.*, 1995). The major lithologies and structures in Eastern and Western H.U. Sverdrupfjella will be described separately.

3.2.1 Lithologies in H.U. Sverdrupfjella

H.U. Sverdrupfjella is dominated by high-grade metamorphic rocks whereas ~10-20 % of the area comprises younger intrusions. This region is dominated by rocks from three gneiss complexes, namely the Jutulrøra, Fuglefjellet and Rootshorga Formations; the Jutulrøra Formation is overlain by the Fuglefjellet and the Rootshorga Formations (Fig. 3.3).

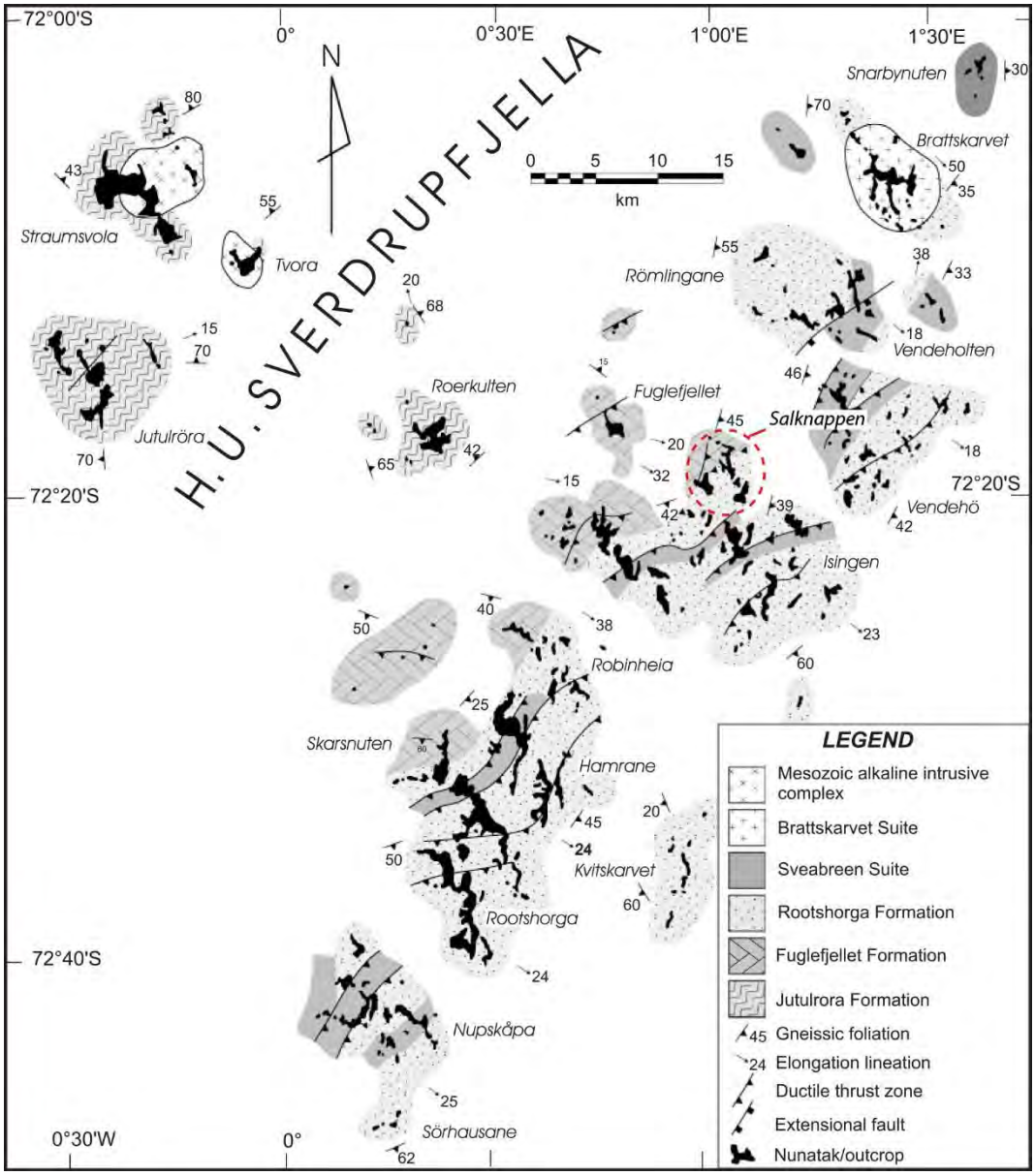

Figure 3.2: Geological map of H.U. Sverdrupfjella showing the various lithologies and structures. Red, dashed line shows the location of Salknappen. Image source: Board et al. (2005).

Western H.U. Sverdrupfjella is dominated by metavolcanic (Groenewald *et al.*, 1995), intermediate orthogneisses that are best exposed at Jutulrøra and also contains a prominent, ~300 m-thick calc-silicate package at Fuglefjellet. The stratigraphic framework in H.U. Sverdrupfjella was most recently revised by Grantham *et al.*, (1988) and Ohta (1996) and categorised the Jutulrøra Formation into a Grey Gneiss – and Banded Gneiss Complex (Fig. 3.3). The *c.* 1100-1150 Ma (Moyes and Barton, 1990) Grey Gneiss Complex is dominated by epidote-biotite-hornblende tonalitic gneisses that contain subordinate granitic orthogneisses. The Banded Gneiss Complex consists of interlayered amphibolites and quartzofeldspathic

gneisses that locally contain calc-silicate gneisses. The Fuglefjellet Formation is more prominent in the east close to the boundary between eastern and western H.U. Sverdrupfjella, and is dominated by marbles and calc-silicates that contain interleaved amphibolites, pelitic and quartzofeldspathic units.

These units are cross-cut by younger mafic intrusives, granitic dykes and sheets. The Dalmation granites (Grantham *et al.*, 1988) are medium-grained, leucocratic granites that intruded as <10 m-thick sheets both concordant and discordant to the foliation in the Jutulrøra Formation (Grantham *et al.*, 1988; Grantham *et al.*, 1991). The Straumsvola nepheline syenite complex and the Tvora alkaline complex constitute a relatively large portion of western H.U. Sverdrupfjella at Straumsvola and Tvora and intruded into the Jutulrøra Formation gneisses at *c.* 170-180 Ma as a result of the Gondwana break-up (Harris and Grantham, 1993).

Eastern H.U. Sverdrupfjella is dominated by units from the Rootshorga Formation but also contains Sveabreen gneisses (Fig. 3.3) and to a lesser extent members of the Fuglefjellet Formation (Ohta, 1996). The Rootshorga Formation is characterised by pelitic to semipelitic garnet-biotite gneisses (locally containing sillimanite and kyanite) and undifferentiated felsic paragneisses and orthogneisses that contain pre-tectonic metamafic lenses and metamafic bodies. These gneisses were mainly derived from greywackes that were deposited along an active continental margin or in an ocean island environment (Groenewald *et al.*, 1995). The interstitial metamafic and ultramafic rocks constitute <5 % of the Rootshorga Formation (Fig. 3.3) and have variable compositions that include dunites, pyroxenites and gabbros (Groenewald *et al.*, 1995).

Various pre- to syntectonic orthogneisses have been grouped together on the basis of structural and petrographical data by Groenewald *et al.* (1995). Concordant leucogranitic sills and veins are interpreted as melt that formed during the early stages of metamorphism; however, the absolute ages are unknown. Approximately 1130 Ma (Harris *et al.*, 1995) Fugitive (garnet-biotite) granites were also interpreted to predate deformation and likely crystallised from mobile restite melt that was being transported through the crust. Approximately 1060 Ma (Harris *et al.*, 1995) Sveabreen orthogneisses are typically megacrystic and associated with shallow, reverse shear zones; they occur as tabular units and are inferred as early- to syn-tectonic. The above-mentioned orthogneisses are cross-cut by tabular or narrow granodiorites that can be up to ~300 m thick (Board, 2001).

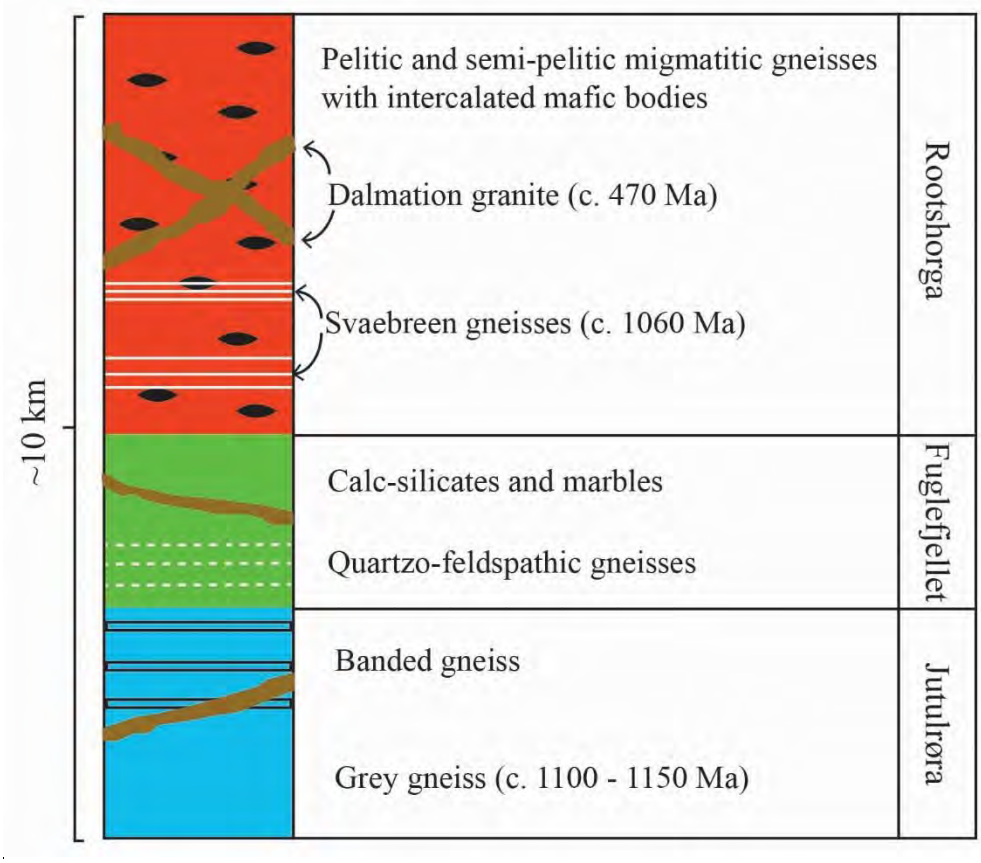

Figure 3.3: Lithostratigraphic column of major lithologies and formations found in H.U. Sverdrupfjella

Younger, medium-grained to megacrystic, post-tectonic monzogranitic dykes vary in thickness between ~10 cm and 60 m and have a variety of orientations (Board, 2001). Three generations of these post-orogenic felsic dykes were identified based on cross-cutting relationships; however there is no consistent orientation among the three generations, they are very similar in composition and are therefore thought to have intruded at a similar time. The *c.* 470 Ma, undeformed Dalmation granites cross-cut these felsic dykes in the eastern domain and are generally oriented sub-parallel to the regional foliation (Grantham *et al.,* 1991). The monzogranites from the Brattskarvet intrusive suite intruded into the country rock gneisses at *c.* 520 Ma (Moyes *et al.*, 1993) but exposures are limited to NE H.U. Sverdrupfjella at Brattskarvet. Subvertical, N-S-trending, dolerite dykes cross-cut the units described above (Grantham, 1992; Grantham, 1996; Ohta, 1996).

3.2.2 Deformation and metamorphic history of H.U. Sverdrupfjella

Early work was carried out by Wolmarans and Kent (1982) to determine metamorphic conditions within the Maud Belt. Further research in the late 1980s and the 1990s placed more emphasis on H.U. Sverdrupfjella (Grantham *et al.*, 1988; Moyes and Groenewald, 1996), whereas other researchers only focussed on eastern H.U. Sverdrupfjella (Groenewald and Hunter, 1991; Grantham *et al.* 1995; Board *et al.* 2005). The geometries of structures from five main deformation events (D_1 to D_5) were first described in detail by Grantham (1992) and Groenewald (1995) who worked in the western and eastern domains of H.U. Sverdrupfjella, respectively. These five deformation events were subsequently summarised into three main deformation events based on the inferred timing of deformation (Grantham *et al.*, 1995).

3.2.2.1 Deformation history of H.U. Sverdrupfjella

D_1 was ascribed to isoclinal, rootless intrafolial folds that were refolded by D_2 to form transposed, isoclinal folds that were moderately inclined to the SE. D_2 also involved top-to-NW shear that formed well-developed SE-plunging mineral lineations. D_1 and D_2 from Groenewald (1995) were combined by Grantham *et al.* (1995) into a prolonged D_1 event that occurred at *c.* 1000 Ma during the Grenvillian orogeny. Whole-rock, Rb-Sr isotope analyses of samples collected from the Rootshorga Formation yielded ages of 1183 ± 27 Ma (Moyes and Barton, 1990; Groenewald *et al.*, 1995) and 1071 ± 253 Ma (Moyes and Groenewald, 1996). Zircon analysis from a sample collected at Salknappen also suggests that the Rootshorga gneisses are Grenvillian in age (Harris, P.D., unpubl. data cited in Moyes and Groenewald, 1996). The inferred timing of the prolonged D_1 Grenvillian-aged orogeny is largely based on the abundance of *c.* 1150 Ma ages obtained from isotopic work done in H.U. Sverdrupfjella. Therefore it was traditionally thought that the metamorphism and deformation in H.U. Sverdrupfjella was Grenvillian in age. Pan-African garnet Sm-Nd ages found in samples collected in Rootshorga gneisses suggest that there was at least a thermal overprint at *c.* 500 Ma but whether or not the rocks were deformed concurrently is uncertain (Moyes and Groenewald, 1996).

More recently, zircon core ages collected from syn-tectonic leucosomes in the Rootshorga gneisses reflect ages between 1030 Ma and 1040 Ma; however, the rims/mantles of these zircons reflect younger ages of between *c.* 565 Ma and *c.* 499 Ma (Board *et al.*, 2005). The

same study dated monazite inclusions in D_1 top-to-NW fabric-defining minerals at *c.* 539 Ma (Board *et al.*, 2005) and used these results to infer that there was a major Pan-African tectonothermal event at *c.* 540 Ma. They also suggested that the Pan-African overprint in eastern H.U. Sverdrupfjella was much larger than previously thought. The timing of deformation and the exact degree of Pan-African overprint in eastern H.U. Sverdrupfjella still remains contentious.

Prior to the study by Board *et al.* (2005), there were very few constraints on the Pan-African deformation event in H.U. Sverdrupfjella. Pan-African structures that were identified formed as a result of D_3 and D_4 deformation events (Groenewald, 1995) and correspond to localised, tight to isoclinal, NE-plunging folds and open, upright NE-SW-striking folds, respectively. Grantham *et al.* (1995) grouped these two events together into a D_2 deformation period that was Pan-African in age. D_2 was assigned a Pan-African age as a result of the inferred syn-tectonic emplacement of the Dalmatian granite, where absolute dating thereof yielded ages of *c.* 470 Ma (Grantham *et al.*, 1991). Additionally, tight, NE-SW-striking folds are present in the *c.* 520 Ma (Moyes *et al.*, 1993) Brattskarvet monzogranites and it was assumed that the folding was Pan-African in age (Grantham *et al.,* 1995).

Recent work by McGibbon (2014) revealed that Pan-African deformation in western H.U. Sverdrupfjella is confined to discrete, reactivated, subhorizontal shear zones that can locally be subvertical.

The final deformation episode D_3 (Grantham *et al.*, 1995) was ascribed to the break-up of Gondwana and is characterised by N-S-trending, NE-SW-trending fractures, normal faults and emplacement of Karoo-aged dolerite dykes.

3.2.2.2 Metamorphic history of H.U. Sverdrupfjella

Early P-T estimates of H.U. Sverdrupfjella were made by Groenewald and Hunter (1991). They focussed on the NE section of H.U. Sverdrupfjella and the metamorphic history of the area but refrain from commenting on the age of peak metamorphism. This was followed by work from Grantham *et al.* (1995) and Moyes and Groenewald (1996) who ascribe the granulite facies peak metamorphism to the Grenvillian event and inferred that retrogression was caused by the Pan-African event. Although Board *et al.* (2005) have similar P-T estimates to previous workers (Fig. 3.4), they suggest that most of the textures and assemblages preserved in the

gneisses from H.U. Sverdrupfjella are Pan-African in age. Thomas (2014) favours Grenvillian-aged peak and retrogression events. A clockwise P-T path is envisaged for the evolution of H.U. Sverdrupfjella (Fig. 3.4), (Grantham *et al.*, 1995; Moyes and Groenewald, 1996; Board *et al.*, 2005; Thomas, 2014).

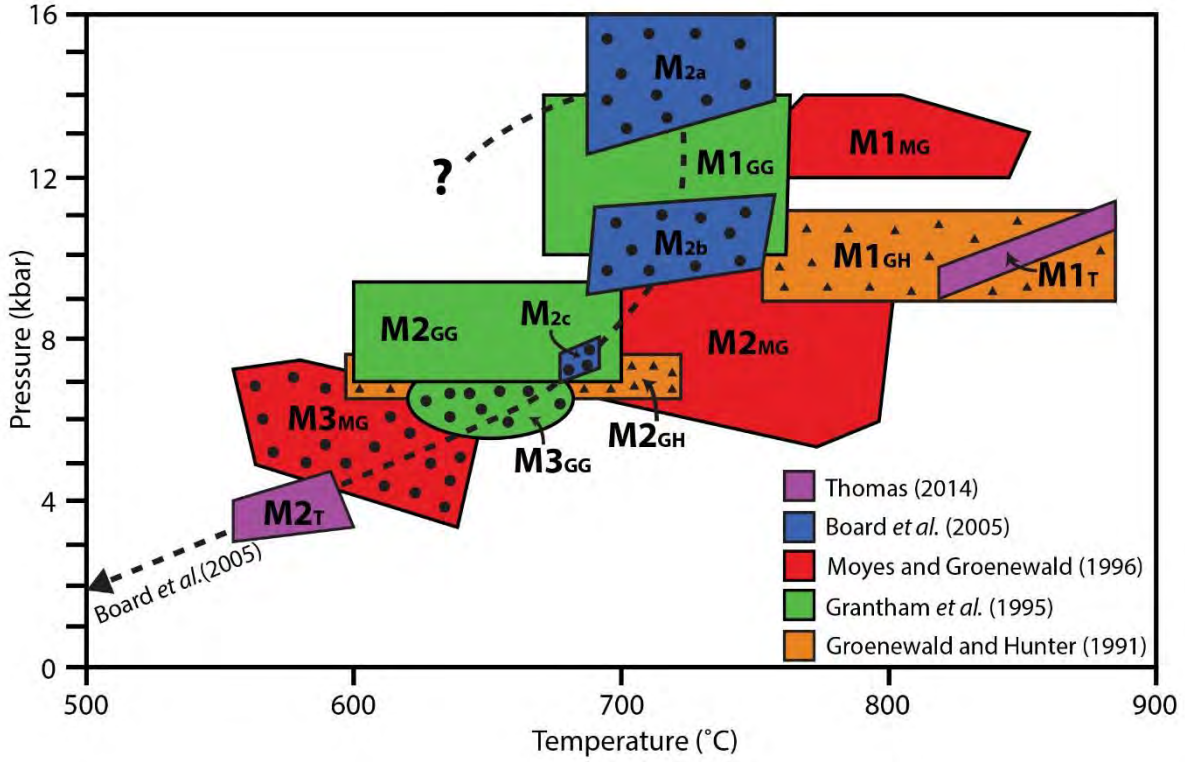

Figure 3.4: Summary of P-T paths and inferred metamorphic conditions in H.U. Sverdrupfjella. Metamorphic events that contain black dots are Pan-African in age whereas events with no texture fill are Grenvillian. P-T estimates that do not differentiate the timing of metamorphism contain black triangles.

Groenewald and Hunter (1991) identified two main metamorphic phases – ($M1_{GH}$ (Groenewald-Hunter) and $M2_{GH}$) by using thermobarometry in metamafic and metapelitic rocks. The peak metamorphic temperatures and pressures indicated by ($M1_{GH}$) are ~750-880 ºC and 9-11 kbar, respectively. After a combination of decompression and cooling, the rocks were retrogressed at temperatures and pressures ($M2_{GH}$) between ~600-720 ºC and 6.5-8 kbar, respectively. The ages of the $M1_{GH}$ and $M2_{GH}$ events are undetermined.

Grenvillian-aged D_1 (Grantham *et al.*, 1995) is believed to record two stages of peak metamorphism $M1_{GG}$ (Grantham *et al.*) and $M2_{GG}$ where near-isothermal decompression occurred

from ~12 ± 2 kbar at ~675-750ºC ($M1_{GG}$) down to ~7-9.5 kbar between ~600-700ºC ($M2_{GG}$). The peak metamorphic conditions during $M1_{GG}$ are slightly higher than peak pressures calculated by Groenewald and Hunter (1991) and $M1_{GG}$ temperature estimates are marginally lower. Grantham *et al.* (1995) ascribe a third period of metamorphism ($M3_{GG}$) to Pan-African deformation (D_2), where temperatures and pressures were ~650ºC and ~6.5 kbar, respectively.

Moyes and Groenewald (1996) summarised and modified previous P-T work done by Grantham *et al.* (1988, 1995) and Groenewald and Hunter (1991) and acknowledge three main phases of metamorphism / deformation. High-grade, eclogite-facies metamorphism reflected by $M1_{MG\ (Moyes\text{-}Groenewald)}$ is followed by near-isothermal decompression to amphibolite-facies conditions ($M2_{MG}$). Both $M1_{MG}$ and $M2_{MG}$ are Grenvillian in age and are followed by a lower-amphibolite-facies $M3_{MG}$ event that was suspected to be Pan-African in age.

Board *et al.* (2005) acknowledged two distinct high-grade metamorphic events at *c.* 1000 Ma and *c.* 500 Ma (M_2). The *c.* 1000 Ma event in Board *et al.* (2005) was inferred from P-T work done by Groenewald and Hunter (1991). Thermobarometry and thermodynamic modelling done on samples collected by Board *et al.* (2005) resulted in the identification of three metamorphic phases - $M_{2a,\ 2b,\ 2c}$, that form a coherent clockwise P-T path. Although it is uncertain whether or not the peak assemblage (M_{2a}) preserved in their mafic samples is Grenvillian or Pan-African in age, they favour the interpretation that their samples only preserved effects of Pan-African metamorphism, i.e. M_2. Peak eclogite-facies conditions (M_{2a}) were inferred from a reaction texture where hornblende-plagioclase symplectites replace omphacitic clinopyroxene in mafic rocks. M_{2a} was followed by near-isothermal decompression and syn-tectonic amphibolite-facies metamorphism (M_{2b}) recorded by equilibrated amphibolites. Retrograde metamorphism recorded by pelitic samples is represented by M_{2c} (Fig. 3.4).

Recent P-T estimates from Thomas (2014) were done on samples collected from Southern H.U. Sverdrupfjella at Nupskåpa. This study identified a Grenvillian-aged ($M1_{T\ (Thomas)}$) event that occurred at relatively high temperatures that overlaps with $M1_{GH}$ but confines the peak P-T estimates to a narrower range than earlier studies (Fig. 3.4). The P-T estimates of the $M2_T$ retrogressive event identified by Thomas (2014) overlaps the retrograde path from Board *et al.* (2005) and is thought to have been part of the same Grenvillian-aged tectonic cycle as M_{1T}.

The clockwise P-T path derived by Board *et al.* (2005) roughly intersects P-T estimates derived by Groenewald and Hunter (1991), Grantham *et al.* (1995) as well as those summarised by Moyes and Groenewald (1996), (Fig. 3.4). All studies in Figure 3.4 other than Board *et al.* (2005) agree that the granulites are Grenvillian in age and that Pan-African retrogression occurred at amphibolite facies conditions. Board *et al.* (2005) also suggest that the Pan-African event reached eclogite facies metamorphic conditions.

3.3 The geology of Salknappen

Work for this study was carried out at the Salknappen nunatak (Fig. 3.2), in the central domain of eastern H.U. Sverdrupfjella. Salknappen forms a group of small nunataks (up to ~1 km in size) about 5 to 10 km to the south-east of Fuglefjellet. These nunataks are predominantly made up of undifferentiated felsic paragneisses from the Rootshorga gneiss complex with the Svaebreen gneiss and amphibolite dykes constituting subordinate lithologies (Fig. 3.5). The dominant tectonic foliation in the area dips moderately to the south-east between 30 and 50º. Thrust zones oriented parallel to this fabric have also been noted in the area (Ohta, 1996).

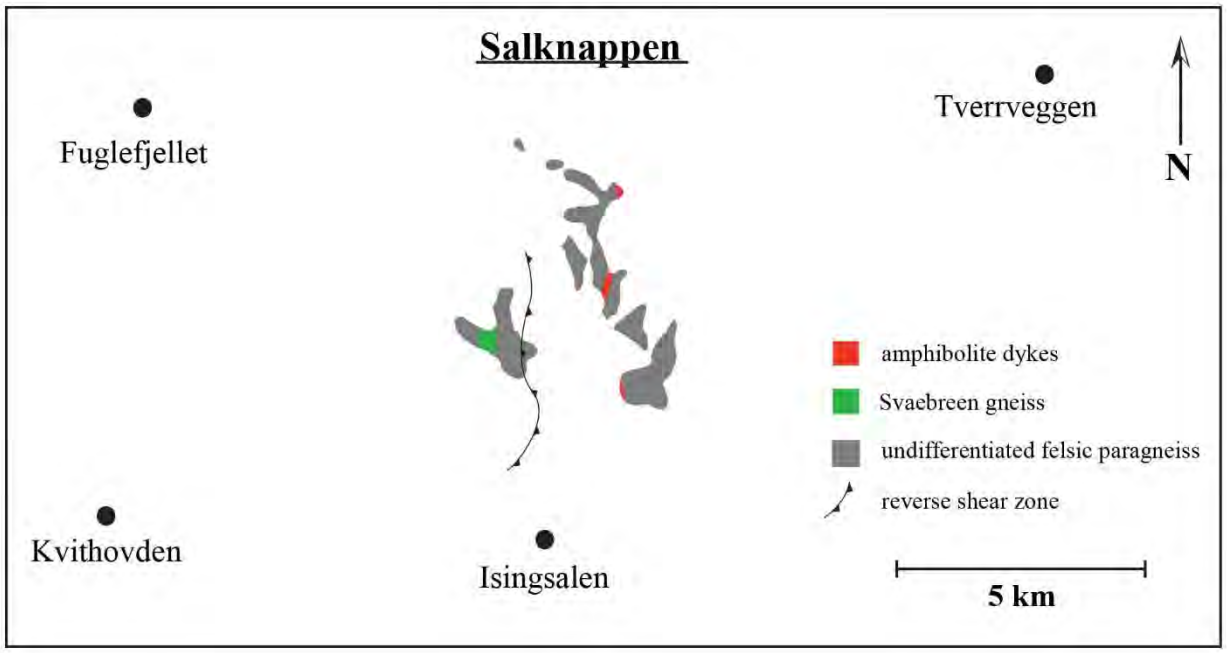

Figure 3.5: Geological map of Salknappen, eastern H.U. Sverdrupfjella.

The outcrops at Salknappen have not been described in detail before. Field observations made in this study of the undifferentiated felsic paragneisses from the Rootshorga formation are described in chapter 4.

4. Field relations and deformation history

4.1 Outcrop map and lithology descriptions

The outcrop maps in Figures 4.1 and 4.2 are digitised from field observations of a NW-SE striking vertical outcrop (Fig. 4.1a), situated at 72º19.346' S, 001º00.238' E that forms a part of the Salknappen nunatak (referred to as SkA). Several foliation, lineation and intrusion orientations were taken and are represented in stereoplots in Figures 4.2b, c, and d. The outcrop at location 'SkA' comprises various lithologies that include: garnet-biotite-feldspar gneisses, metamafic bodies and leucosome-rich migmatites that are cross-cut by megacrystic leucogranitic dykes and equigranular (Dalmation) granite sheets.

Concordant and discordant megacrystic leucogranite dykes that cross-cut normal shear zone 1 (Fig. 4.2a) are younger than the shear zone because they are undeformed by the shear zone. Concordant leucogranite dykes cross-cutting normal shear zone 2 (Fig. 4.2a) are younger than this shear zone because they are undeformed by the shear zone and discordant leucogranite dykes are most likely also younger than shear zone 2 because the upper section of the large dyke near to shear zone 2 is subparallel to the centre of the shear zone. This could mean that the discordant dykes are syn-tectonic with shear zones oriented similarly to shear zone 2 but this interpretation is not favoured because there are no other shear zones where other large concordant leucogranite dykes are present in this outcrop.

Normal shear zones that are younger than the megacrystic leucogranite dykes exist because shear zone 3 in Figure 4.2a displaces and deforms the leucogranite dykes. Dalmation granite sheets are oriented slightly oblique to the gneissic foliation and located in the centre of shear zone 3.

4.1.1 Garnet-biotite-feldspar gneiss

The outcrop is predominantly made up of well-foliated leucosome-bearing garnet-biotite-feldspar gneisses. The garnet-biotite-feldspar gneisses are brown, grey and white in colour and are made up of layers, consisting of leucosomes and melanosomes (Fig. 4.3a). The foliation generally dips shallowly towards the east (Fig. 4.2b) and contains a strong to moderate biotite and quartz lineation that plunges shallowly towards the south-east (Fig. 4.2b). Garnet-biotite-feldspar-sillimanite gneisses are present in thin layers less than ~30 cm thick and generally scarce in the area.

Melanosomes contain ~5-10% medium (0.5-1 mm) to coarse-grained (> 1 mm) garnet porphyroblasts mantled by biotite. Medium to coarse-grained biotite makes up ~30-40% of the matrix and the remainder of the matrix comprises fine to medium-grained quartz and feldspar.

Leucosomes contain ~5% garnet, have less than ~5% biotite in the matrix and are predominantly made up of medium to coarse-grained quartz and feldspar. A range of maroon-red garnet grain sizes between ~1 mm and 2 cm are present in coarse-grained quartz-feldspar leucosomes and coarse-grained, biotite-rich melanosomes. Coarse-grained biotite (~1-2 mm) wraps around garnet porphyroblasts in the leucosomes, and in places δ-type porphyroblasts of garnet are present and indicate a top-to-NW sense of shear (Fig. 4.3b). Leucosomes typically form narrow lenses ~10-20 cm long (Fig. 4.3a) but also form wider structures that are several metres long. Where these structures become interconnected or coalesce, they form 'leucosome-rich migmatites' (Fig. 4.1a, b).

4.1.2 Leucosome-rich migmatites

Leucosome-rich layers are oriented parallel to the gneissic foliation (Fig. 4.2b). Leucosome-rich migmatites (Figs. 4.1b, 4.2a) are white, relatively thick zones (~0.5-10 m) comprised of more than 95% leucosome whereas the other ~5% is schlieren of wallrock (garnet-biotite-feldspar gneiss) fragments and melanosome material. The medium- to coarse-grained leucosomes that make up this unit do not contain any garnet and are made up of ~40% quartz, ~50-60% feldspar and less than ~5% biotite. Units as thin as ~1-2 m thick are laterally continuous for at least ~70 m along strike in the gneissic foliation; however, not all units are continuous and layers less than ~0.5 m pinch out along the foliation. In places, leucosome-rich migmatites are truncated by tightly folded mafic bodies (Fig. 4.2a, just to the right of centre).

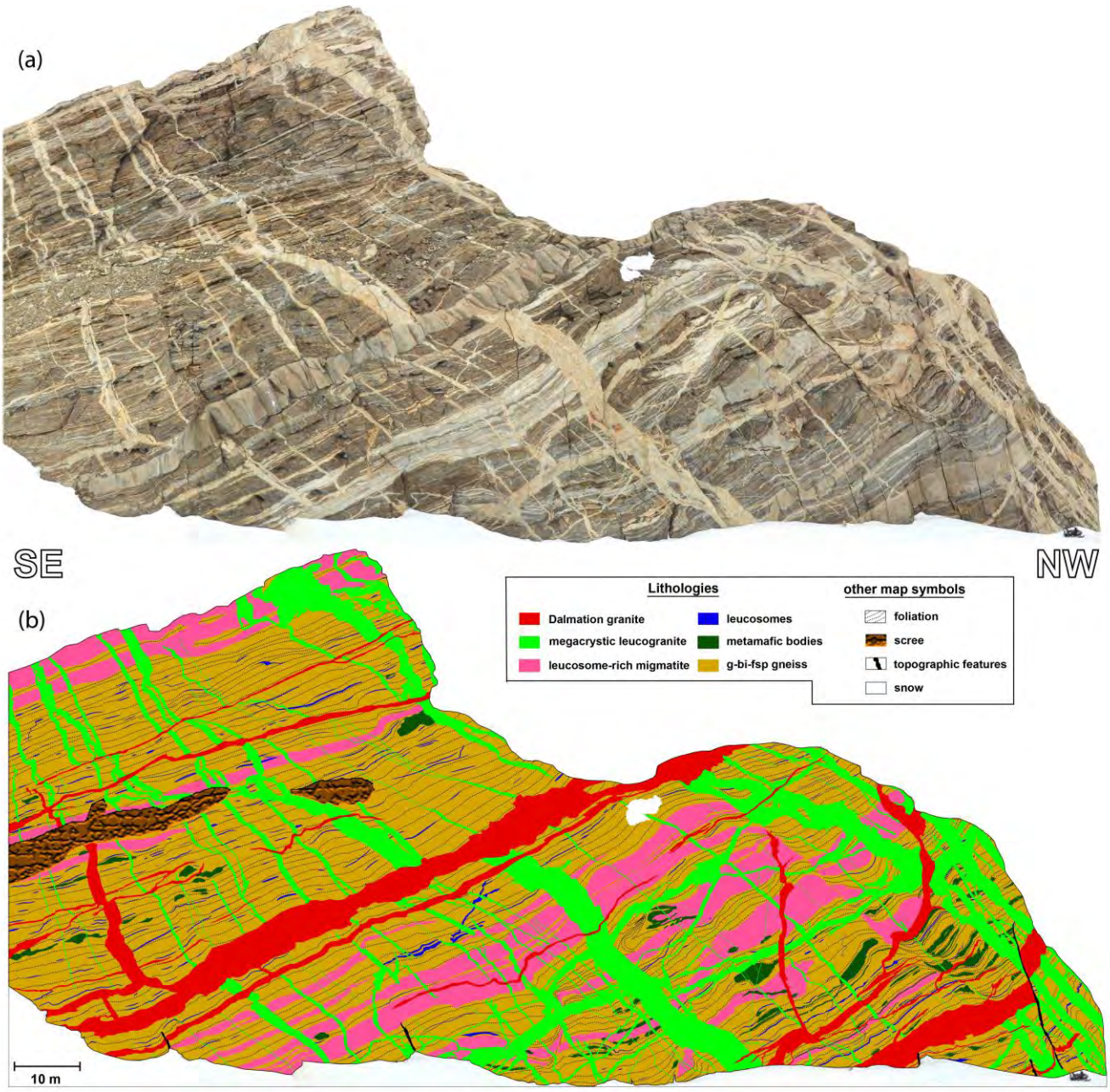

Figure 4.1: (a) Outcrop at location 'SkA' and (b) Digitised outcrop map of a section through Salknappen in HU Sverdrupfjella, Antarctica

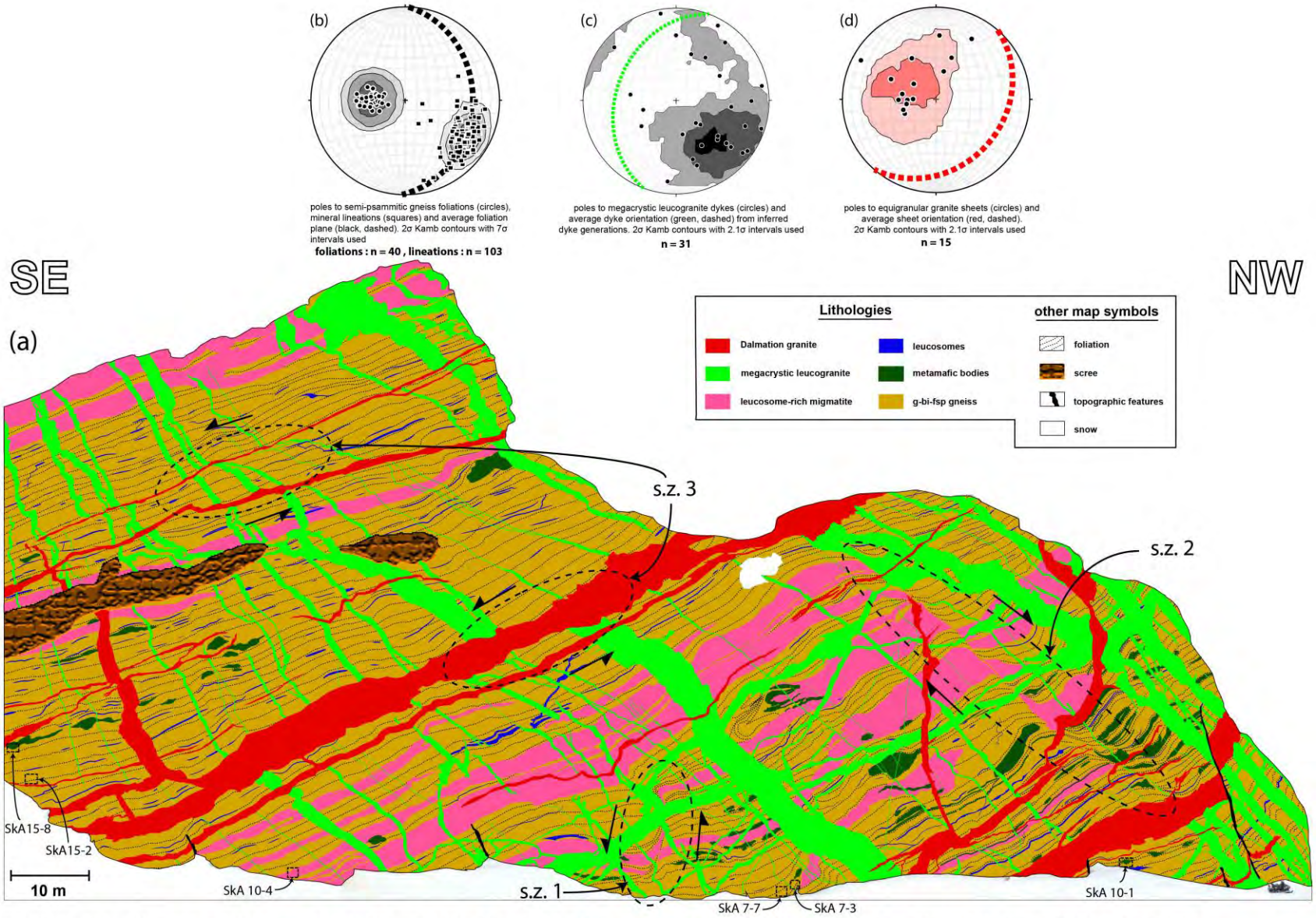

Figure 4.2: Digitised outcrop map with sample localities of a section through Salknappen in HU Sverdrupfjella, Antarctica

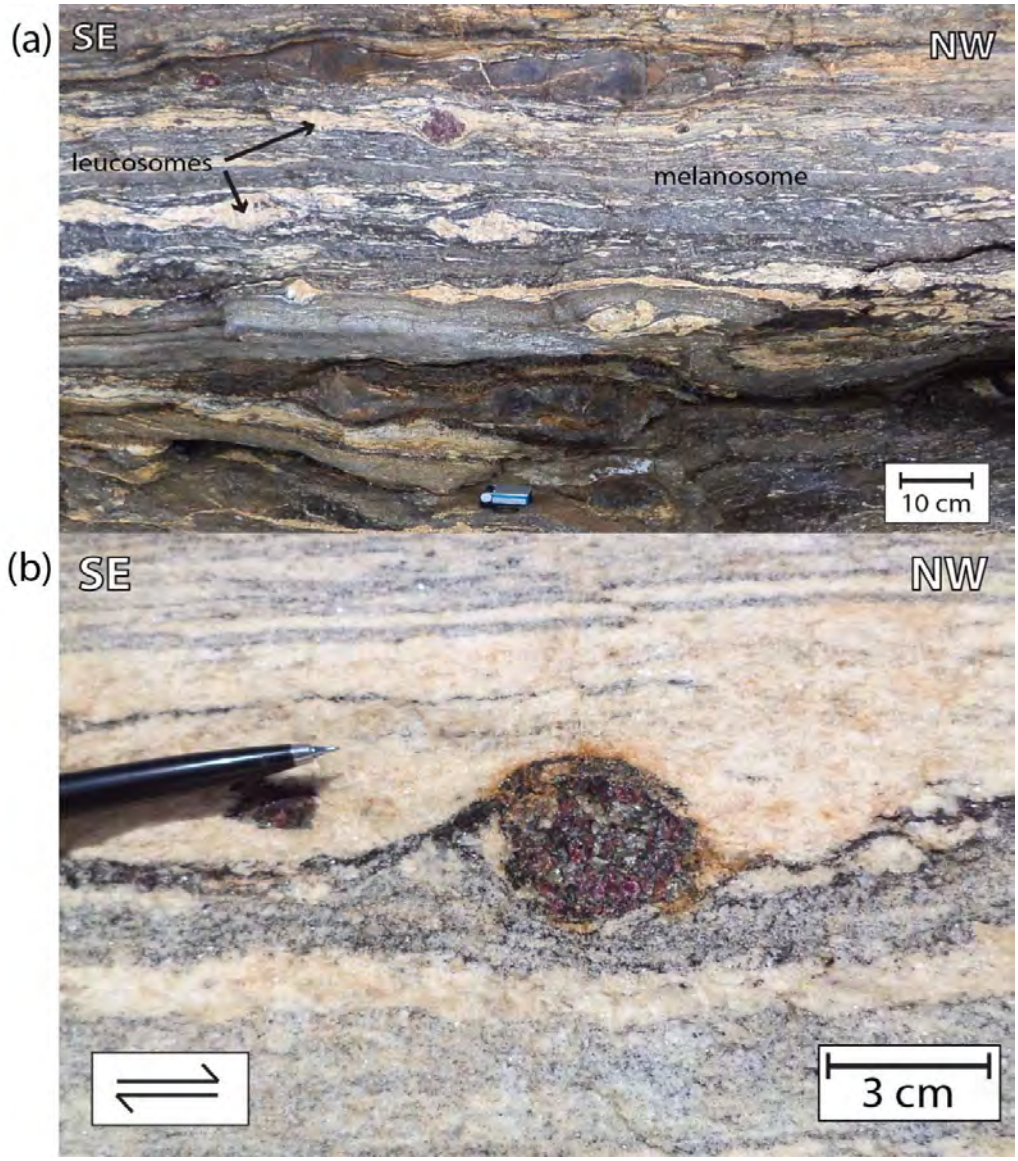

Figure 4.3: Field photographs showing: (a) gneissic banding of leucosomes and melanosomes typical of the garnet-biotite-feldspar gneiss and (b) a garnet δ-type porphyroblasts showing a top-to-NW shear-sense.

4.1.3 Metamafic bodies

Metamafic bodies are dispersed throughout and intercalated within the garnet-biotite-feldspar gneiss. They are oriented subparallel to the gneissic foliation. Metamafic bodies and metamafic lenses only constitute a small part of the section and are typically between ~10 cm and ~10 m long (Fig. 4.1a, b). They are generally equigranular, fine to medium-grained and are largely made up of hornblende and feldspar. Garnet is rarely seen but is present in association with feldspar.

4.1.4 Megacrystic leucogranite dykes

Megacrystic leucogranite dykes are abundant in this outcrop and cross-cut the lithologies described above. Leucogranitic dykes are moderately inclined and dipping to the ESE and WNW (Fig. 4.2a, c). Dykes dipping towards ESE are oriented subparallel to the gneissic foliation and will therefore be referred to as *concordant* dykes, whereas dykes dipping WNW that cross-cut the foliation will be referred to as *discordant* dykes. Both varieties are megacrystic and consist of ~30% quartz, ~60% feldspar, less than 10% biotite and accessory tourmaline and garnet.

Discordant dykes are the most abundant and make up ~90% of the megacrystic leucogranite dykes (Fig. 4.2a, c). They are between ~0.2 m and ~5 m thick and exist as single dykes that are ~10-50 m long (Fig. 4.2a). They do however commonly coalesce into thicker dykes or split up into thinner ones up-dip. They also intersect concordant dykes; however there is only vague evidence of the relative age relationship between the concordant and discordant dykes. In most cases it is unclear which of these dykes cross-cuts the other (Fig. 4.4) but there are examples of concordant dykes that cross-cut discordant dykes (Fig. 4.4). Concordant dykes make up ~10% of the leucogranite dyke swarm and have a relatively narrow thickness range between ~0.5 m and ~2 m.

4.1.5 Equigranular granite sheets (Dalmatian granites)

Equigranular granitic sheets are less abundant than the megacrystic granitic dykes and cross-cut all of the above-mentioned lithologies and shear zones. They are equigranular, medium-grained (0.5-1 mm), contain ~30% quartz, ~50-60% feldspar, ~10-20% biotite and constitute the 'Dalmation granites' described by Grantham *et al.* (1991). The Dalmation granites generally dip moderately to the south-east (Fig. 4.2c); however, some sheets are steeply-dipping towards the north-west (Fig. 4.2a). These granite sheets are typically between ~0.5 and 7 m thick. The Dalmation granites appear to be undeformed but the thickest unit in the outcrop is not completely tabular and pinches and swells along the dip direction of the unit.

Figure 4.4: Outcrop showing relative age relationships between megacrystic leucogranite dykes where: (a) concordant dykes cross cut the discordant dykes (in blue ellipses), and (b) the age relationship between the leucogranite dykes is unclear (in red ellipse).

4.2 Microstructural descriptions of major lithologies

Samples collected from the Salknappen nunatak were cut perpendicular to cleavage and parallel to a moderate to strong biotite and quartz lineation in the rock. Polished thin sections were produced from blocks taken along this cut surface.

Field relations provide an insight into the deformation history of the area and microstructures are useful to help expand on the deformation history. The gneissic foliation and tabular lithologies (mafic bodies and leucosome-rich migmatites) are oriented subparallel to one another in the outcrop face from which samples were collected. This face trends subparallel to mineral lineations in the foliation plane and is perpendicular to the gneissic foliation, such that the outcrop map represents the XZ plane of the local finite strain ellipsoid.

4.2.1 Garnet-biotite-feldspar gneisses (melanosome)

Melanosomes are characterised by narrow, sparse biotite-rich domains that are only ~1-2 cm long and also have magmatic quartz subparallel to the foliation (Fig. 4.5a). Biotite grains form a weakly interconnected framework parallel to the dominant lineation (Fig. 4.5b) but in general, biotite in the matrix is poorly interconnected owing to the fact that it is separated by quartz and feldspar that make up ~75% of the melanosome (Fig. 4.5b). The long axes of biotite in the matrix are moderately to strongly oriented in the same direction where grain aspect ratios are typically between 5 and 10.

Feldspar grains rarely exhibit flame perthite structures in the grains from the matrix. Feldspar and quartz grains that are adjacent to biotite are anhedral and seem to inherit the form of the margin at the biotite grain. Pinning microstructures are common (Fig. 4.5c) and feldspar and quartz grains seldom contain biotite inclusions. Grain boundaries between adjacent feldspar grains are typically straight or gently curved; however where quartz and feldspar lie adjacent to one another in the matrix, grains are often more curved, lobate and less commonly straight (Fig. 4.5c). Quartz crystals in the matrix commonly have curved grain boundaries; however less commonly examples of smaller subhedral grains are present.

Quartz grains in leucosomes are generally significantly larger (up to ~6 mm) but small grains may be as little as 100 μm in size. Large grains are elongate with their long axes oriented subparallel to biotite long axes in the matrix (Fig. 4.5a). Grain boundaries of leucosomes are anhedral and display evidence of bulging and subgrain rotation (Fig. 4.5d). Large quartz grains are also partially recrystallised in areas that are relatively richer in biotite. Quartz from the matrix as well as from melt veins displays undulose extinction.

4.2.2 Leucosomes in leucosome-rich migmatites

These leucosomes are rich in quartz, plagioclase and K-feldspar that make up ~40, ~20-30 and ~20-30 modal percent of the sample, respectively. Coarse grains are anhedral whereas fine-grained quartz and feldspar grains are subhedral to anhedral. The long axes of coarse-grained quartz crystals are strongly aligned in the same direction and aspect ratios of these grains are typically between 2 and 5. The long axes of feldspar grains are moderately to strongly aligned subparallel to the long axes of quartz grains but feldspar exhibits significantly lower aspect ratios (1-2) than quartz.

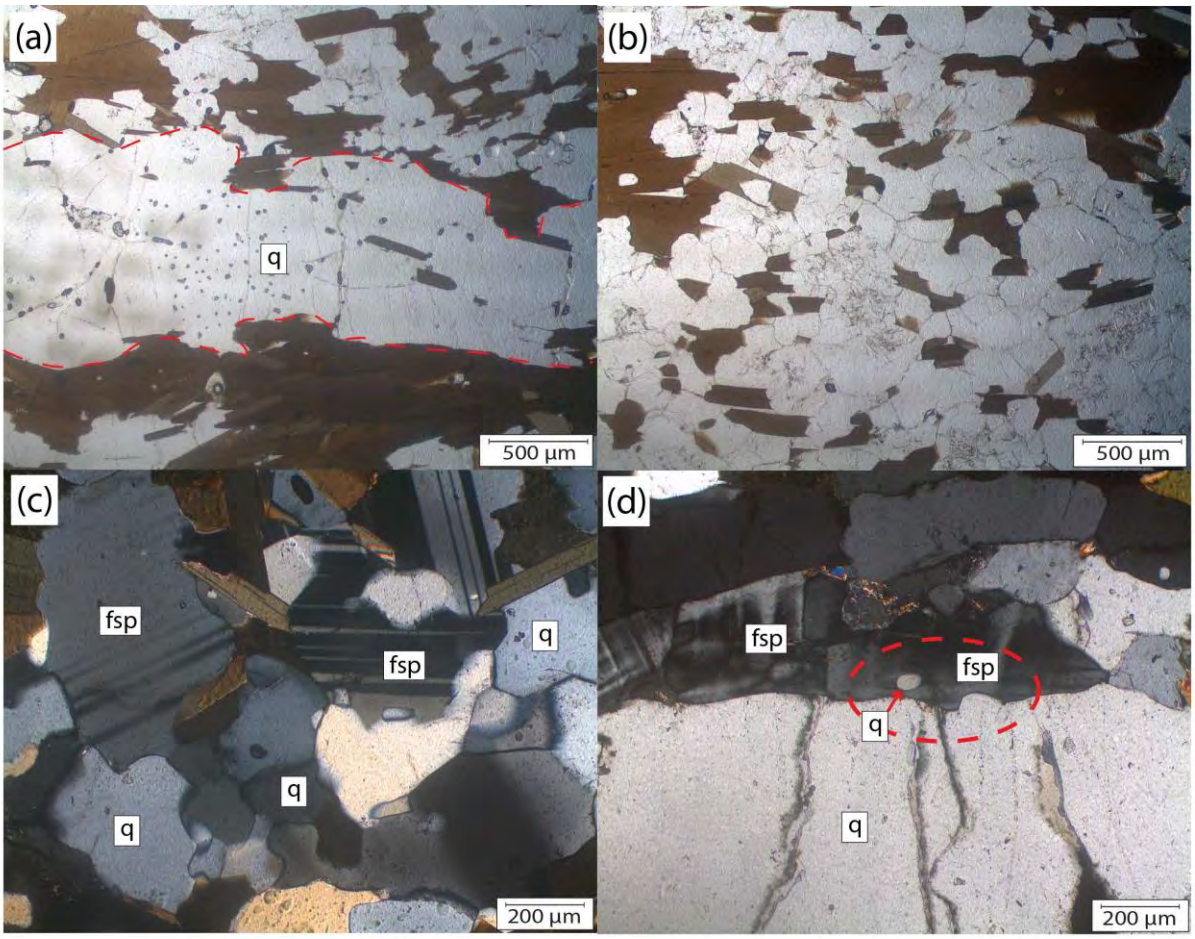

Figure 4.5: Photomicrographs of melanosomes typically found in the garnet-biotite-feldspar gneisses at SkA, showing: (a) biotite-rich zones and magmatic-quartz veins (between red dashes) oriented subparallel to the biotite foliation; (b) weakly interconnected biotite that makes up the majority of the matrix; (c) dominantly lobate grain boundaries between adjacent quartz and feldspar grains; and (d) bulging magmatic quartz vein grain boundaries and quartz subgrain rotation adjacent to a magmatic quartz vein.

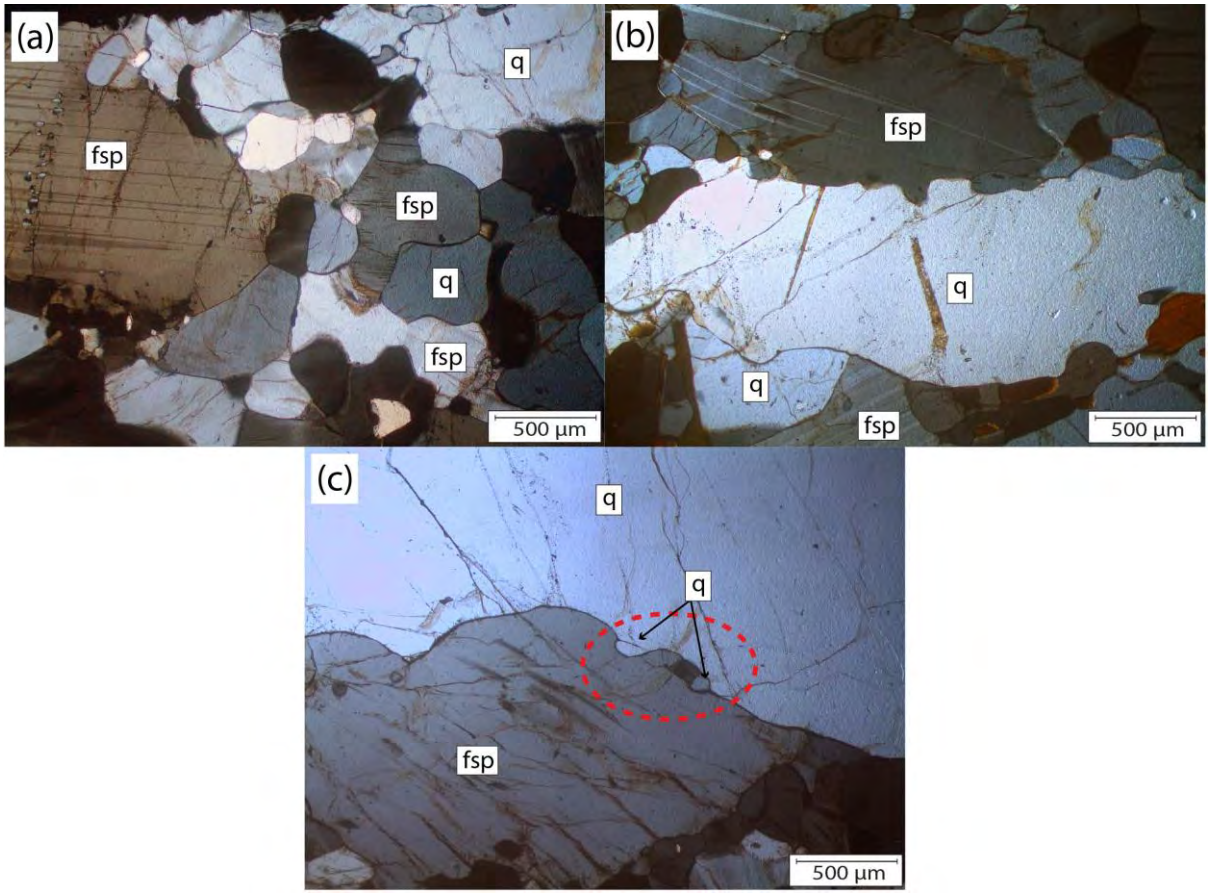

Figure 4.6: Photomicrographs of leucosome material from leucosome-rich migmatite lithologies at SkA, showing: (a) Lobate, irregular and straight grain boundaries between adjacent quartz and feldspar grains representative of the sample; (b) curved quartz grain boundaries, feldspar grain boundaries bulging into quartz and (c) the sparse formation of quartz subgrains (in red ellipse) where quartz bulges into feldspar.

Grain boundaries between coarse-grained quartz and feldspar grains are lobate, bulging or straight; however, straight boundaries are less common (Fig. 4.6a). Isolated, fine-grained subgrains of quartz and feldspar on the boundaries between coarse-grained quartz and feldspar are present but uncommon (Figs 4.6b, c). The grain boundaries between coarse-grained, adjacent quartz and adjacent feldspar crystals are typically curved, lobate and less commonly bulging. Straight grain boundaries are less common and are more common in fine-grained domains. Flame perthite is also common in coarse grains and lamellae are generally subparallel to the long axes of quartz and feldspar.

4.2.3 Metamafic bodies

When in contact with hornblende, plagioclase grain boundaries are dominantly irregular, but rare examples of straight grain boundaries do exist. When plagioclase is in contact with quartz or other plagioclase grains the grain boundaries are dominantly straight but can be gently curved and lobate (Fig. 4.7a). More rarely, these boundaries exhibit localised bulging. Quartz is less common and only forms ~5 modal percent of the matrix. When in contact with hornblende, the contacts look similar to those between plagioclase and hornblende and are irregular and curved. Subgrains are present in both quartz and feldspar.

Coarse-grained (~1-2 mm), quartz-rich leucosome veins have intruded into the mafic rocks. The grain boundaries in leucosomes are moderately curved when in contact with hornblende and plagioclase. The coarse-grained quartz crystals are largely intact but rarely exhibit evidence of bulging / subgrain rotation (Fig. 4.7b).

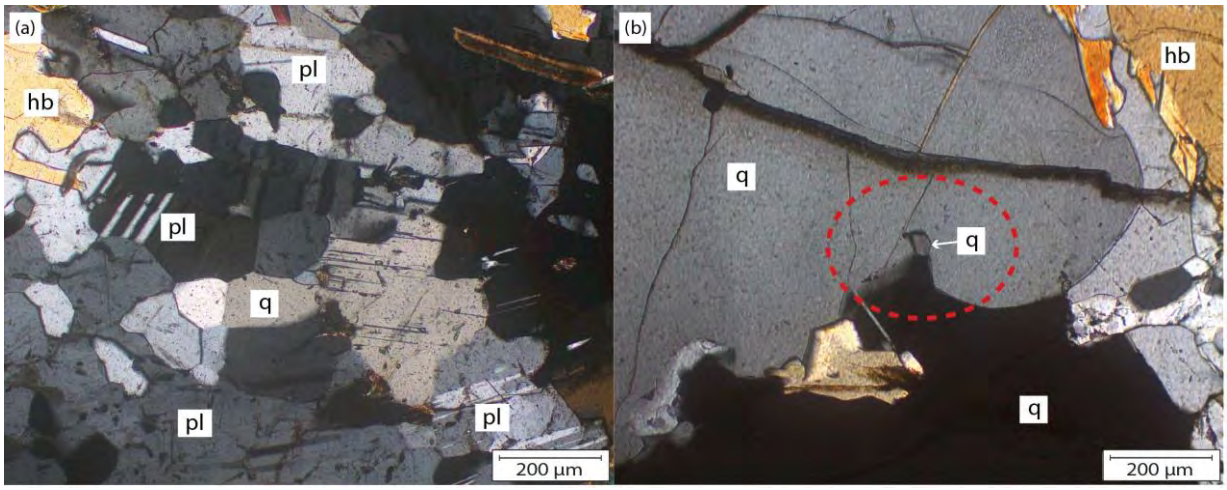

Figure 4.7: Photomicrographs of quartz and plagioclase microstructures in mafic samples from SkA, showing: (a) Grain boundary relationships between adjacent quartz and plagioclase grains, and (b) subgrain formation through bulging in a magmatic quartz vein (in red ellipse) that intruded into the mafic sample.

4.3 Comparing dynamically recrystallised grain sizes in garnet-biotite-feldspar gneiss samples collected in close proximity to a mafic lens

The mafic lens in Figure 4.8a is a seemingly more competent unit that might have forced more deformation to be accommodated by gneisses surrounding the lens. Therefore three samples were collected at variable distances measured orthogonally to the large mafic lens at an outcrop that forms part of the Salknappen nunatak (referred to as 'SkB') – GPS coordinates are 072º19.677' S and 000º58.915' E. The samples, SkB 11- 1, SkB 11-2 and SkB 11-4 were retrieved at distances of 71 cm, 42 cm and 3 cm away from the boundary between the garnet-biotite-feldspar gneiss and the mafic lens (Fig. 4.8b).

Samples were cut perpendicular to foliation and parallel to lineations defined by biotite and quartz. Polished thin sections were produced along this cut surface. Thereafter photomicrographs were taken using AnalysisGetIT software and calibrated scale bars were 'burnt' onto the images. Using the scale bars on the photomicrographs, the line-measuring tool on "imageJ" freeware was calibrated. Two randomly oriented diagonals were measured per a grain to calculate an average diagonal representative for a grain. Average diagonal measurements were then compared in histograms (Fig. 4.8 c, d, e).

Because of the geological history of the area, granulite facies assemblages and overall high-grade metamorphism that the region experienced and the curved / lobate quartz grain boundaries in the gneisses (excluding leucosomes), it was assumed that all of the quartz grains from the protolith are dynamically recrystallised. Vein quartz was not included and measured because they appear to post-date the main recrystallization event. Similarly, where quartz grain growth seemed to be restricted by pinning caused by the presence of biotite the quartz grain sizes were not measured.

Dynamically recrystallised quartz grain sizes range between ~40 μm and 700 μm, where the average grain size is typically ~200 μm (Fig. 4.8c, d, e). Standard deviations from the mean are high (~100 μm) in all three samples and histograms show that the datasets are positively skewed with only one distinct peak in each of the samples. At a distance of 71 cm away from the mafic lens, n = 172 and the mean recrystallised grain sizes and standard deviations are 187 μm and 104 μm, respectively. At a distance of 42 cm away from the mafic lens, n = 184 and the mean recrystallised grain sizes and standard deviations are 181 μm and 111 μm, respectively. At a distance of 3 cm away from the mafic lens, n =168 and the mean recrystallised grain sizes and standard deviations are 205 μm and 93 μm, respectively.

Dynamically recrystallised quartz grain sizes measured from the garnet-biotite-feldspar gneiss samples collected at the location in Figure 4.8 can be used to approximate the minimum crustal strength conditions prior to melting. By using a recrystallised grain size piezometer for quartz from Stipp and Tullis (2003, Figure 4) minimum flow stresses experienced by garnet-biotite-feldspar gneisses prior to melting are less than ~1 MPa.

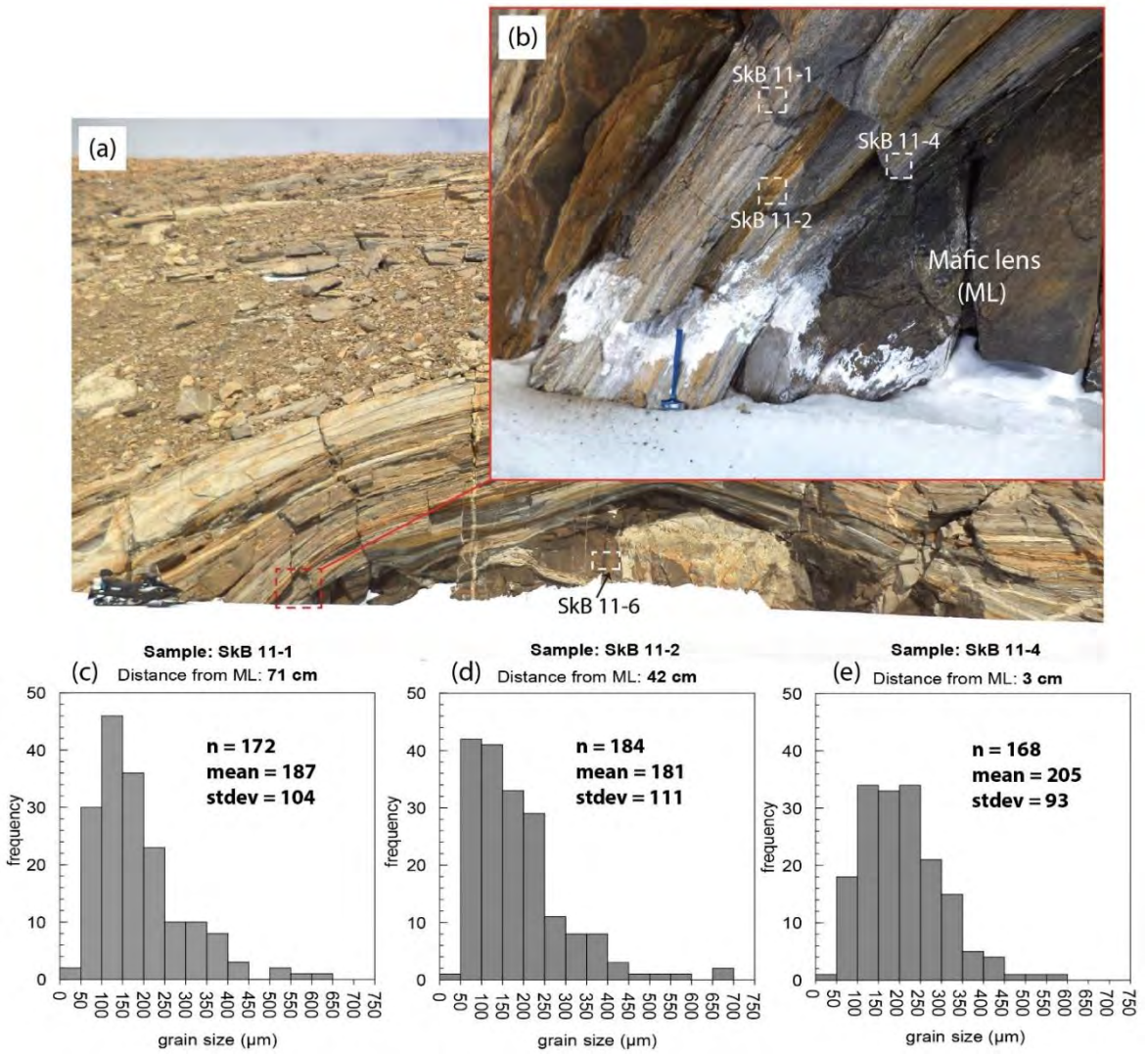

Figure 4.8: (a) Photograph of outcrop locality 'SkB' (looking SW) and (b) locations where samples SkB: 11-1, 11-2, 11-4 and 11-6 were collected. (c, d, e) Histograms showing the frequency of inferred dynamically recrystallised grain sizes of quartz in garnet-biotite-feldspar gneisses collected at variable distances from a mafic lens (ML).

5. Petrography of metamorphic assemblages

5.1 Petrography of metapelitic / metagraywacke samples

Three of the sampled metapelitic / metagraywacke rocks: SkA 7-3, SkA 7-7 and SkA 15-2 taken from the garnet-biotite-feldspar gneisses shown in Figure 4.2a were selected based on possibly useful mineral assemblages. These samples are similar to the garnet-biotite-feldspar gneiss described in chapter 3; however, the presence of minerals such sillimanite and cummingtonite in samples SkA 7-3, SkA 7-7 and SkA 15-2 is useful to model the metamorphic histories. Each of the samples is described below.

5.1.1 Sample SkA 7-3

Sample SkA 7-3 contains garnet, biotite, sillimanite, ilmenite, spinel, quartz, plagioclase and K-feldspar. Overall this sample exhibits a granoblastic texture where biotite laths are weakly interconnected but strongly oriented subparallel to one another. Sillimanite-rich zones are comprised of large aggregates of fine-grained sillimanite and are characterised by an increase in the amount of biotite relative to the matrix.

Subhedral to euhedral garnet grains that are between 100 μm and 1.5 mm in size are uniformly distributed throughout the matrix make up ~5 modal percent of the sample. Garnet porphyroblasts contain a combination of quartz and biotite inclusions, whereas some garnet grain boundaries are in contact with biotite, plagioclase, quartz, sillimanite and spinel. Garnet porphyroblasts typically overprint well-oriented biotite in the matrix (Fig. 5.1a)

Medium-grained (500 μm – 1 mm) to fine-grained (< 500 μm) aggregates of sillimanite are oriented parallel to the foliation defined by biotite laths. These aggregates are also oriented parallel to the foliation and are typically between 1 mm and 5 mm long (Fig. 5.1b). Small, isolated and fine-grained sillimanite mats are distributed throughout the matrix and do not form in laterally continuous layers. Overall, sillimanite constitutes between 5 and 10 modal percent of the sample.

Subparallel biotite laths make up ~20-30 modal percent of the sample and grain sizes range from less than 10 μm to 2 mm in size. Fine-grained, accessory ilmenite is present in the matrix, is associated with biotite and tends to grow parallel to the dominant biotite foliation. Medium-grained (500 μm – 1 mm), light green and isotropic spinel grains occur throughout the matrix in association with biotite. In the matrix where spinel is associated with biotite it embays into

biotite. Spinel grains are rarely in contact with garnet but when they are garnet and biotite appear to be in equilibrium with spinel (Fig. 5.1c), sillimanite (Fig. 5.1d) and quartz.

Quartz and plagioclase make up about 30 modal percent and 30 modal percent of the matrix, respectively. K-feldspar is restricted to leucosomes and makes up ~10 modal percent of the sample. Sparse euhedral quartz grains are present but the majority of the sample is comprised of subhedral and anhedral grains that vary in size from tens of microns to 2 mm. Similarly, K-feldspar grain sizes range from tens of microns to ~1 mm.

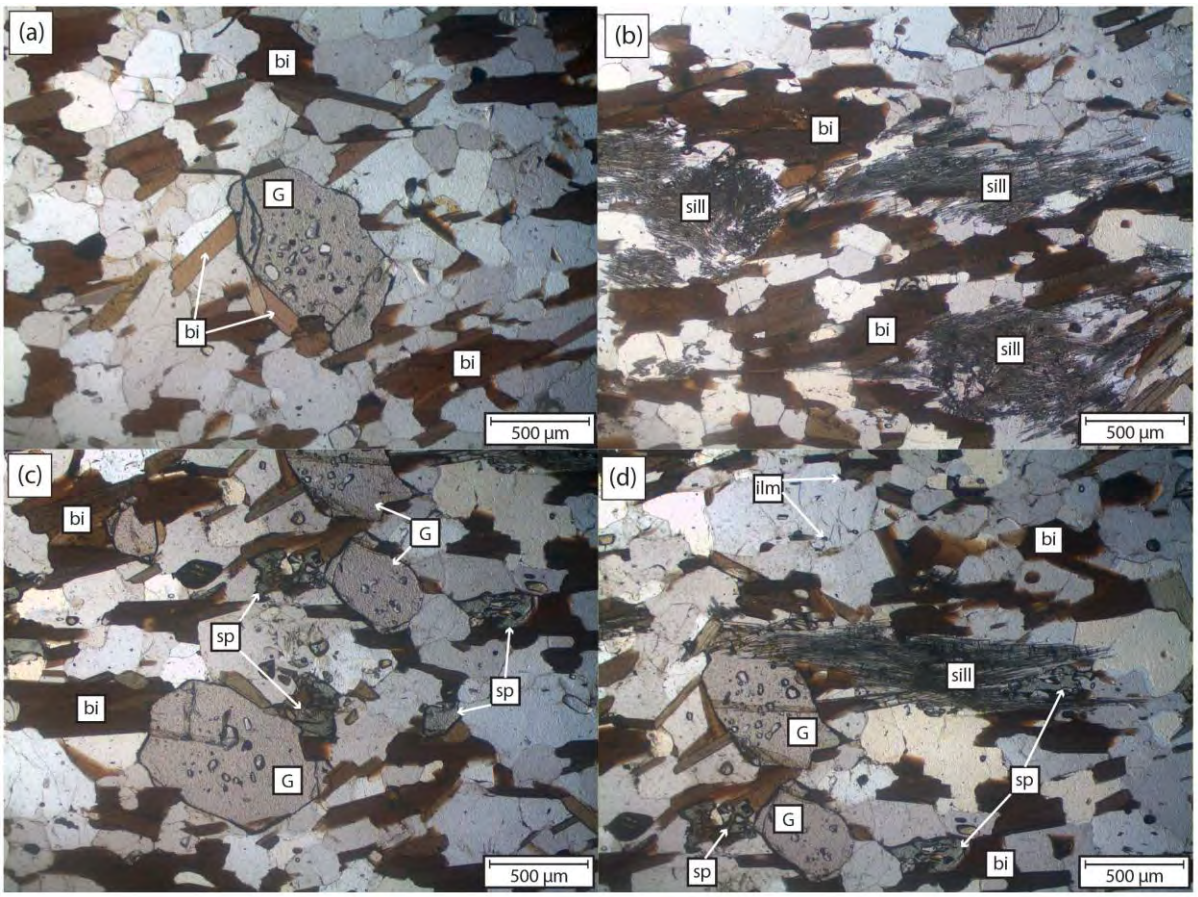

Figure 5.1: Photomicrographs representative of sample SkA 7-3. Images A and B are also representative of sample SkA 7-7. (A) Euhedral garnet porphyroblast overprinting biotite and mantled by minor biotite. (B) Sillimanite aggregates and needles in sillimanite-rich domains. Needles are subparallel to biotite laths. (C) Spinel adjacent to both garnet and biotite. (D) Sillimanite, spinel, garnet and biotite adjacent to one another.

5.1.2 Sample SkA 7-7

This sample exhibits a texture similar to sample SkA 7-3 where quartz, feldspar and biotite form an easily noticeable granoblastic texture throughout the matrix. Additionally, the long axes of biotite grains are strongly oriented subparallel to one another and sillimanite aggregates. Θ-type porphyroblasts made up of garnet and biotite are rarely observed in the matrix. The mineralogy in SkA 7-7 is similar to that of sample SkA 7-3; however spinel is absent in this sample.

Approximately 5-10 modal percent of SkA 7-7 is comprised of euhedral to subhedral porphyroblastic garnet grains that are between 200 μm and 1.5 mm in size and are evenly distributed throughout the matrix. Fine-grained quartz and biotite are included within the garnets whereas garnet grain boundaries appear unresorbed when adjacent to quartz, feldspar, some biotite and some sillimanite grains (Fig. 5.2a). Rarely, garnet grains are embayed where embayments contain biotite grains that are typically only a few 100 μm in length. In addition to this, some garnet grains have sillimanite growing in garnet embayments but are separated by a narrow quartz mantle (Fig. 5.2a).

Sillimanite aggregates in SkA 7-7 are disseminated and do not occur in distinct layers as in SkA 7-3 that occupy ~5 modal percent of the matrix. Sillimanite aggregates made up of fine-grained sillimanite needles (Fig. 5.2b) are elongated subparallel to the foliation and are between 0.5 mm and 4 mm long. The majority of sillimanite needles are subparallel to the foliation defined by biotite but some sillimanite grains are distinctly oblique to the foliation. Sillimanite is not limited to forming in dense aggregates and occurs as single, isolated grains when present in quartz or feldspar.

Biotite grain sizes vary between 20 μm and 2.5 mm in length and constitute about 30 modal percent of the sample. Coarse biotite grains are typically interconnected and have their long axes oriented subparallel to one another. Fine-grained crystals occur as isolated laths that occur between quartz, plagioclase and K-feldspar in the matrix. Similar to sample SkA 7-3, sparse and fine-grained ilmenite grains are present throughout the matrix in minor amounts (< 1 modal percent) and are commonly associated with biotite grains. This sample does not contain any spinel.

Framework silicates dominate the matrix: quartz (~40 %), plagioclase (~10 %) and K-feldspar (~5 %). Euhedral to anhedral varieties of fine-, medium- and coarse-grained quartz crystals are

present in the matrix and can be up to 2.5 mm in size. Plagioclase grains are evenly distributed throughout the matrix as medium-grained crystals (500 µm – 1 mm). Medium-grained K-feldspar is only present in leucosomes.

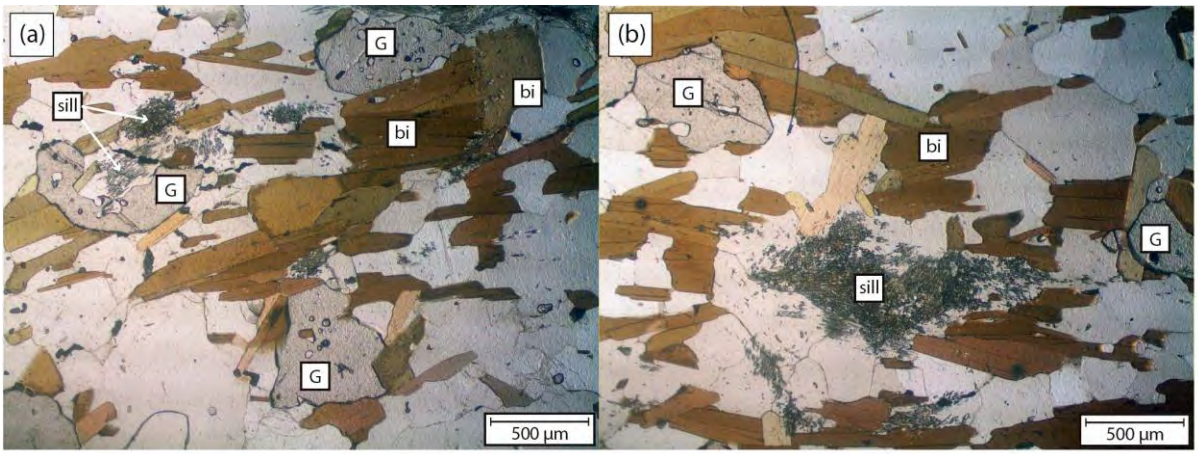

Figure 5.2: Photomicrographs of textures in sample SkA 7-7. (A) Garnet porphyroblasts adjacent to biotite and sillimanite with biotite in the matrix oriented subparallel to one another. (B) Fine-grained sillimanite needles constitute a sillimanite mat oriented subparallel to biotite.

5.1.3 Sample SkA 15-2

Similar to other metapelitic / metagraywacke samples, SkA 15-2 exhibits a fabric where medium- to coarse-grained biotite laths are strongly aligned but weakly interconnected. This biotite fabric uncommonly wraps around garnet porphyroblasts to form Θ-type porphyroblasts (Fig. 5.3a), whereas biotite that formed in garnet breakdown microstructures does not show a preferred orientation. Cummingtonite and ilmenite form a part of the matrix and leucosomes are subparallel to the foliation.

Subhedral garnet porphyroblasts together with anhedral, embayed garnet grains constitute 5-10 modal percent of the matrix and vary in size between 0.2-4 mm. Fine to medium-grained quartz, fine-grained biotite and plagioclase crystals occur in cracks and embayments on the margins of anhedral garnet porphyroblasts (Fig. 5.3a).

Large cummingtonite grains and smaller cummingtonite relics can be identified by their medium relief and under crossed polarised light they exhibit second order bright blue interference colours (Fig. 5.3b). More commonly, grains are comprised of well-developed polysynthetic twins. Large grains are up to ~4 mm long, whereas (Fig. 5.3b) relict grains can range between 400-800 µm. Relict cummingtonite grains are rarely adjacent to euhedral garnet

grain boundaries. Fine-grained biotite has formed in between and on the margins of large cummingtonite grains in the matrix. Altogether cummingtonite constitutes ~1-5 modal percent of the matrix.

Most biotite grains are disseminated and are between 50-500 µm long. Coarse-grained biotite up to 2 mm is present in areas where biotite is more concentrated and forms an interconnected foliation. Biotite makes up between 20-30 modal percent of the sample whereas subhedral to anhedral quartz and plagioclase grains make up 30-40 modal percent and 20-30 modal, respectively. Fine- to medium-grained quartz and plagioclase grains tend to be located in and around garnet breakdown microstructures as well as in the matrix. Coarse-grained quartz and plagioclase up to ~4 mm long is concentrated in leucosomes oriented parallel to the biotite foliation (Fig. 5.3c).

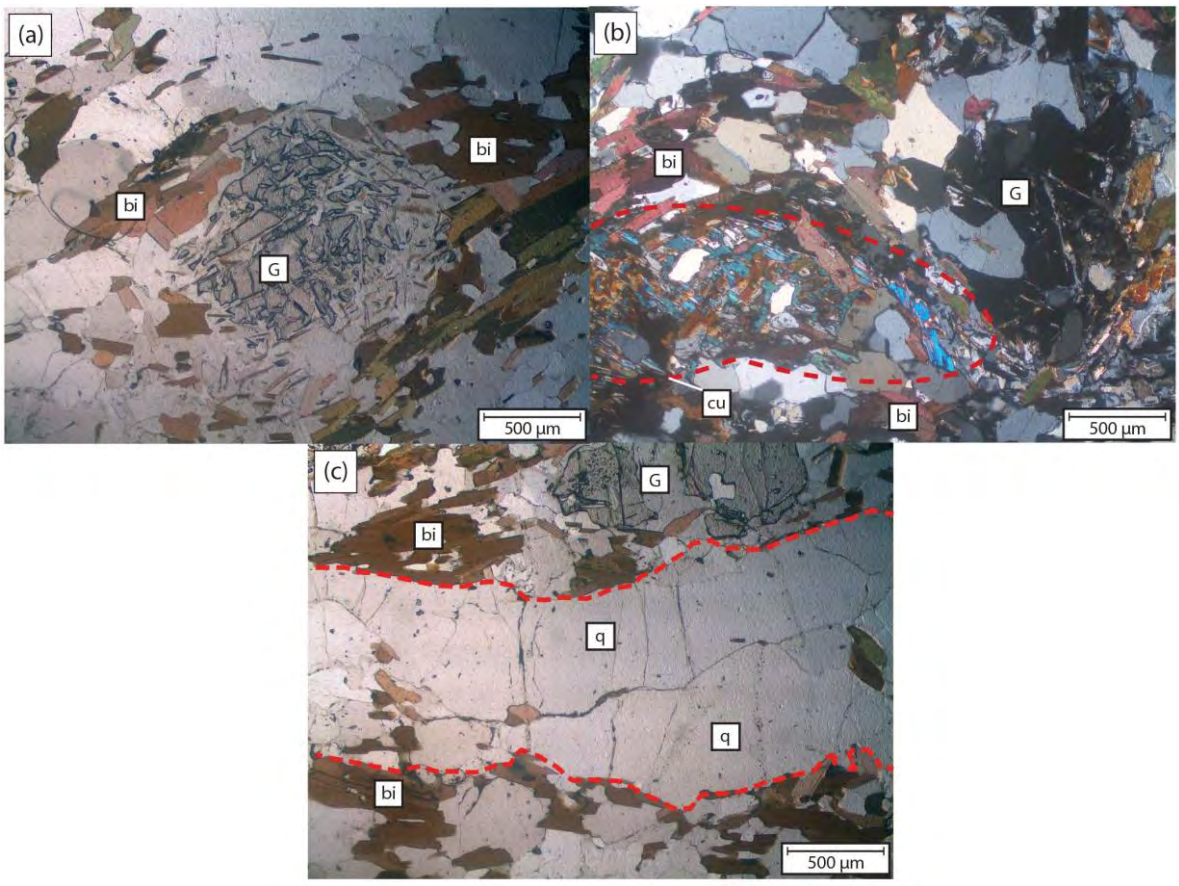

Figure 5.3: Photomicrographs representative of sample SkA 15.2. (A) Relict Θ-type porphyroblast where biotite is wrapped around a garnet grain. This image also exhibits a garnet-breakdown texture where garnet is severely resorbed. (B) Large cummingtonite (shown by red dashes) grain in the matrix. (C) Leucosome with irregular boundaries (red dashes) oriented subparallel to biotite in the matrix.

5.2 Petrography of metamafic samples

In addition to metapelitic samples, three metamafic samples were chosen to model the metamorphic history at Saltknappen. Samples SkA 10-1 and SkA 15-8 were taken from localities shown in Figure 4.2a whereas sample SkB 11-6 was retrieved from outcrop 'SkB' shown in Figure 4.8. Metamafic samples SkA 10-1 and SkA 15-8 have similar mineralogies and contain irregular garnet, hornblende, plagioclase, quartz, ilmenite, titanite and fine-grained cummingtonite. SkB 11-6 is different to these samples as it contains clinopyroxene, does not contain any cummingtonite and has a banded texture. Each sample will be described in more detail below.

5.2.1 Sample SkA 10-1

Anhedral garnet remnants and pseudomorphs after coarse-grained garnet (up to ~4 mm) make up between 20-30 modal percent of the matrix in this sample. Fine-grained quartz and ilmenite inclusions are visible in garnet grains but due to the degree of resorption of the garnet grains no conclusive evidence of hornblende or biotite inclusions could be found. Where garnet porphyroblasts are resorbed, plagioclase, quartz and less commonly hornblende form part of the mantle surrounding garnet grains (Fig. 5.4a).

Subhedral to anhedral, coarse-grained (up to 2.5 mm) hornblende grains form the majority of the matrix and are weakly to moderately aligned (Fig. 5.4b). They are characterised by yellow to light green pleochroism in plane polarised light and contain numerous quartz, ilmenite and plagioclase inclusions. Finer-grained (< 10 μm) varieties of hornblende form part of the garnet breakdown microstructures and are typically present on the rims of garnets. Fine-grained titanite (< 400 μm) oriented subparallel to hornblende (Fig. 4.4b), makes up < 1 modal percent of the sample, is mainly found as inclusions in hornblende but can also be found in association with ilmenite and plagioclase.

Subhedral to anhedral quartz and plagioclase make up 20-30 modal percent and 5-10 modal percent of the matrix, respectively. Quartz tends to be coarser grained in this sample and can be up to 1.5 mm long. However, both quartz and plagioclase are typically fine- to medium-grained and are found throughout the matrix, in garnet breakdown microstructures and as inclusions within hornblende.

Fine-grained ilmenite needles and euhedral aggregates are common throughout the sample and constitute ~2-5 modal percent. They are weakly aligned parallel to hornblende in the matrix. Predominantly fine-grained biotite grains that can be up to ~600 µm long form a part of the garnet breakdown textures and constitute the remaining ~2-3 modal percent of the sample. Biotite grains are weakly oriented in the same direction as the long axes of hornblende grains in the matrix. Minor amounts of fine-grained cummingtonite can be found on the margins of some hornblende in the matrix (Fig. 5.4c).

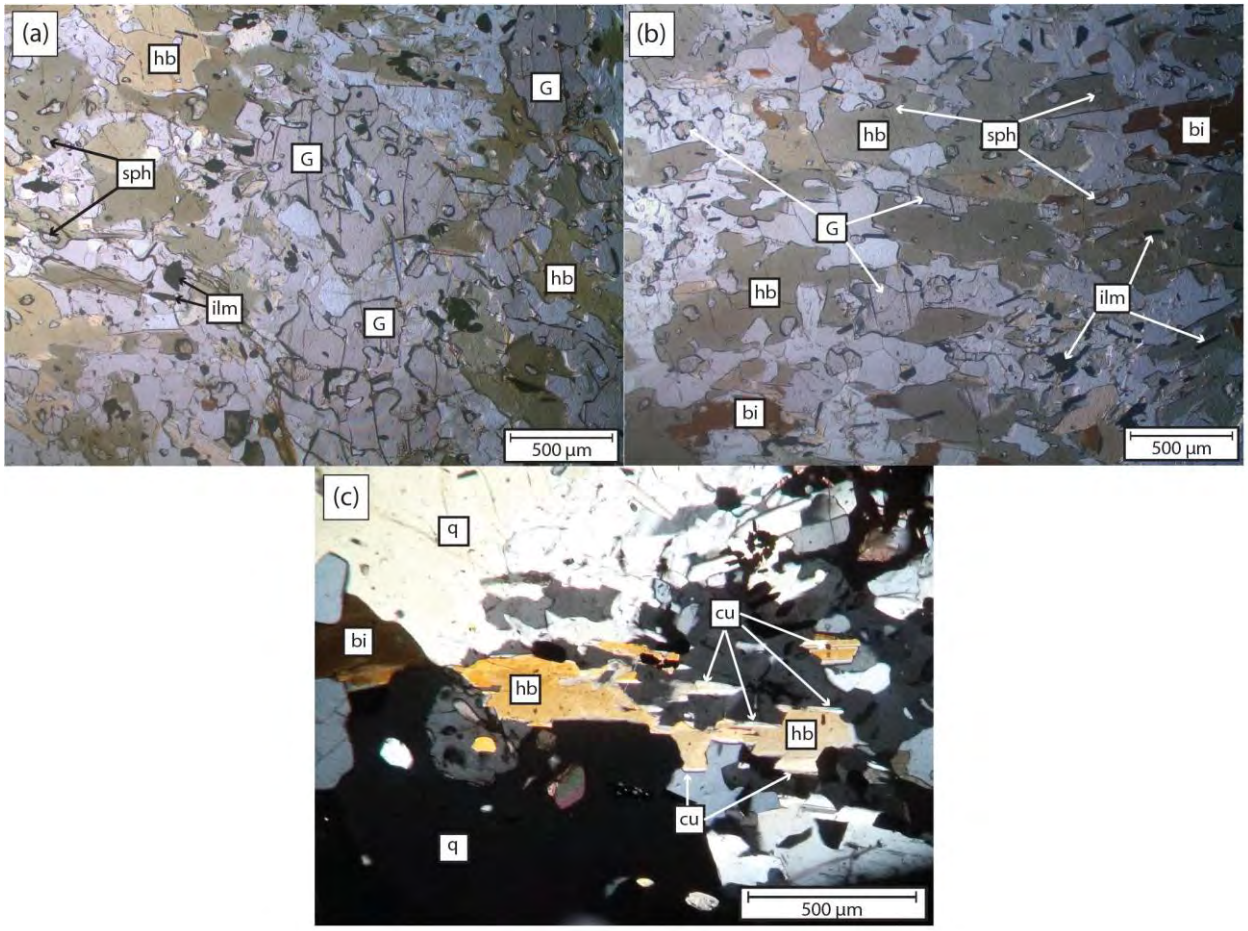

Figure 5.4: Photomicrographs representative of sample SkA 10-1. (A) Garnet-breakdown texture where garnet is dominantly mantled by plagioclase and quartz and less commonly hornblende. (B) Rounded and resorbed garnet. This image also shows weak to moderate alignment of ilmenite, titanite and hornblende grains. (C) Fine-grained cummingtonite forming rims on hornblende.

5.2.2 Sample SkB 11-6

Sample SkB 11-6 is comprised of hornblende-rich and quartz-plagioclase-rich layers, where both layers are strongly oriented in the same direction. Ilmenite and titanite are well aligned with hornblende whereas garnet is generally anhedral and found in quartz-plagioclase-rich areas.

Rounded and embayed garnet remnants (100 μm – 2 mm) are commonly encapsulated by a matrix of quartz and feldspar, and more rarely in contact with hornblende (Fig. 5.5a). Garnets contain no inclusions and make up less than ~3 modal percent of the matrix. Coarse-grained pseudomorphs after clinopyroxene and relict clinopyroxene porphyroblasts occur in the hornblende-rich areas of the matrix and constitute between 5-10 modal percent of the sample. They are up to ~1.5 mm large and can be identified by looking for a colourless to light green mineral in plane polarised light that has a strong cleavage in one direction. Ilmenite typically occurs along this cleavage and is associated with a hornblende-quartz symplectite after clinopyroxene (Fig. 5.5b). In rare cases where the clinopyroxene has not been completely altered to hornblende, the characteristic, bright, second order interference colours of clinopyroxene can be seen under cross-polarised light (Fig. 5.5c).

Subhedral to euhedral, coarse-grained hornblende forms about 50-60 modal percent of the matrix. Grains exhibit well-developed 120º cleavage as well as dark green to light brown pleochroism and vary in size between 100 μm and 2 mm. Aggregates (up to 1 mm long) of fine-grained ilmenite crystals are distributed throughout the matrix in hornblende-rich domains and constitute ~2-5 % of the sample. Both the long axes of the hornblende grains in the matrix and ilmenite aggregates are moderately to strongly oriented in the same direction (Fig. 4.5d). Minor amounts (< 1 modal percent) of rounded, fine-grained titanite also occurs in hornblende-rich regions of the sample (Fig. 5.5d).

The remaining minerals quartz and plagioclase constitute 10-20 % and ~20 % of the matrix, respectively. In this case, euhedral to subhedral plagioclase grains are larger than quartz grains and are between 100 μm and 2 mm in size in hornblende-poor domains. Quartz grains are typically only 100 μm – 1 mm big. Quartz and plagioclase in hornblende-rich domains are typically rounded and fine-grained.

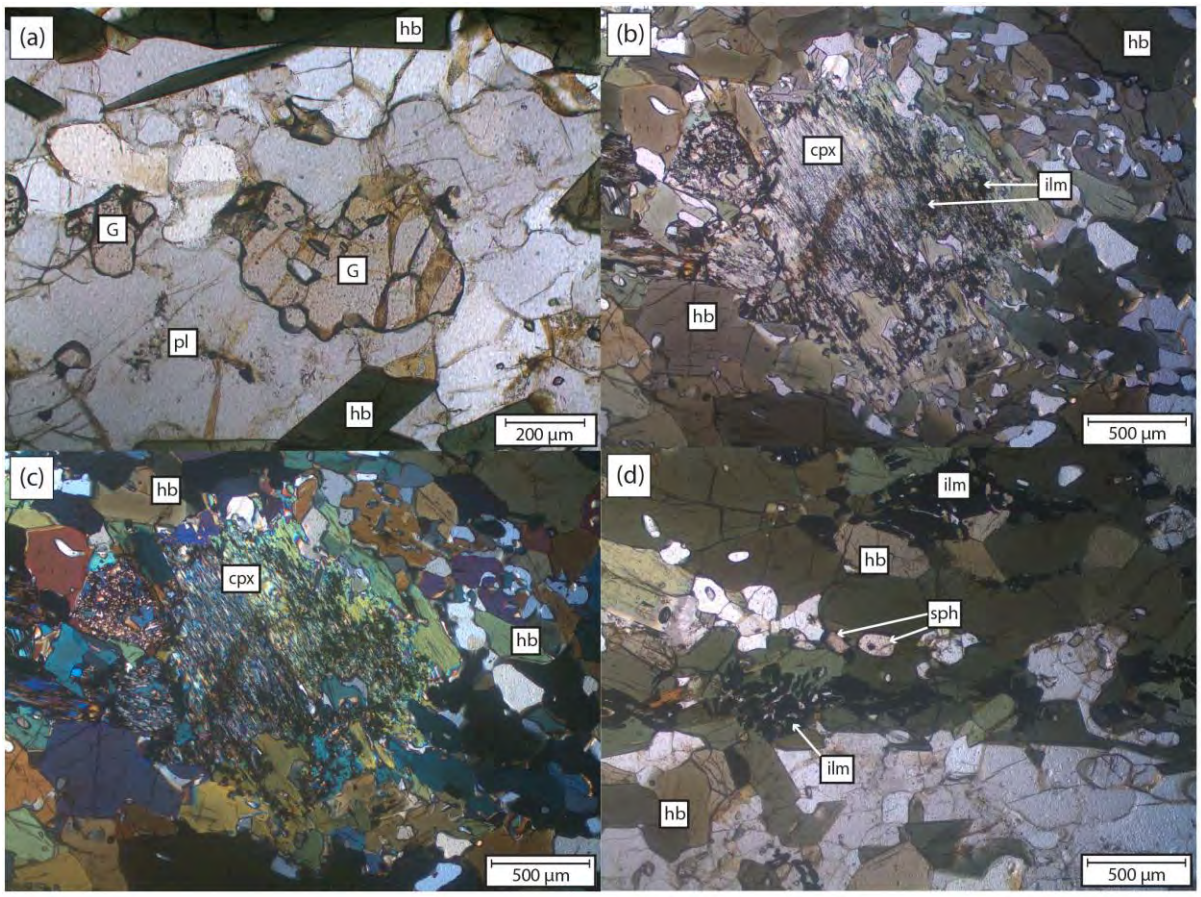

Figure 5.5: Photomicrographs representative of sample SkB 11-6. (A) Rounded garnet surrounded by plagioclase and quartz in a plagioclase-quartz-rich domain. (B) Relict clinopyroxene (diopside) partially pseudomorphed by hornblende, ilmenite and quartz (in PPL). (C) Bright second order interference colours of coarse-grained, relict clinopyroxene (in XPL). (D) Strongly oriented ilmenite aggregates in hornblende-rich domain. Fine-grained titanite inclusions in hornblende-rich domain (upper half). This image also shows the boundary between hornblende-rich and plagioclase-quartz-rich domains

5.2.3 Sample SkA 15-8

Resorbed, anhedral garnet grains between 1-2 mm can be found in rare cases. Here the garnet is surrounded by plagioclase, quartz and to a lesser extent hornblende (Fig. 5.6a). Garnet more commonly exists as fine-grained (< 200 μm), rounded relicts that remain after being resorbed (Fig. 5.6b). Approximately 1-3 modal percent garnet is present in the sample. Hornblende grains are mostly anhedral and fine- to coarse-grained with grain sizes between 50 μm and 5 mm. Fine-grained hornblende is found in plagioclase-rich domains where small garnet relicts are nearby. The long axes of hornblende grains are weakly aligned in the same direction and make up ~60-70 modal percent of the sample. Crystals exhibit a light green to yellow-green pleochroism and contain quartz, and titanite inclusions.

Titanite grains are sparse and only make up ~1 modal percent of the sample. They are typically less than 200 μm long, oval-shaped and occur throughout the matrix as inclusions in hornblende porphyroblasts (Fig. 5.6c). Quartz and plagioclase are fine-grained to medium-grained (< 500 μm to 1 mm) and are present as anhedral crystals. Quartz and plagioclase make up ~20 – 30 % and ~5 modal percent of the matrix, respectively.

The remainder of the matrix is comprised of biotite, cummingtonite and ilmenite. A variety of fine-grained to coarse grained (up to 2.5 mm) biotite grains overprint the matrix, are weakly oriented and occupy ~5 modal percent of the matrix area. Ilmenite is weakly-oriented, occurs throughout the matrix as fine-grained needles or aggregates and forms ~2 modal percent of the matrix. Cummingtonite can be recognised by black-yellow polysynthetic twinning and has formed on the margins of hornblende and biotite (Fig. 5.6d). Cummingtonite is typically fine-grained in this sample but grains up to ~0.8 mm in size were found.

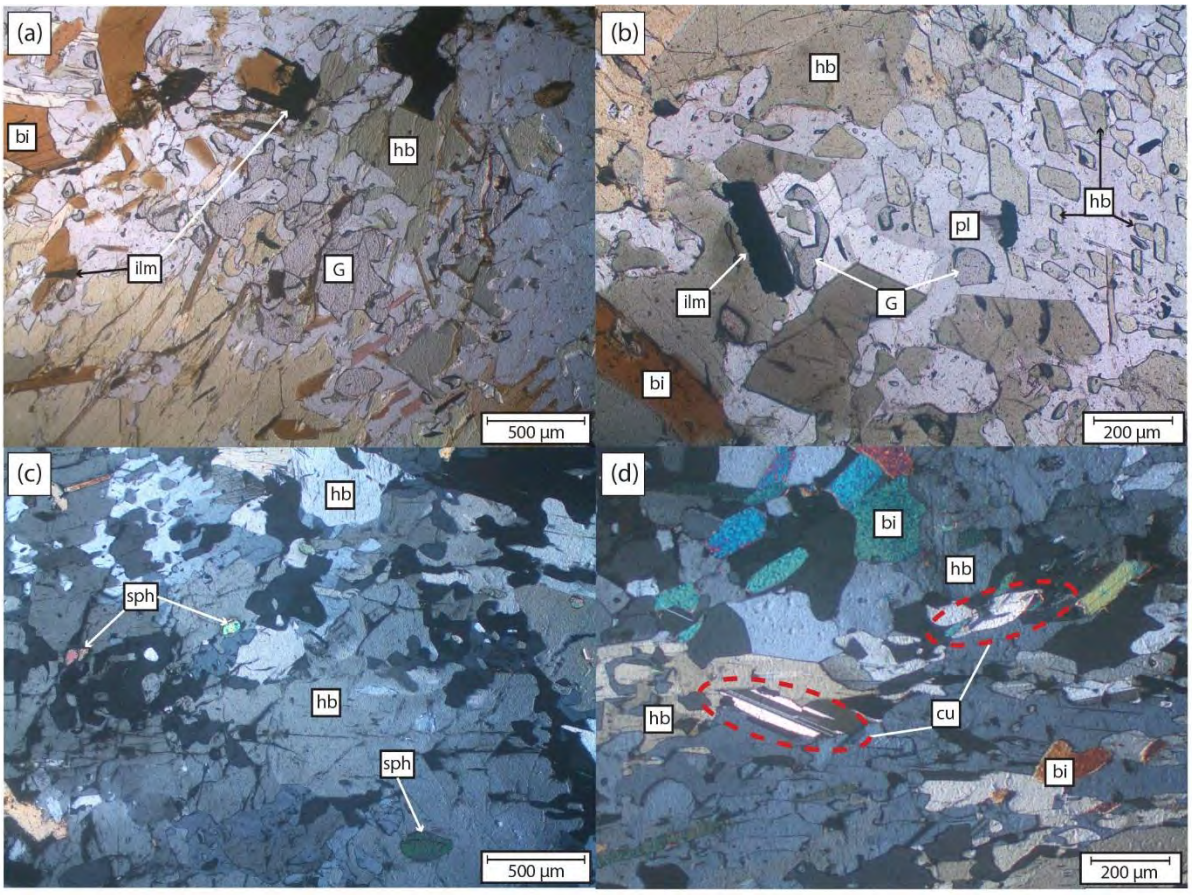

Figure 5.6: Photomicrographs representative of sample SkA 15-8. (A) Plagioclase-quartz mantle surrounding anhedral garnet. Weakly-oriented biotite and ilmenite overprinting the matrix. (B) Relict, anhedral garnet grains surrounded by plagioclase and quartz. Euhedral hornblende grains in the garnet-breakdown texture. (C) Fine-grained titanite inclusions in hornblende. (D) Fine-grained cummingtonite in the matrix associated with hornblende.

6. Mineral chemistry

The mineral assemblages in samples described in the petrography were deemed useful to help model the metamorphic history of the area. Electron microprobe (EMP) analyses were conducted on various minerals in each of the above-mentioned samples to determine the mineral chemistry and elucidate zoning within minerals. This can be used to determine the degree to which minerals are equilibrated and whether or not minerals grew over multiple generations.

Analyses were conducted by using a 'Jeol JXA – 8100 electron probe microanalyzer'. Analyses were done using an accelerating voltage of 15 kV, a beam current of ~20 nA and a spot size of ~20 μm. Peak counting times were 30 for Fe and 10 seconds for all elements investigated. Natural and synthetic standards were used to calibrate measurements made.

In metapelitic / metagraywacke samples (SkA 7-3, SkA 7-7 and SkA15-2) minerals analysed include garnet, biotite, plagioclase, spinel and cummingtonite. Minerals probed in mafic samples (SkA 10-1, SkB 11-6 and SkA 15-8) include garnet, hornblende, plagioclase, biotite and cummingtonite. A total of 225 EMP analyses were performed and are included in Appendix A.

Representative EMP oxide results and cation stoichiometry for major minerals in each of the 6 samples are highlighted and displayed in tables below. All Fe is measured as Fe^{2+} and assumed to be Fe^{2+} unless otherwise stated. Fe^{3+} has been taken into consideration and is estimated for minerals with relatively cation substitutions, i.e. garnet, ilmenite, spinel and pyroxenes, using the methodology in Droop, 1987. Formulae based on 12 oxygens for garnet, 11 oxygens for biotite, 23 oxygens for hornblende and cummingtonite, 8 oxygens for plagioclase, 6 oxygens for clinopyroxene, 3 oxygens for ilmenite and 4 oxygens for the spinel-group minerals.

Feldspar cation totals for calcium, potassium and sodium per an analysis are between 0.90 and 1. Totals below 0.95 are poor and indicate that one of the feldspar end-members was underestimated, therefore there is less confidence in the absolute values of X_{Ab} and X_{An}. Whereas most of the minerals analysed appear to be well-equilibrated a few minerals do exhibit zoning or differences between a given mineral in the matrix and in a garnet-breakdown structure (GBS). These minerals and differences are highlighted and significant differences are plotted on a graph or section through a mineral.

6.1 Mineral chemistry of metapelitic / metagraywacke samples

Table 6.1: Representative EMP results from minerals in sample SkA 7-3.

Sample	Salknappen , metapelitic sample SkA 7-3					
Mineral	Garnet		Plagioclase	Biotite	Spinel	Spinel
Location probed on mineral / in sample	Core	Rim	Matrix	Matrix	Matrix	Matrix
wt% oxide						
SiO2	37.41	37.45	62.86	34.63	0.01	0.00
TiO2	0.00	0.00	0.01	2.85	0.05	0.03
Al2O3	22.05	22.01	23.64	20.50	54.39	53.69
Cr2O3	0.03	0.03	0.00	0.07	0.38	0.55
FeO	33.13	33.64	0.03	21.39	15.31	15.30
Fe2O3	0.00	0.00	0.00	0.00	0.00	0.00
MnO	3.13	3.47	0.03	0.14	0.13	0.17
MgO	2.97	2.59	0.00	8.07	1.37	1.36
CaO	1.32	1.29	4.81	0.01	0.00	0.01
Na2O	0.00	0.00	8.09	0.38	1.17	0.95
K2O	0.00	0.00	0.16	9.81	0.00	0.00
Total	100.04	100.48	99.62	97.85	72.81	72.07
Cations						
Si	2.99	2.99	2.78	2.60	0.00	0.00
Ti	0.00	0.00	0.00	0.16	0.00	0.00
Al	2.08	2.07	1.23	1.81	2.27	2.27
Cr	0.00	0.00	0.00	0.00	0.01	0.02
Fe2+	2.22	2.25	0.00	1.34	0.45	0.46
Fe3+	0.00	0.00	-	-	0.00	0.00
Mn	0.21	0.23	0.00	0.01	0.00	0.01
Mg	0.35	0.31	0.00	0.90	0.07	0.07
Ca	0.11	0.11	0.23	0.00	0.00	0.00
Na	0.00	0.00	0.69	0.06	0.08	0.07
K	0.00	0.00	0.01	0.94	0.00	0.00
Total	7.97	7.97	4.95	7.83	2.90	2.89
Al^{IV}	-	-	-	1.40	-	-
Al^{VI}	-	-	-	0.41	-	-
X_{Fe}	-	-	-	0.60	0.86	0.86
X_{Alm}	0.77	0.77	-	-	-	-
X_{Spss}	0.07	0.08	-	-	-	-
X_{Py}	0.12	0.11	-	-	-	-
X_{Grss}	0.04	0.04	-	-	-	-
X_{An}	-	-	0.24	-	-	-
X_{Ab}	-	-	0.75	-	-	-

Table 6.2: Representative EMP results from minerals in sample SkA 7-7.

Sample	Salknappen , metapelitic sample SkA 7-7			
Mineral	Garnet		Plagioclase	Biotite
Location probed on mineral / in sample	Core	Rim	Matrix	Matrix
wt% oxide				
SiO2	37.51	37.35	62.72	35.30
TiO2	0.03	0.00	0.02	2.42
Al2O3	21.60	21.62	24.61	20.30
Cr2O3	0.01	0.06	0.00	0.04
FeO	34.17	34.34	0.05	21.60
Fe2O3	0.00	0.00	0.00	0.00
MnO	3.10	3.62	0.00	0.05
MgO	2.68	2.00	0.00	7.70
CaO	1.52	1.11	4.96	0.00
Na2O	0.01	0.04	7.84	0.28
K2O	0.00	0.00	0.22	9.88
Total	100.63	100.13	100.42	97.57
Cations				
Si	3.01	3.02	2.76	2.65
Ti	0.00	0.00	0.00	0.14
Al	2.04	2.06	1.27	1.80
Cr	0.00	0.00	0.00	0.00
Fe2+	2.29	2.32	0.00	1.36
Fe3+	0.00	0.00	-	-
Mn	0.21	0.25	0.00	0.00
Mg	0.32	0.24	0.00	0.86
Ca	0.13	0.10	0.23	0.00
Na	0.00	0.01	0.67	0.04
K	0.00	0.00	0.01	0.95
Total	8.00	8.00	4.95	7.80
Al^{IV}	-	-	-	1.35
Al^{VI}	-	-	-	0.45
X_{Fe}	-	-	-	0.61
X_{Alm}	0.78	0.80	-	-
X_{Spss}	0.07	0.09	-	-
X_{Py}	0.11	0.08	-	-
X_{Grss}	0.04	0.03	-	-
X_{An}	-	-	0.26	-
X_{Ab}	-	-	0.73	-

Metapelitic samples SkA 7-3 and SkA 7-7 do not display distinct zoning in any of the analysed minerals. Garnet cores have slightly higher X_{Py} and X_{Grss} values and slightly lower X_{Alm} and X_{Spss} values compared to their rims and exhibit very weak compositional zoning. Compositions representative of garnet cores are: $X_{Alm} = 0.75 – 0.78$, $X_{Spss} = 0.06 – 0.08$, $X_{Py} = 0.10 – 0.13$ and $X_{Grss} = 0.03 – 0.05$ whereas garnet rims typically have compositions where $X_{Alm} = 0.76 – 0.80$, $X_{Spss} = 0.06 – 0.09$, $X_{Py} = 0.08 – 0.12$ and $X_{Grss} = 0.03 – 0.04$.

Plagioclase displayed no zoning and has X_{An} values that range between 0.24 and 0.28. Biotite is unzoned and sample SkA 7-3 has Al^{VI} and X_{Fe} values between 0.41 – 0.44 cations per formula unit (c.p.f.u) and 0.60 – 0.61 respectively. Sample SkA 7-3 exhibits similar values to SkA 7-7 where Al^{VI} and X_{Fe} values are between 0.45 - 0.49 and 0.58 – 0.61, respectively. Sample SkA 7-3 contains Fe-rich (or possibly Zn-rich) spinel-group minerals. Total cations in spinel analyses are only ~ 70 wt% because analyses were not calibrated to quantify Zn or low totals could be due to the abundance of Fe_2O_3 in the mineral, which cannot be measured directly with the EMPA.

Metagraywacke sample SkA 15-2 displays the most significant zoning in garnet and plagioclase of the samples analysed. Similar to the garnet in samples SkA 7-3 and SkA 7-7, the cores are enriched in Mg and Ca relative to the garnet rims whereas Fe and Mn are enriched on the rims of the grains. Compositions of different elements in cores of garnet grains are: $X_{Alm} = 0.42 – 0.53$, $X_{Spss} = 0.01 – 0.03$, $X_{Py} = 0.21 – 0.26$ and $X_{Grss} = 0.23 – 0.34$ whereas garnet rims typically have compositions where $X_{Alm} = 0.55 – 0.63$, $X_{Spss} = 0.03 – 0.07$, $X_{Py} = 0.17 – 0.23$ and $X_{Grss} = 0.13 – 0.20$. Figure 6.1 shows a representative zoning profile through garnet from sample SkA 15-2. Plagioclase grains in the matrix also have different compositions to grains that form a part of garnet breakdown microstructures (GBS) (Fig. 6.2). Plagioclase from the matrix is more depleted in Ca and has X_{An} values between 0.26 and 0.39 whereas plagioclase from GBS are enriched in Ca and have X_{An} values between 0.44 and 0.71. Additionally, plagioclase grains from garnet breakdown microstructures are moderately zoned. Plagioclase rims adjacent to biotite in GBS have X_{An} values between 0.44 – 0.66. Cores and plagioclase rims adjacent to garnet in the GBS have X_{An} values between 0.64 – 0.65 and 0.63 – 0.71, respectively (Fig. 6.2). Biotite in the matrix and GBS is unzoned in SkA 15-2 and have Al^{VI} and X_{Fe} values between 0.22 – 0.27 c.p.f.u and 0.35 – 0.36. Biotite inclusions in garnet vary slightly in composition and have Al^{VI} and X_{Fe} values between 0.28 – 0.32 c.p.f.u and 0.25 – 0.31. Cummingtonite in the matrix typically has Al^{VI} and X_{Fe} values of 0.03 c.p.f.u and 0.40.

Table 6.3: Representative EMP results from minerals in sample SkA 15-2.

Sample	Salknappen , metagraywacke sample SkA 15.2					
Mineral	Garnet		Plagioclase		Biotite	Cummingtonite
Location probed on mineral / in sample	Core	Rim	Matrix	Garnet breakdown microstructures	Matrix	Matrix
wt% oxide						
SiO2	39.41	39.13	59.24	52.03	37.67	54.97
TiO2	0.08	0.02	0.00	0.00	2.73	0.08
Al2O3	22.54	22.41	26.69	31.65	16.99	1.04
Cr2O3	0.09	0.04	0.00	0.00	0.10	0.06
FeO	20.03	24.79	0.02	0.13	14.79	22.84
Fe2O3	0.00	0.00	0.00	0.00	0.00	0.00
MnO	0.64	1.42	0.05	0.01	0.08	0.72
MgO	6.66	5.92	0.00	0.04	14.51	19.19
CaO	11.10	6.76	7.57	12.71	0.07	0.66
Na2O	0.03	0.00	6.61	3.77	0.28	0.04
K2O	0.00	0.00	0.09	0.03	8.80	0.01
Total	100.57	100.49	100.28	100.37	96.03	99.63
Cations						
Si	2.99	3.01	2.63	2.35	2.77	7.85
Ti	0.00	0.00	0.00	0.00	0.15	0.01
Al	2.02	2.03	1.40	1.68	1.47	0.18
Cr	0.01	0.00	0.00	0.00	0.01	0.01
Fe2+	1.27	1.60	0.00	0.01	0.91	2.73
Fe3+	0.00	0.00	-	-	-	-
Mn	0.04	0.09	0.00	0.00	0.01	0.09
Mg	0.75	0.68	0.00	0.00	1.59	4.09
Ca	0.90	0.56	0.36	0.61	0.01	0.10
Na	0.00	0.00	0.57	0.33	0.04	0.01
K	0.00	0.00	0.01	0.00	0.83	0.00
Total	7.99	7.97	4.96	4.98	7.77	15.06
Al^{IV}	-	-	-	-	1.23	0.15
Al^{VI}	-	-	-	-	0.24	0.03
X_{Fe}	-	-	-	-	0.36	0.40
X_{Alm}	0.43	0.55	-	-	-	-
X_{Spss}	0.01	0.03	-	-	-	-
X_{Py}	0.25	0.23	-	-	-	-
X_{Grss}	0.30	0.19	-	-	-	-
X_{An}	-	-	0.39	0.65	-	-
X_{Ab}	-	-	0.61	0.35	-	-

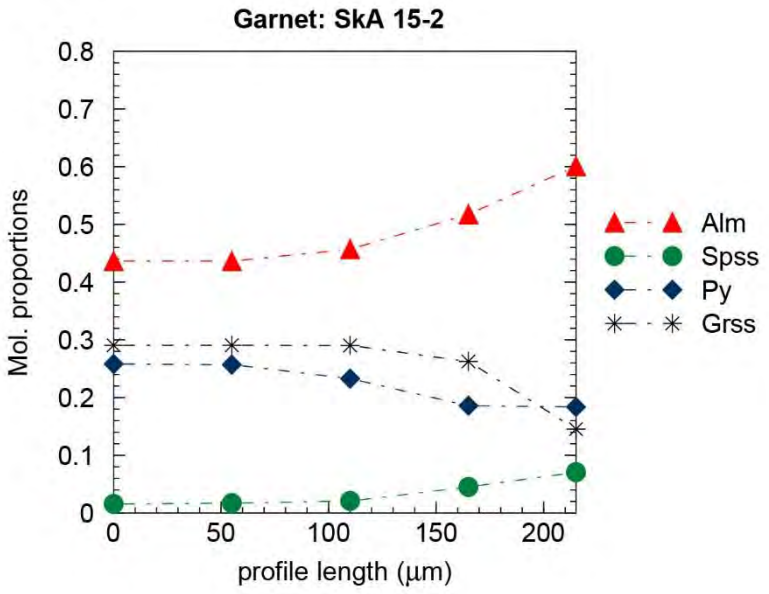

Figure 6.1: Representative zoning profile from *core to rim* in garnet from sample SkA 15-2

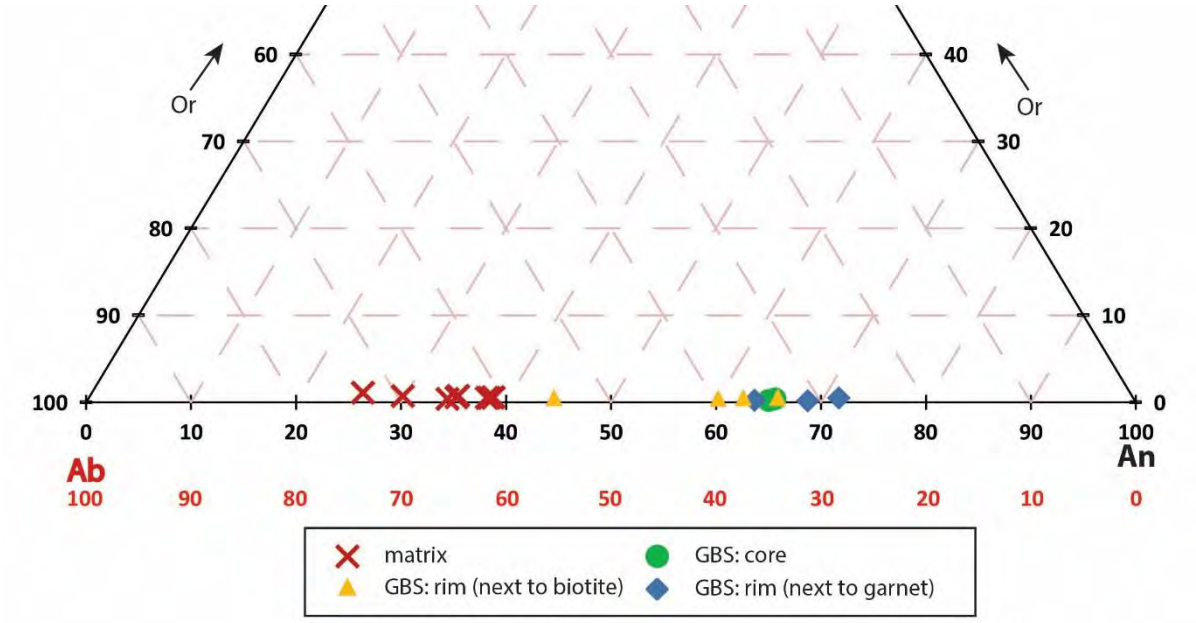

Figure 6.2: Ternary plot showing differences in plagioclase compositions between the matrix and garnet breakdown microstructures in SkA 15-2. The diagram also shows moderate zoning within plagioclase found in the matrix and garnet breakdown microstructures.

6.2 Mineral chemistry of metamafic samples

Table 6.4: Representative EMP results from minerals in sample SkA 10-1.

Sample	Salknappen , metamafic sample SkA 10-1							
Mineral	Garnet		Plagioclase	Hornblende		Biotite	Cummingtonite	Ilmenite
Location probed on mineral / in sample	Core	Rim	Matrix	Core	Rim	Matrix	Matrix	Matrix
wt% oxide								
SiO2	38.90	38.29	45.81	43.34	45.78	36.90	53.61	0.00
TiO2	0.04	0.01	0.00	1.56	1.19	3.52	0.10	52.18
Al2O3	22.27	22.05	35.75	13.35	11.31	16.15	1.13	0.00
Cr2O3	0.02	0.04	0.00	0.01	0.00	0.03	0.00	0.00
FeO	24.10	28.02	0.13	17.55	16.99	18.34	27.46	44.42
Fe2O3	0.00	0.00	0.00	0.00	0.00	0.00	0.00	2.01
MnO	0.88	2.03	0.02	0.24	0.17	0.02	0.61	0.64
MgO	4.60	3.10	0.00	9.30	10.15	12.26	15.31	0.41
CaO	9.72	6.89	17.48	11.50	12.35	0.00	0.90	0.10
Na2O	0.00	0.01	1.03	0.95	0.68	0.16	0.02	0.00
K2O	0.00	0.00	0.07	0.72	0.49	9.43	0.00	0.00
Total	100.52	100.44	100.29	98.53	99.11	96.82	99.13	99.75
Cations								
Si	3.00	3.01	2.10	6.43	6.71	2.75	7.87	0.00
Ti	0.00	0.00	0.00	0.17	0.13	0.20	0.01	0.97
Al	2.03	2.04	1.93	2.33	1.95	1.42	0.19	0.00
Cr	0.00	0.00	0.00	0.00	0.00	0.00	0.00	0.00
Fe2+	1.56	1.84	0.01	2.18	2.08	1.14	3.37	0.96
Fe3+	0.00	0.00	-	-	-	-	-	0.04
Mn	0.06	0.14	0.00	0.03	0.02	0.00	0.08	0.01
Mg	0.53	0.36	0.00	2.06	2.22	1.36	3.35	0.02
Ca	0.80	0.58	0.86	1.83	1.94	0.00	0.14	0.00
Na	0.00	0.00	0.09	0.27	0.19	0.02	0.01	0.00
K	0.00	0.00	0.00	0.14	0.09	0.90	0.00	0.00
Total	7.98	7.97	4.99	15.44	15.33	7.80	15.02	2.00
Al^{IV}	-	-	-	1.57	1.29	1.25	0.13	-
Al^{VI}	-	-	-	0.76	0.66	0.17	0.07	-
X_{Fe}	-	-	-	0.51	0.48	0.46	0.50	-
X_{Alm}	0.53	0.63	-	-	-	-	-	-
X_{Spss}	0.02	0.05	-	-	-	-	-	-
X_{Py}	0.18	0.12	-	-	-	-	-	-
X_{Grss}	0.27	0.20	-	-	-	-	-	-
X_{An}	-	-	0.90	-	-	-	-	-
X_{Ab}	-	-	0.10	-	-	-	-	-

Garnet in samples SkA 10-1 and SkA 15-8 exhibits moderate compositional zoning but not to the extent that garnet in sample SkA 15-2 does; however, the elements depleted and enriched at the rims are the same. Fe and Mn cation concentrations increase towards the rims of garnet whereas Mg and Ca decrease in concentration towards the rims. Typical compositions in the core are: X_{Alm} = 0.53 – 0.55, X_{Spss} = 0.02, X_{Py} = 0.16 – 0.18 and X_{Grss} = 0.26 – 0.28 whereas garnet rims typically have compositions where X_{Alm} = 0.63 – 0.65, X_{Spss} = 0.04 – 0.06, X_{Py} = 0.11 – 0.13 and X_{Grss} = 0.19 – 0.20. Figure 5.3 shows a zoning profile through garnet from sample SkA 15-8, representative for both SkA 15-8 and SkA 10-1.

Total aluminium content variations between cores and rims of hornblende indicates moderate to subtle compositional zoning in samples SkA 10-1 (Fig. 6.4) and SkA 15-8, respectively. Al^{VI} and X_{Fe} values in the cores of hornblende grains in SkA 10-1 range between 0.73 – 0.76 c.p.f.u and 0.50 – 0.52, respectively. Aluminium totals are slightly higher for hornblende cores in sample SkA 15-8 and range between 0.86 – 0.97 in the Al^{VI} site. The X_{Fe} value is similar at 0.48 – 0.49. Aluminium for analyses obtained at the rim of hornblende in SkA 10-1 are significantly lower than at the cores and Al^{VI}, X_{Fe} values are 0.65 – 0.71 c.p.f.u and 0.48 – 0.49, respectively. Aluminium at hornblende rims in sample SkA 15-8 is only slightly lower than at the cores and typically ranges between 0.84 – 0.86 and 0.47 – 0.48 for Al^{VI} and X_{Fe}.

Plagioclase is unzoned in SkA 10-1 and in SkA 15-8 and has a X_{An} value of 0.91 – 0.94. Biotite is also unzoned in both above-mentioned samples and sample SkA 10-1 has representative compositions between 0.13 – 0.17 and 0.46 – 0.50 for Al^{VI} and X_{Fe}, respectively. Sample SkA 15-8 exhibits similar values where Al^{VI} and X_{Fe} are between 0.16 – 0.18 and 0.42 – 0.43, respectively. Cummingtonite analyses from both samples SkA 10-1 and SkA 15-8 show similar Al^{VI} and X_{Fe} values that are between 0.02 – 0.07 and 0.44 – 0.50.

Table 6.5: Representative EMP results from minerals in sample SkA 15-8.

Sample	Salknappen , metamafic sample SkA 15-8					
Mineral	Garnet		Plagioclase	Hornblende	Biotite	Cummingtonite
Location probed on mineral / in sample	Core	Rim	Matrix	Matrix	Matrix	Matrix
wt% oxide						
SiO2	38.35	38.36	45.67	42.72	38.55	53.87
TiO2	0.04	0.00	0.00	1.49	3.35	0.09
Al2O3	21.48	21.12	35.31	14.64	15.61	1.00
Cr2O3	0.00	0.02	0.00	0.04	0.05	0.01
FeO	24.90	26.40	0.32	16.31	17.06	24.48
Fe2O3	0.00	0.00	0.00	0.00	0.00	0.00
MnO	2.15	3.40	0.05	0.21	0.10	0.93
MgO	4.04	3.40	0.04	9.46	12.83	17.26
CaO	9.05	7.03	17.83	10.13	0.02	1.09
Na2O	0.00	0.02	0.78	0.74	0.28	0.11
K2O	0.00	0.00	0.25	0.97	8.85	0.03
Total	100.01	99.76	100.25	96.71	96.70	98.87
Cations						
Si	3.01	3.04	2.10	6.39	2.84	7.84
Ti	0.00	0.00	0.00	0.17	0.19	0.01
Al	1.98	1.97	1.91	2.58	1.36	0.17
Cr	0.00	0.00	0.00	0.00	0.00	0.00
Fe2+	1.63	1.75	0.01	2.04	1.05	2.98
Fe3+	0.00	0.00	-	-	-	-
Mn	0.14	0.23	0.00	0.03	0.01	0.11
Mg	0.47	0.40	0.00	2.11	1.41	3.75
Ca	0.76	0.60	0.88	1.62	0.00	0.17
Na	0.00	0.00	0.07	0.21	0.04	0.03
K	0.00	0.00	0.01	0.19	0.83	0.00
Total	8.00	7.98	4.99	15.35	7.73	15.08
Al^{IV}	-	-	-	1.61	1.16	0.16
Al^{VI}	-	-	-	0.97	0.20	0.02
X_{Fe}	-	-	-	0.49	0.43	0.44
X_{Alm}	0.54	0.59	-	-	-	-
X_{Spss}	0.05	0.08	-	-	-	-
X_{Py}	0.16	0.13	-	-	-	-
X_{Grss}	0.25	0.20	-	-	-	-
X_{An}	-	-	0.91	-	-	-
X_{Ab}	-	-	0.07	-	-	-

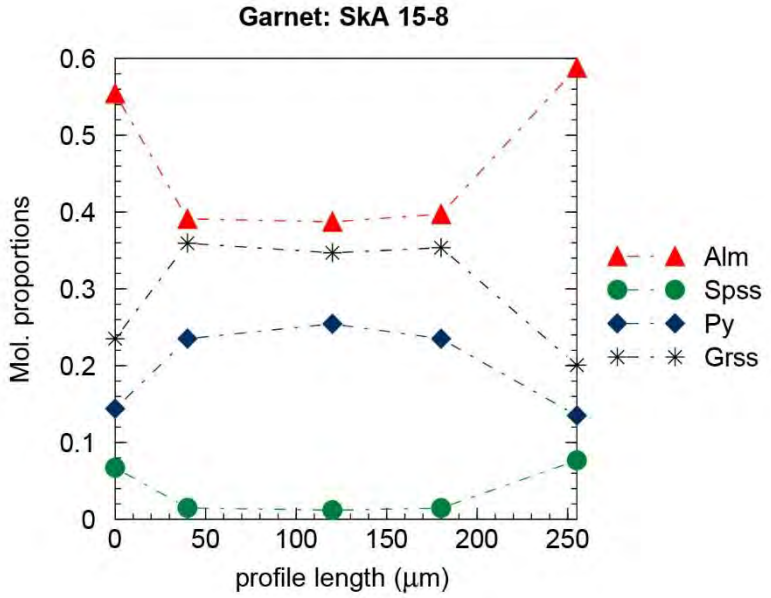

Figure 6.3: Profile through garnet representative of zoning in samples SkA 15-8 & SkA 10-1. Note: profile starts at the rim of a grain, passes through the core and ends at the opposite rim.

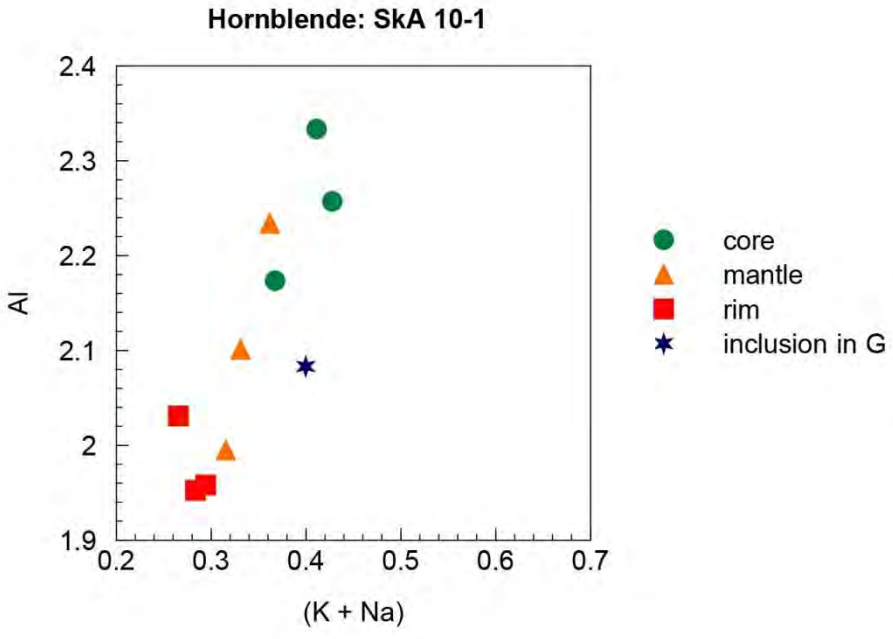

Figure 6.4: Plot of total aluminium cations against the sum of K and Na cations in hornblende from sample SkA 10-1. Al concentrations in the core are marginally higher than Al in the mantle and rim.

Table 6.6: Representative EMP results from minerals in sample SkB 11-6.

Sample	Salknappen , metamafic sample SkB 11-6					
Mineral	Garnet		Plagioclase	Hornblende	Diopside	Diopside
Location probed on mineral / in sample	Core	Rim	Matrix	Matrix	Matrix	Matrix
wt% oxide						
SiO2	38.38	38.52	59.47	42.41	52.99	52.56
TiO2	0.06	0.00	0.02	2.04	0.08	0.12
Al2O3	21.12	20.54	25.51	11.21	0.67	0.92
Cr2O3	0.00	0.04	0.00	0.00	0.03	0.02
FeO	25.15	25.70	0.04	21.54	12.32	12.86
Fe2O3	0.00	0.50	0.00	0.00	0.00	0.00
MnO	0.90	1.17	0.05	0.26	0.36	0.41
MgO	3.19	2.82	0.00	6.80	11.50	11.37
CaO	10.96	10.85	9.22	12.16	21.27	21.38
Na2O	0.03	0.06	5.58	1.19	0.22	0.24
K2O	0.00	0.00	0.20	1.06	0.00	0.03
Total	99.80	100.15	100.10	98.67	99.45	99.90
Cations						
Si	3.02	3.02	2.65	6.46	2.01	1.99
Ti	0.00	0.00	0.00	0.23	0.00	0.00
Al	1.96	1.90	1.34	2.01	0.03	0.04
Cr	0.00	0.00	0.00	0.00	0.00	0.00
Fe2+	1.65	1.72	0.00	2.75	0.39	0.41
Fe3+	0.00	0.03	-	-	0.00	0.00
Mn	0.06	0.08	0.00	0.03	0.01	0.01
Mg	0.37	0.33	0.00	1.54	0.65	0.64
Ca	0.92	0.91	0.44	1.99	0.86	0.87
Na	0.01	0.01	0.48	0.35	0.02	0.02
K	0.00	0.00	0.01	0.21	0.00	0.00
Total	8.00	8.00	4.93	15.57	3.98	3.99
Al^{IV}	-	-	-	1.54	-	-
Al^{VI}	-	-	-	0.48	-	-
X_{Fe}	-	-	-	0.64	0.38	0.39
X_{Alm}	0.55	0.57	-	-	-	-
X_{Spss}	0.02	0.03	-	-	-	-
X_{Py}	0.12	0.11	-	-	-	-
X_{Grss}	0.31	0.30	-	-	-	-
X_{An}	-	-	0.47	-	-	-
X_{Ab}	-	-	0.52	-	-	-

Garnet in sample SkB 11-6 exhibits no compositional zoning and representative values in the core are: $X_{Alm} = 0.55$, $X_{Spss} = 0.02$, $X_{Py} = 0.12$ and $X_{Grss} = 0.31$ whereas garnet rims typically have compositions where $X_{Alm} = 0.57$, $X_{Spss} = 0.03$, $X_{Py} = 0.11$ and $X_{Grss} = 0.30$. Plagioclase is also unzoned where compositions are typically $X_{An} = 0.46 – 0.47$. Hornblende grains that form a part of garnet breakdown microstructures exhibit subtle compositional variations between cores and rims. Aluminium concentrations are marginally higher in the cores where Al^{VI} and X_{Fe} values range between 0.62 – 0.64 c.p.f.u and 0.64 – 0.65, respectively. Al^{VI} and X_{Fe} values are typically between 0.57 – 0.61 c.p.f.u and 0.62 – 0.63, respectively. Al^{VI} and X_{Fe} values from the matrix overlap values found in the cores and rims of hornblende from GBS's where representative values are between 0.48 – 0.56 c.p.f.u and 0.62 – 0.64, respectively. Compositions obtained for pyroxene found in SkB 11-6 are uniform and no zoning is distinguished. Half of the analyses plot in the diopside field whereas the others plot in the augite field. Clinopyroxene compositions show a slight Ca deficiency and minor solid solution towards clino-enstatite.

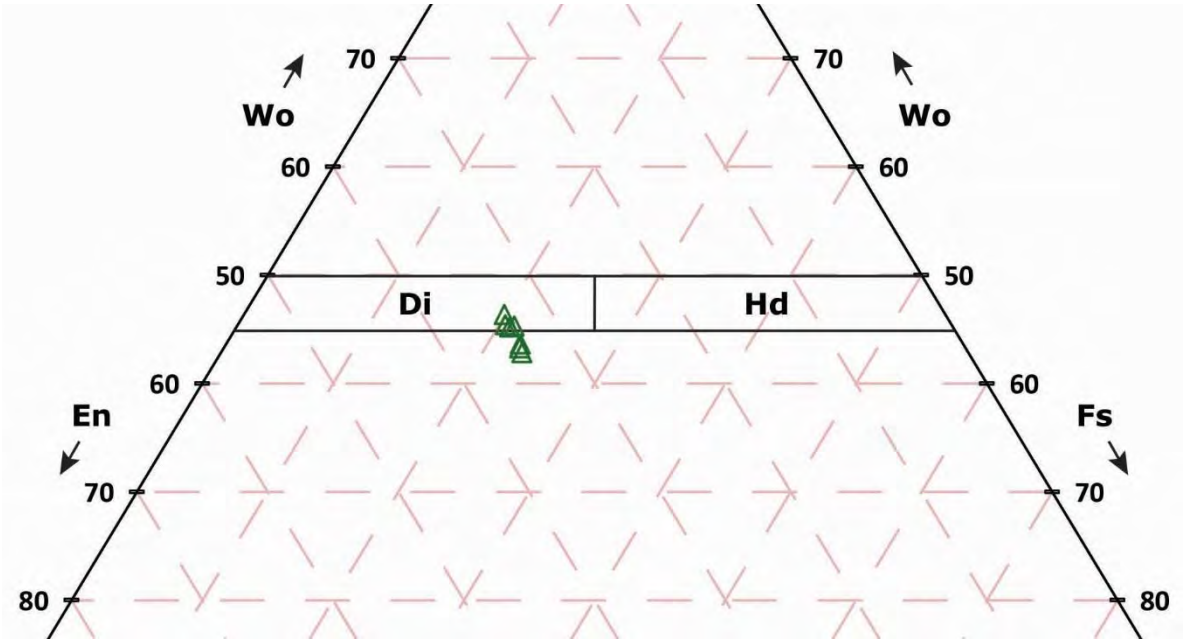

Figure 6.5: Pyroxene ternary diagram showing the variation in clinopyroxene compositions (green triangles) in sample SkB 11-6. Nomenclature is taken from Morimoto *et al.* (1988).

7. Inferred equilibrium mineral parageneses

Minerals present in metapelitic and metamafic samples have been described; however, some inference needs to be made as to which minerals constitute equilibrium assemblages. The paragenesis of each of the metapelitic / metagraywacke samples is necessary to be able to initiate phase diagram modelling, to determine which of the phase fields most likely represents peak metamorphic conditions and which assemblages were formed during retrogression.

7.1 Metapelitic / metagraywacke rocks

Partial melting and melt migration removes a volatile-bearing melt phase from the rocks and consequently allows the near-solidus assemblages to be preserved (White and Powell, 2002; 2010). The lack of hydrous retrograde minerals such as muscovite and chlorite in SkA 7-3, SkA 7-7 and SkA 15-2 suggests that substantial melt loss has occurred and that the peak assemblages are largely preserved.

The matrix of metapelitic samples SkA 7-3 and SkA 7-7 is characterised by biotite grains, sillimanite aggregates, quartz and plagioclase grains that are similar in size and have straight grain boundaries when in contact with one another. Garnet porphyroblasts are slightly larger but are also equally distributed throughout the matrix and typically have straight grain boundaries when in contact with biotite, sillimanite, quartz, plagioclase and K-feldspar. The major minerals (garnet, biotite and plagioclase) probed in metapelitic samples SkA 7-3 and SkA 7-7 do not exhibit any significant zoning from the cores to rims of mineral grains. The lack of zoning between minerals is an indication that these minerals were in equilibrium with one another. Therefore they are inferred to form an equilibrium assemblage that most likely reflects peak metamorphic conditions. Ilmenite is difficult to see in metapelitic / metagraywacke samples but is typically associated with biotite and since biotite is present throughout the matrix it is assumed that ilmenite is also part of the peak assemblage.

Relatively fine-grained K-feldspar is present in magmatic leucosome structures in SkA 7-3 and SkA 7-7, which suggests that partial melting has occurred in both samples. Coarse-grained spinel that is present throughout the matrix in sample SkA 7-3, has relatively straight grain boundaries in contact with garnet, sillimanite, biotite, plagioclase and quartz, and is also considered part of the equilibrium assemblage in sample SkA 7-3. Sillimanite mats are comprised of fine-grained needles and suggests that the sillimanite is possibly pseudomorphed

after another aluminium-rich silicate such as kyanite, andalusite or staurolite, (e.g. Hollister, 1969; Brown and Raith, 1996). In this case the sillimanite is most likely pseudomorphed after kyanite because during prograde to early peak metamorphism the inferred peak assemblage is stable in the kyanite field (see below). Kyanite has also been described in other outcrops within Sverdrupfjella (Board *et al.*, 2005), and it is therefore likely that large parts of the metamorphic history of these rocks could have occurred at conditions of kyanite stability, before it was replaced by sillimanite. It is possible that either kyanite or sillimanite could have been present during peak metamorphism, and therefore the peak assemblages will be taken to contain either sillimanite or kyanite. Biotite grains wrap around garnet porphyroblasts and where garnet overprints the biotite in the matrix. Therefore garnet most likely formed late during the prograde history after a dominant biotite fabric had formed and is also part of the equilibrium assemblage. The inferred peak assemblage for SkA 7-3 consequently is: garnet, biotite, sillimanite / kyanite, quartz, plagioclase, K-feldspar, spinel, ilmenite and melt, whereas the peak assemblage for SkA 7-7 is: garnet, biotite, sillimanite or kyanite, quartz, plagioclase, K-feldspar, ilmenite and melt.

Metagraywacke sample SkA 15-2 contains biotite, ilmenite, garnet, cummingtonite, plagioclase and quartz grains throughout the matrix that are in mutual contact with one another, have straight grain boundaries and are not limited to any particular domain within the sample. Biotite grains in the matrix are subparallel and garnet porphyroblasts overprint the foliation-defining biotite. Biotite grains also wrap around garnet porphyroblasts, which suggests that this biotite formed / recrystallised later in the tectonic history after the garnet had formed.

The only significant compositional variations in minerals from sample SkA 15-2 occur in garnet and plagioclase. The garnet zoning profiles exhibited by metagraywacke sample SkA 15-2 are characteristic of retrograde zoning (Tracy and Robinson, 1976; Tuccillo *et al.*, 1990). During peak metamorphism and prior to retrogression, these zoning profiles were most likely flat with a similar composition to that preserved in the core. The garnet was therefore in equilibrium with the peak assemblage in sample SkA 15-2. Plagioclase in the garnet breakdown microstructures is enriched in Ca relative to the plagioclase in the matrix. The Ca enrichment in plagioclase comes from diffusion with garnet as garnet rims are significantly depleted in Ca, eg. Liu and Zhong (1997). The plagioclase in the matrix is depleted in Ca and represents the most likely composition of plagioclase that was in equilibrium with the peak assemblage. Leucosomes that contain quartz and plagioclase are oriented subparallel to the dominant

foliation in the rock and suggests that the rock was melt-bearing at the same metamorphic conditions that formed the equilibrium assemblage.

Therefore, the major minerals in the matrix form part of the equilibrium assemblage with retrograde zoning only affecting the rims of garnet and the composition of plagioclase in the garnet breakdown microstructures. The inferred equilibrium assemblage in sample SkA 15-2 is therefore garnet, biotite, cummingtonite, quartz, plagioclase, ilmenite and melt.

7.2 Metamafic rocks

Metamafic rocks are dominated by hornblende and plagioclase whereas garnet, ilmenite, titanite and quartz are present in smaller volumes. Clinopyroxene is present in sample SkB 11-6. Samples SkA 10-1 and SkA 15-8 have similar mineralogies and textures and have hornblende, plagioclase, ilmenite and quartz occurring throughout the samples. Most major minerals in metamafic samples SkA 10-1 and SkA 15-8 show little to no compositional variation. Sample SkA 10-1 shows a significant variation of the Al composition in hornblende, and both SkA 10-1 and SkA 15-8 exhibit moderate compositional zoning in garnet. In sample SkA 10-1, the concentration of aluminium in hornblende from the matrix is significantly higher in the cores and diminishes towards the rims. In metamafic rocks the aluminium content in hornblende typically increases with metamorphic grade, (e.g. Raase *et al.*, 1986). Therefore, the lowered Al content at the rims of hornblende in the matrix of sample SkA 10-1 implies that the zoning was formed during the retrogression. The garnet in samples SkA 10-1 and SkA 15-8 exhibit similar zoning profiles to the garnet in metagraywacke sample SkA 15-2, where the concentrations of Mn and Fe increase towards the rim. In metamafic rocks, growth zoning in garnet is typically characterised by a decrease in Mn and Fe towards rim, (e.g. Faak *et al,* 2012). Therefore, the zoning in samples SkA 10-1 and SkA 15-8 formed during the retrograde path.

In samples SkA 10-1 and SkA 15-8, fine-grained cummingtonite can be found on the margins of hornblende when closely associated with plagioclase and ilmenite. This occurs throughout the matrix in areas that are not limited to garnet breakdown microstructures. Cummingtonite is not considered to be part of the peak assemblages because it is fine-grained, incipient and is restricted to the rims of some hornblende grains in the matrix.

Where garnet porphyroblasts still preserve straight grain boundaries in sample SkA 10-1, hornblende, plagioclase and quartz that are roughly equigranular are adjacent to garnet in the

garnet breakdown microstructures. These equigranular minerals show no preferential orientation, are finer-grained than the minerals in the matrix and are limited to areas surrounding resorbed garnets. Thus, the minerals in the garnet breakdown microstructures most likely formed during retrogression after peak metamorphism where garnet was present together with the other minerals in the matrix. Fine grained ilmenite needles and titanite are abundant throughout the matrix and also have straight grain boundaries when adjacent to unresorbed garnet porphyroblasts. No leucosomes are present. The inferred peak equilibrium assemblage in sample SkA 10-1 is therefore made up of hornblende, plagioclase, quartz, garnet, ilmenite, titanite and fluid (H_2O).

Retrogression of this sample resulted in the depletion of Al in hornblende and retrograde garnet zoning profiles, as well as the resorption of garnet and the development of fine cummingtonite overgrowths on matrix hornblende. The partially-developed retrograde assemblage in sample SkA 10-1 therefore consists of hornblende, cummingtonite, plagioclase and ilmenite.

Sample SkA 15-8 contains less garnet in the matrix than sample SkA 10-1 and where garnet is present, they are resorbed and very rarely preserve straight grain boundaries. Roughly equigranular hornblende, plagioclase and quartz are present adjacent to straight grain boundaries of garnet. Titanite is present throughout the matrix and is also found in close proximity to garnet where straight grain boundaries are present. There is less ilmenite present in sample SkA 15-8 compared to SkA 10-1 but in SkA 15-8 it is also present throughout the matrix and can be found in garnet breakdown structures. It is therefore uncertain whether or not ilmenite formed a part of the peak assemblage in sample SkA 15-8. The inferred equilibrium peak metamorphic assemblage of sample SkA 15-8 is made up of hornblende, plagioclase, quartz, garnet, titanite and fluid (H_2O) with or without ilmenite.

Retrogression in samples SkA 15-8 resulted in the depletion of Al in hornblende and the formation of retrograde zoning profiles in garnet, as well as the development of fine cummingtonite grains on the margins of matrix hornblende. This retrograde assemblage is partially-developed and consists of hornblende, cummingtonite, plagioclase and ilmenite.

The lack of compositional zoning of the major minerals probed in the metamafic sample SkB 11-6 suggests that the minerals are in equilibrium with one another. The peak assemblage in sample SkB 11-6 is therefore decided based on textural grounds. In sample SkB 11-6, hornblende, ilmenite aggregates, titanite, coarse-grained clinopyroxenes and the plagioclase-quartz-rich domains are all moderately to strongly aligned subparallel to one another and are

considered to be a part of the peak assemblage. Titanite, however, only occurs as inclusions in hornblende. Garnet relicts are common throughout the sample and straight grain boundaries can be seen in association with plagioclase, quartz, hornblende and ilmenite. Rare examples exist where pseudomorphs after diopside are adjacent to the extent of garnet breakdown structures and it is inferred that garnet and clinopyroxene were also a part of the equilibrium peak assemblage. No evidence of quartz-plagioclase leucosomes were found. The inferred peak assemblage is therefore garnet, hornblende, diopside, ilmenite, plagioclase, quartz and fluid (H_2O) with or without titanite. Titanite might have been a part of the peak assemblage but may also have remained as an inclusion within hornblende and 'survived' re-equilibration once it became metastable during inferred peak conditions.

8. Phase diagram modelling

Three metapelitic / metagraywacke samples and three metamafic samples were chosen to constrain pressure-temperature (P-T) conditions through pseudosection calculations. These choices were based on useful mineral assemblages, textures and the presence of relict garnet in these samples. The metapelitic / metagraywacke samples modelled for P-T conditions are namely: SkA 7-3, SkA 7-7, SkA 15-2 and metamafic samples include: SkA 10-1, SkB 11-6 and SkA 15-8.

Samples were prepared for X-ray Fluorescence Spectrometry (XRF) analysis at the University of Cape Town to determine the concentration of the major oxides in each sample. The results of the XRF analyses are shown in Table 8.1.

Table 8.1: XRF bulk composition results for six of the samples collected at Saltknappen

	SkA 7.3	SkA 7.7	SkA 15.2	SkA 10.1	SkB 11.6	SkA 15.8
SiO_2	64.77	63.98	62.16	53.75	49.90	48.51
TiO_2	0.89	0.86	0.84	1.75	2.16	1.04
Al_2O_3	14.28	13.93	14.53	14.32	14.34	14.99
Fe_2O_3	9.75	11.83	7.19	14.69	15.30	12.92
MnO	0.18	0.27	0.12	0.27	0.20	0.30
MgO	2.49	2.84	5.19	5.45	4.63	8.04
CaO	1.55	0.98	3.74	7.42	9.41	11.61
Na_2O	2.54	1.26	1.66	0.46	2.83	0.77
K_2O	2.96	3.22	2.79	1.01	0.61	0.55
P_2O_5	0.23	0.17	0.26	0.18	0.24	0.10
SO_3	0.01	-	-	0.00	0.01	0.14
Cr_2O_3	0.02	0.02	0.04	0.01	0.00	0.02
NiO	0.01	0.01	0.03	0.02	0.01	0.02
H2O-	0.11	0.15	0.16	0.10	0.10	0.17
LOI	0.46	0.39	0.66	0.44	-0.03	0.56
Total	100.24	99.91	99.35	99.84	99.71	99.74

LOI = loss of ignition, "**-**"= below detection limit

P_2O_5, SO_3, Cr_2O_5 and NiO components were disregarded for phase diagram calculations because they are only present in minor amounts in all of the samples analysed and it was assumed that they would have insignificant effects on phase equilibria. MnO was also ignored because it only has a notable effect on the stability of garnet in low to medium grade rocks, e.g. (Mahar *et al.*, 1997). K_2O was omitted in mafic rocks because it is only present in minor amounts. Metapelitic and metagraywacke rocks were modelled using the NCKFMASHTO (Na_2O-CaO-K_2O-FeO-MgO-Al_2O_3-SiO_2-H_2O-TiO_2-O) system whereas metamafic rocks were modelled using the NCFMASHTO system. The Fe_2O_3 (O) component was estimated by

considering the $Fe_2O_3/(Fe_2O_3 + FeO)$ ratio as described in Rebay *et al.* (2010) and White *et al.* (2014). For metapelitic and mafic rocks oxide values were assigned so that the $Fe_2O_3/(Fe_2O_3 + FeO)$ ratios were between 0.05 – 0.15 and 0.10 – 0.25, respectively (e.g. Rebay *et al.*, 2010). H_2O was assumed to be in excess in metamafic samples because there is currently no reliable melt model for mafic rocks. Metapelitic rocks have undergone partial melting and have lost melt to some degree, therefore their current composition is that of a melt-depleted residuum. For these assemblages to be preserved, they must have equilibrated at the residuum solidus in the presence of the remaining melt, e.g. (White *et al.*, 2001, 2004). Therefore the fluid contents were selected to stabilise the inferred peak assemblages in metapelitic / metagraywacke rocks at the residuum solidus.

Several assumptions were made before modelling phase diagrams. It was assumed that XRF bulk compositions were representative of the composition of the equilibration volume due to the fact that metapelitic and metagraywacke rocks experienced granulite facies temperatures during peak metamorphism. It was assumed that until partial melting occurred, metapelitic and metagraywacke rocks were H_2O-saturated and in metamafic rocks the samples were always H_2O-saturated. For pelitic rocks, the H_2O content was chosen such that the inferred peak assemblages were stable immediately above the residuum solidus. Furthermore, the spinel found in sample SkA 7-3 was not considered in phase diagram calculations because Zn was not measured during XRF analysis and reliable activity-composition models for Zn-spinel are not available. Bulk compositions used to model P-T conditions are given in Table 8.2. Values in Table 8.2 represent molar proportions of oxides that have been converted from wt% oxides measured by XRF.

Table 8.2: Bulk compositions used to create the pseudosections.

		SiO_2	TiO_2	Al_2O_3	FeO	MgO	CaO	Na_2O	K_2O	O	H_2O
SkA 7-3	**P**	71.24	0.73	9.26	8.07	4.08	1.83	2.70	2.08	0.40	2.00
SkA 7-7	**P**	70.85	0.71	9.09	9.86	4.69	1.17	1.36	2.27	0.30	3.00
SkA 15-2	**P**	67.64	0.69	9.32	5.89	8.42	4.36	1.75	1.94	0.30	3.90
SkA 10-1	**M**	59.02	1.44	9.27	12.14	8.91	8.73	0.49	-	1.00	excess
SkB 11-6	**M**	54.71	1.78	9.27	12.63	7.56	11.05	3.00	-	1.40	excess
SkA 15-8	**M**	52.16	0.84	9.50	10.45	12.88	13.37	0.80	-	0.60	excess

Note: P = metapelitic sample, M = metamafic sample

Phase diagram modelling was done by using THERMOCALC v3.37 (Powell and Holland, 1988, released 12/12/2011) and the new internally consistent dataset (Holland and Powell, 2011), (file: tc-ds62.txt, updated 06/02/2012). The activity-composition models used for phase

diagram modelling are those of White *et al.* (2014), with quartz, kyanite, sillimanite, titanite (titanite), rutile and aqueous fluid (H_2O) taken to be pure end-member phases. The activity-composition models for amphibole and clinopyroxene are unpublished updates of the Diener and Powell (2012) models suitable for use with the Holland and Powell (2011) dataset.

Pseudosections were constructed between 600 – 900 ºC and 3 – 15 kbar (sample SkA 15-8 pressure ranges were from 2.5 – 15 kbar). Pseudosections are presented in figures 7.1 – 7.6. Phase fields containing the inferred peak assemblages are shaded in green. In metapelitic / metagraywacke samples the solidus is represented by the black, dashed line.

8.1 Pseudosections modelled for metapelitic / metagraywacke samples

8.1.1 Metapelitic sample SkA 7-3

The pseudosection for sample SkA 7-3 is characterised by high-variance assemblages that each have a relatively large P-T stability. Garnet, quartz, plagioclase, K-feldspar and ilmenite are stable throughout the P-T conditions in the diagram. The solidus is between ~760 – 790 ºC; at pressures > 5 kbar aluminosilicates are lost above ~800 ºC and biotite is lost at temperatures between ~800 – 850 ºC. Cordierite is only stable at pressures below ~5.2 kbar and at temperatures less than ~830 ºC whereas magnetite is present below ~5-7 kbar at temperatures less than ~850 ºC. Muscovite is introduced at ~9.5 kbar at temperatures below ~760 ºC and is present at high pressures at temperatures below 760 – 830 ºC. Kyanite is replaced by muscovite above ~10 – 13.8 kbar at temperatures below ~760 ºC.

The inferred peak assemblage of garnet-biotite-kyanite/sillimanite-ilmenite-plagioclase-K-feldspar-quartz-melt is stable over a narrow temperature range between 780 and 820 ºC, at pressures between 5 and 13 kbar. The assemblage is bounded by the solidus to lower temperatures, whereas aluminosilicates are removed at higher temperatures and the lower pressure limit of the peak assemblage is constrained by the introduction of cordierite (Fig. 8.1).

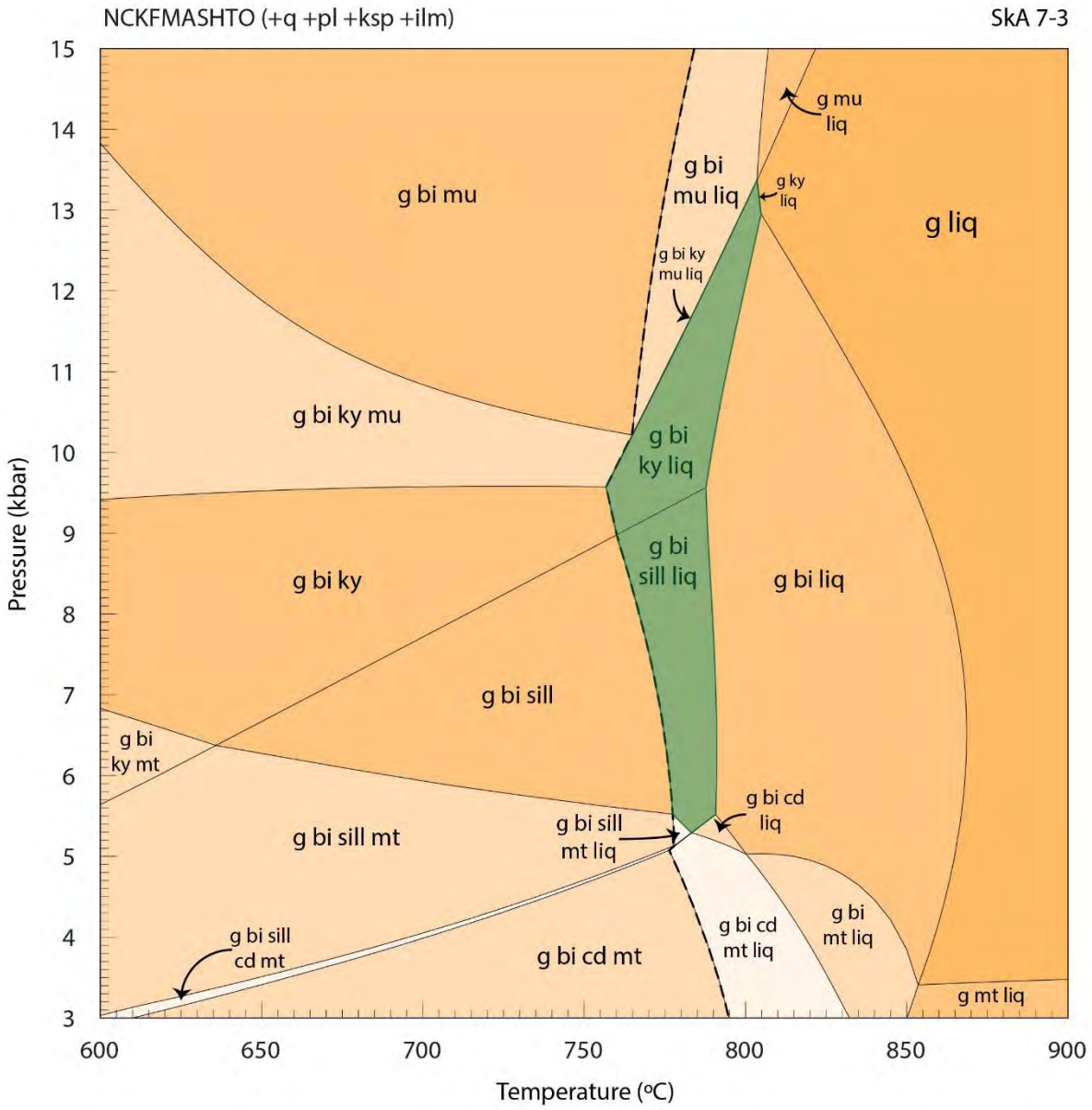

Figure 8.1: Peak-to-retrograde pseudosection modelled for SkA 7-3. Peak conditions are highlighted in green.

8.1.2 Metapelitic sample SkA 7-7

The pseudosection for sample SkA 7-7 has a similar topology to that of sample SkA 7-3, but here the aluminosilicates persist across the entire temperature range at intermediate pressures. Orthopyroxene is stable at high temperatures when subjected to low pressures, and plagioclase is lost at high pressure – high temperature conditions. Garnet and biotite are stable throughout most of the P-T conditions investigated – barring high-temperature, low-pressure conditions. The rock becomes melt-bearing at temperatures above ~750 – 780 ºC throughout the pressure

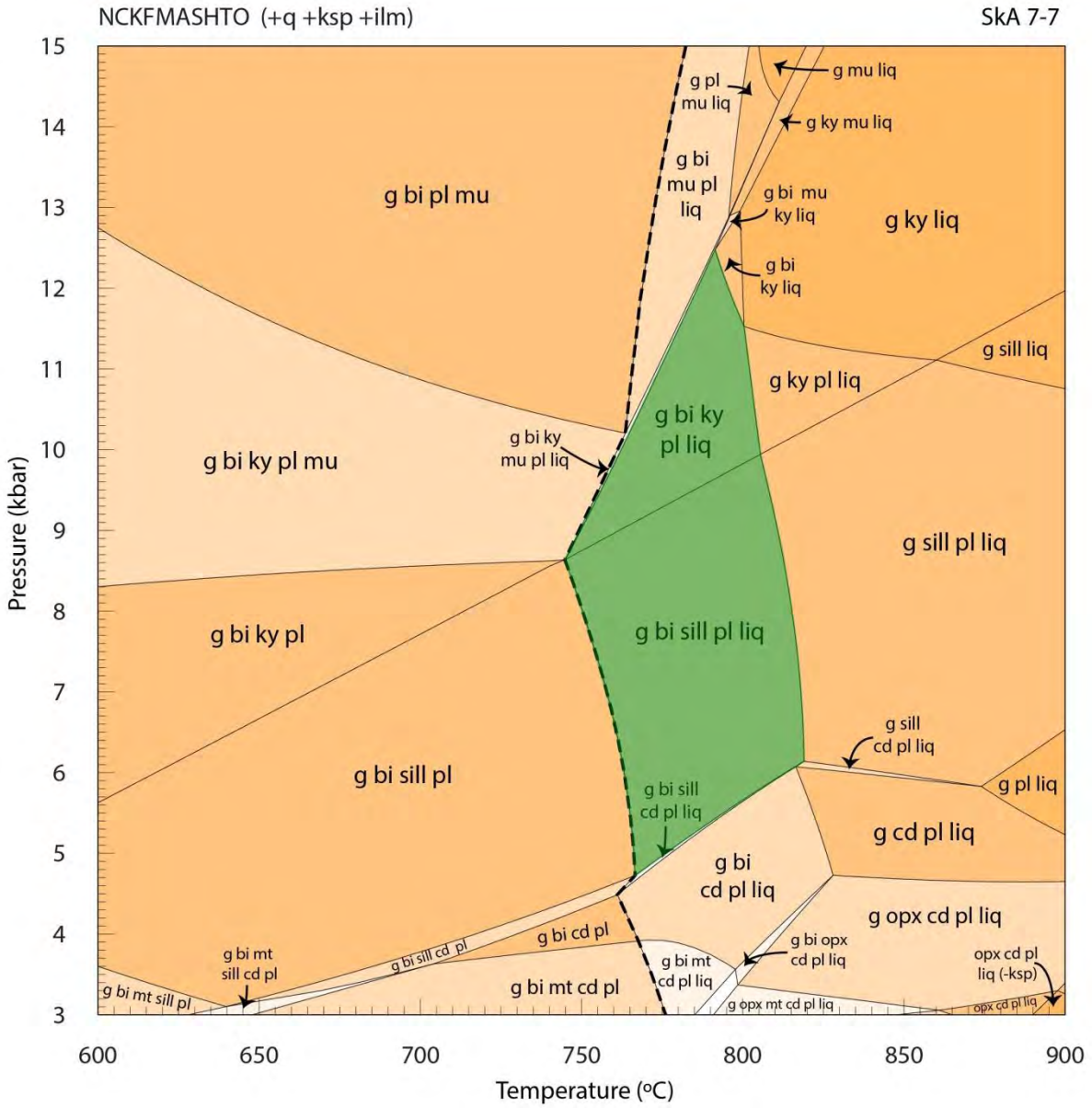

Figure 8.2: Peak-to-retrograde pseudosection modelled for SkA 7-7. Peak conditions are highlighted in green.

range. Kyanite replaces muscovite at intermediate to high pressures above ~750 – 830 ºC. Cordierite and magnetite are present across the temperature range at low pressures. The inferred peak assemblage of garnet-biotite-kyanite/sillimanite-ilmenite-plagioclase-K-feldspar-quartz-melt is stable over a relatively narrow temperature range between 750 and 820 ºC, at pressures between 5 and 12 kbar. The assemblage is bounded by the solidus to lower temperatures, whereas aluminosilicates are removed at higher temperatures and the lower pressure limit of the peak assemblage is constrained by the introduction of cordierite (Fig. 8.2).

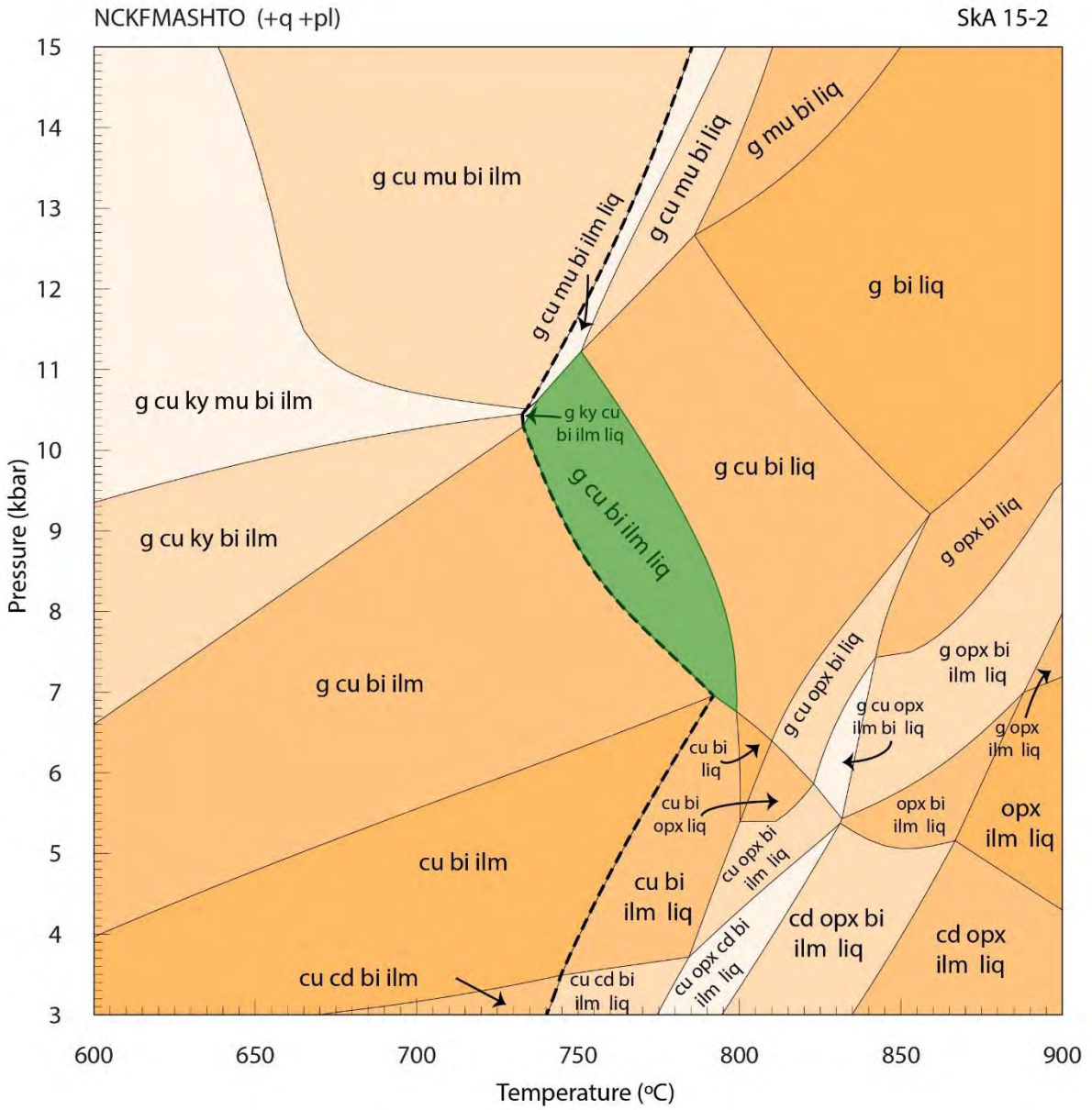

Figure 8.3: Peak-to-retrograde pseudosection modelled for SkA 15-2. Peak conditions are highlighted in green.

8.1.3 Metagraywacke sample SkA 15-2

The pseudosection for sample SkA 15-2 has a markedly different topology to those for samples SkA 7-3 and SkA 7-7, as it is characterised by cummingtonite-bearing fields as well as the absence of aluminosilicates and K-feldspar. Quartz and plagioclase are stable throughout the P-T ranges investigated. The rock becomes melt-bearing at temperatures greater than ~740 – 790 ºC and only has kyanite present at temperatures below ~730 ºC when pressures are greater than 6.6 kbar. Garnet is present at intermediate to high pressures above ~4 – 6.5 kbar, ilmenite is lost at high temperatures and intermediate pressures above ~5.5 kbar, and cummingtonite is

lost at high temperatures greater than ~800 ºC. Orthopyroxene is present at high-temperature, low-pressure conditions, biotite is lost at low pressures above ~835 ºC and cordierite is present at temperatures greater than ~670 ºC when pressures are below ~5 kbar. Muscovite is present at high pressures below ~750 – 850 ºC.

The inferred peak assemblage of garnet-cummingtonite-biotite-ilmenite-plagioclase-quartz-melt is stable over a narrow temperature range between 740 and 800 ºC, at pressures between 7 and 11 kbar. The peak assemblage is bounded by the solidus to lower temperatures and the loss of ilmenite at higher temperatures. The peak assemblage is also constrained by the introduction of muscovite at higher pressures and the loss of garnet at lower pressures (Fig. 8.3).

8.2 Pseudosections modelled for metamafic samples

Metamafic pseudosections and the peak assemblages add useful constraints to assist in modelling the metamorphic history of rocks in question, but once mafic rocks start melting the existing models are not entirely reliable yet. Therefore, mafic pseudosections are more useful at lower P-T conditions and P-T estimates made for high P-T conditions should me made with caution. The mafic rocks in this study were not melted but peak phase fields identified in the Figures 8.4 – 8.5 exist at high P-T conditions and therefore interpretations should be made with caution.

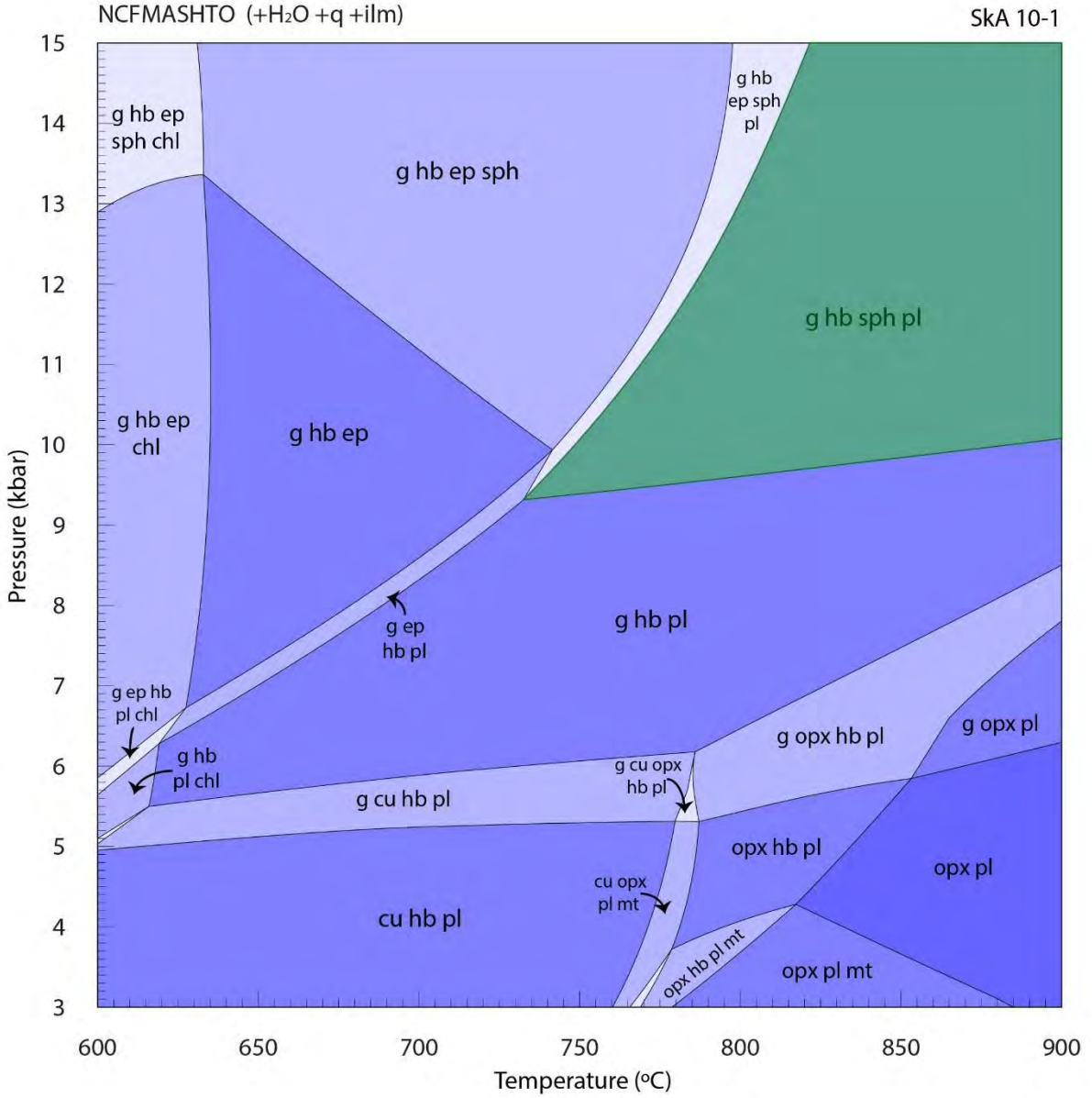

Figure 8.4: Pseudosection modelled for SkA 10-1. Peak conditions are highlighted in green.

8.2.1 Metamafic sample SkA 10-1

The pseudosection modelled for sample SkA 10-1 is characterised by high-variance assemblages that are generally stable over wide P-T ranges. Quartz, ilmenite and fluid (H_2O) are present throughout the P-T ranges investigated. This section is dominated by amphibole-bearing assemblages, with garnet present at intermediate to high pressures above ~5 kbar, chlorite and epidote present at low temperatures and intermediate to high pressures, titanite present at high pressures, and orthopyroxene present at high-temperature – low-pressure conditions. Cummingtonite is only present at temperatures below ~785 ºC and pressures below ~5.6 kbar whereas magnetite is only present at high temperatures where pressures are below ~4 kbar. Hornblende is lost at high temperatures and low pressures and plagioclase is lost at temperatures below ~600 – 790 ºC when pressures are greater than ~6 kbar.

The inferred peak assemblage of garnet-hornblende-ilmenite-plagioclase-quartz-titanite is stable over a wide temperature range at temperatures greater than 750 ºC, at pressures greater than 9 kbar. The peak assemblage is bounded by the introduction of epidote to lower temperatures and the loss of titanite at lower pressures (Fig. 8.4).

8.2.2 Metamafic sample SkB 11-6

The pseudosection modelled for sample SkB 11-6 is characterised by a few high-variance fields at high grades and the presence of hornblende over the P-T range modelled. Garnet is present at high pressures over ~8 – 12 kbar, whereas plagioclase is lost at high pressures where temperatures are below ~700 ºC. Diopside is absent at temperatures and pressures below ~700 ºC and ~10.5 kbar and epidote is present at temperatures below ~750 ºC when at intermediate to high pressures. Titanite is only present at temperatures below ~750 - 770 ºC at pressures below ~12.5 kbar whereas orthopyroxene is present at temperatures greater than 800 ºC at pressures less than 7 kbar.

The inferred peak assemblage of garnet-diopside-hornblende-ilmenite-plagioclase-quartz-±titanite is stable over a wide temperature range at temperatures greater than 700 ºC, and pressures between 8 and 13 kbar. The peak assemblage is bounded by the introduction of epidote to lower temperatures and the loss of titanite at lower pressures (Fig. 8.5).

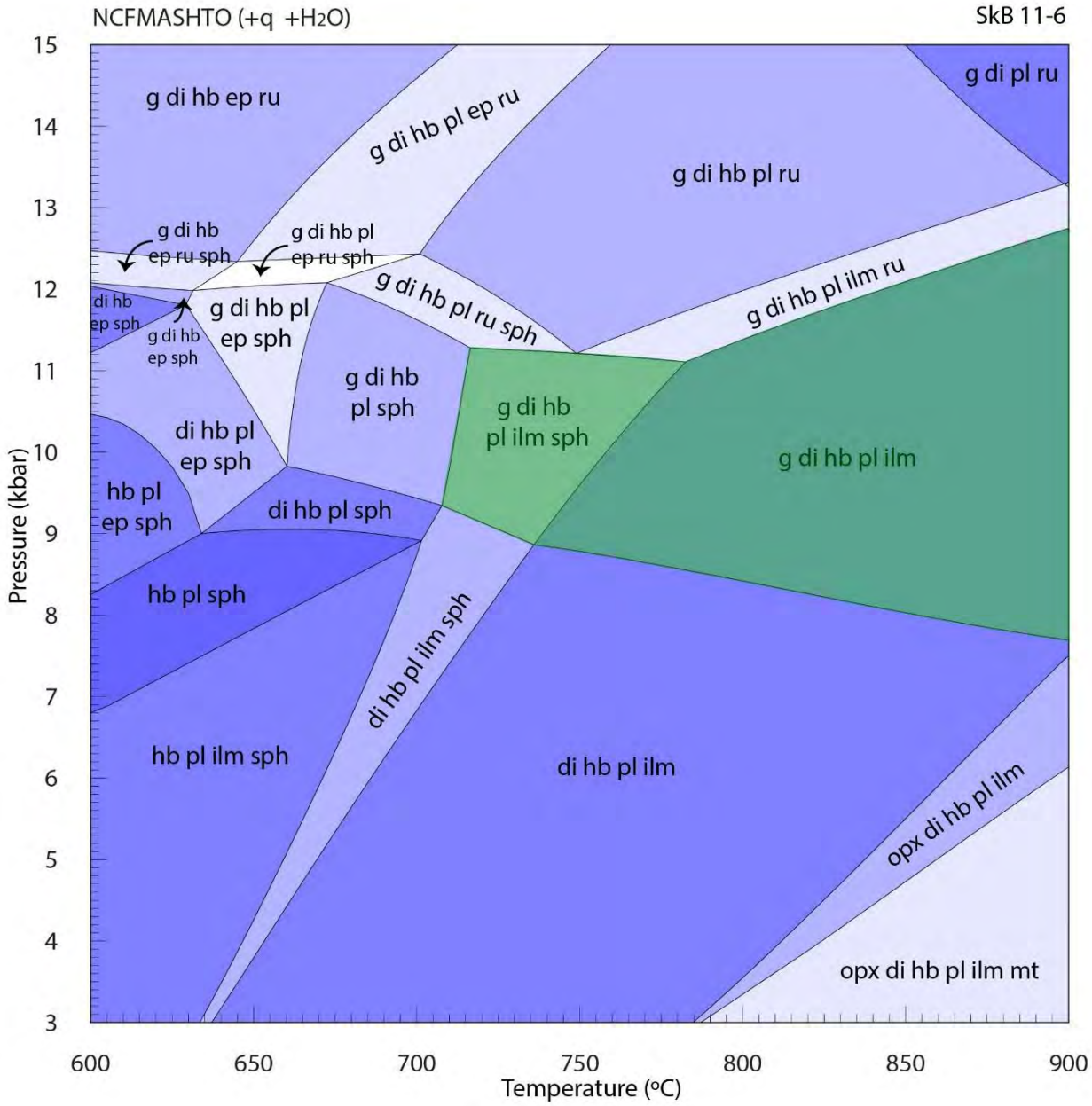

Figure 8.5: Pseudosection modelled for SkB 11-6. Peak conditions are highlighted in green.

8.2.3 Metamafic sample SkA 15-8

The pseudosection for sample SkA 15-8 is characterised by several low variance fields that exist over relatively narrow P-T ranges. Garnet is present at pressures above ~6 kbar and hornblende is present throughout. Diopside is present at intermediate to high temperatures above ~700 ºC and orthopyroxene is only present at high temperatures and low pressures. Plagioclase is lost at intermediate to high pressures where epidote is present at high pressures when temperatures are below ~800 ºC. Titanite is mainly present between ~6 – 13 kbar and ~670 – 885 ºC.

The inferred peak assemblage of garnet-hornblende-plagioclase-quartz-titanite-±ilmenite is stable over a wide temperature range at temperatures between 670 and 810 ºC, at pressures between 6 and 11 kbar. The peak assemblage is bounded by the introduction of diopside to higher temperatures and introduction of epidote to lower temperatures. It is also bound by the loss of plagioclase and titanite to higher and lower pressures, respectively (Fig. 8.4).

The retrograde assemblage containing cummingtonite, ilmenite, plagioclase, hornblende and quartz is present at pressures below ~3 kbar and intermediate temperatures between ~625 – 760 ºC for the bulk composition obtained by XRF. An increase in the abundance of major hornblende-forming elements, i.e. Al, Ca, Mg, Fe and Si increases the stability of the retrograde assemblage to higher pressures (Fig. 8.6). An increase in the proportions of Al, Ca, Mg and Fe by 3 mol. % and Si by 4 mol. % increases the stability of the retrograde assemblage to pressures below ~6 kbar at temperatures below ~750 ºC.

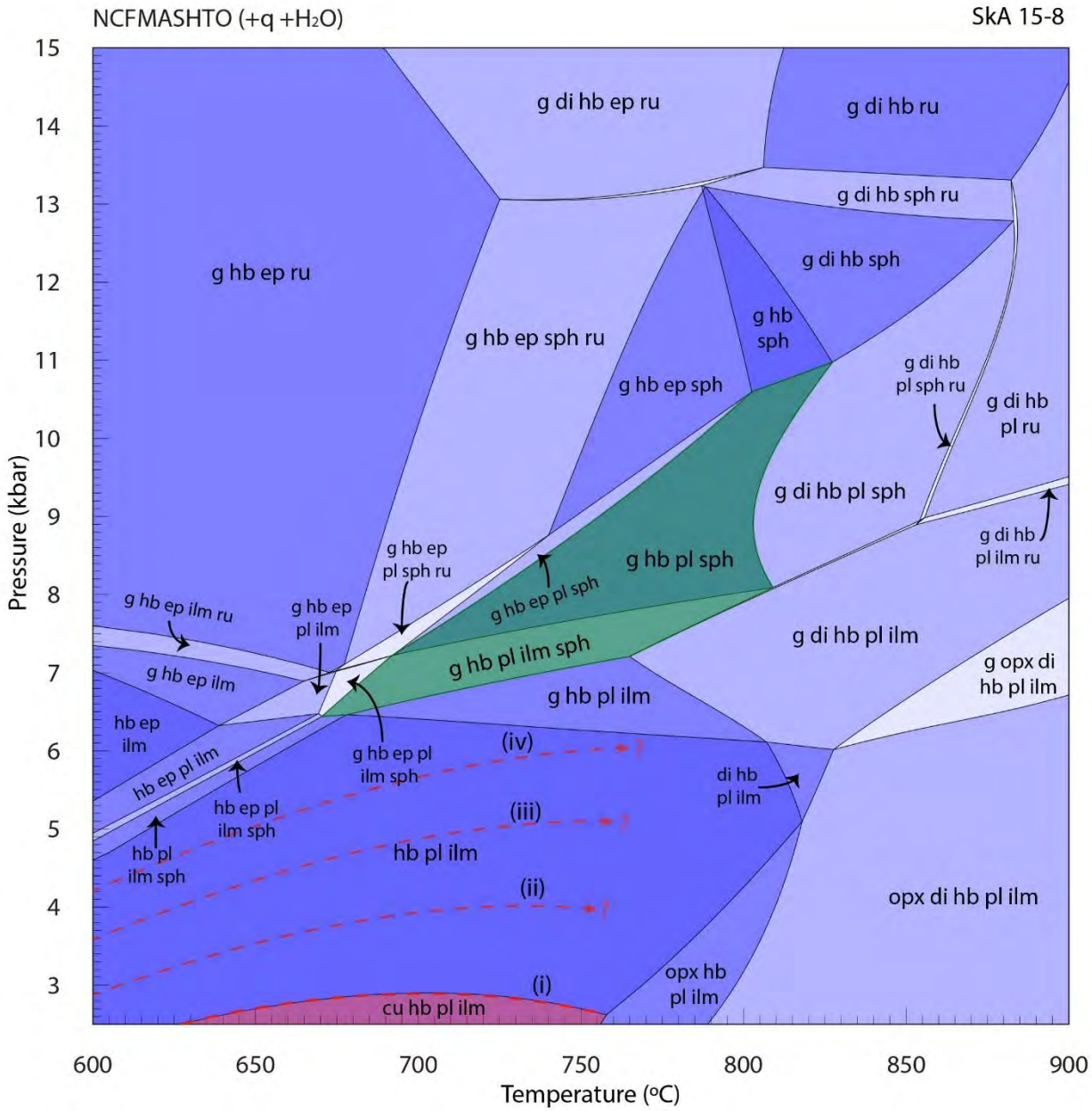

Figure 8.6: Pseudosection modelled for SkA 15-8. Peak conditions are highlighted in green and retrograde conditions in red. The red dashes for (i), (ii), (iii) and (iv) indicate the variable stability of the cu-hb-pl-ilm phase field at varying bulk compositions, where (i) = bulk composition used in XRF and (ii, iii and iv) represent bulk compositions where the mol. percentages of Al, Ca, Mg, Fe and Si were increased incrementally. These oxides were all increased by 1 and 2 mol. % at (ii) and (iii), respectively. For (iv) the Al, Ca, Mg and Fe were increased by 3 mol. % whereas Si was increased by 4 mol. %.

9. Discussion

9.1 Pressure-temperature history of central, Eastern H.U. Sverdrupfjella

The inferred peak equilibrium assemblages derived from textural relationships and mineral chemistries in metapelitic, metagraywacke and metamafic samples from Salknappen in eastern H.U. Sverdrupfjella are characteristic of lower granulite facies metamorphism. To constrain the peak P-T conditions of samples collected from Salknappen, the peak P-T estimates for each sample will be overlapped.

9.1.1 Inferred peak pressure-temperature conditions at Salknappen, Eastern H.U. Sverdrupfjella

Peak metamorphic conditions were estimated by thermodynamic modelling of six representative metapelitic and metamafic rocks from the same area.
Metapelitic and metagraywacke rocks from Salknappen give tight temperature estimates, whereas the inferred peak temperatures from metamafic rocks occurred over a wider temperature range. Metamafic rocks give more precise peak pressure estimates than the metapelitic and metagraywacke rocks. The wide peak pressure range in metapelitic and metagraywacke rocks stems from the uncertainty of the aluminosilicate phase that was present during peak pressures and temperatures. The possibility that either kyanite or sillimanite were present close to peak metamorphic conditions requires the inclusion of both phases in the inferred peak phase fields.

The phase fields of the inferred peak assemblages for metapelitic and metagraywacke rocks overlap over a narrow temperature range and a relatively high pressure range between ~760 ºC – 795 ºC and ~6.9 – 10.2 kbar, respectively. Phase fields of the inferred peak assemblages for metamafic rocks overlap over temperature and pressure ranges between ~770 ºC – 825 ºC and ~9.3 – 10.9 kbar, respectively. The inferred peak P-T conditions for metapelitic / metagraywacke and metamafic rocks overlap over a narrow P-T range between ~770 ºC – 780 ºC and 9.4 – 9.6 kbar (Fig. 9.1).

The overlapping inferred peak P-T estimate is bound by the ilmenite-out univariant from SkA 15-2 at the upper temperature limit but because this univariant is sensitive to bulk composition, the high-temperature limit of the inferred peak P-T estimate is adjusted to the aluminosilicate-out univariant from SkA 7-3. The epidote-out line from SkA 15-8 is a constraint on the upper

pressure limit of the peak P-T estimate, whereas the introduction of melt in SkA 7-3 is a constraint on the low-temperature limit of the peak P-T estimate. The titanite-out univariant from SkA 10-1 is also sensitive to bulk composition and therefore the peak P-T estimate is adjusted to include lower pressures up to the univariant where garnet is lost in SkB 11-6. The adjusted peak P-T estimate is more conservative and expands to 760 – 790 ºC at 8.5 – 10 kbar (Fig. 9.1) and provides a robust estimate of the peak metamorphic conditions experienced by this part of the Maud Belt.

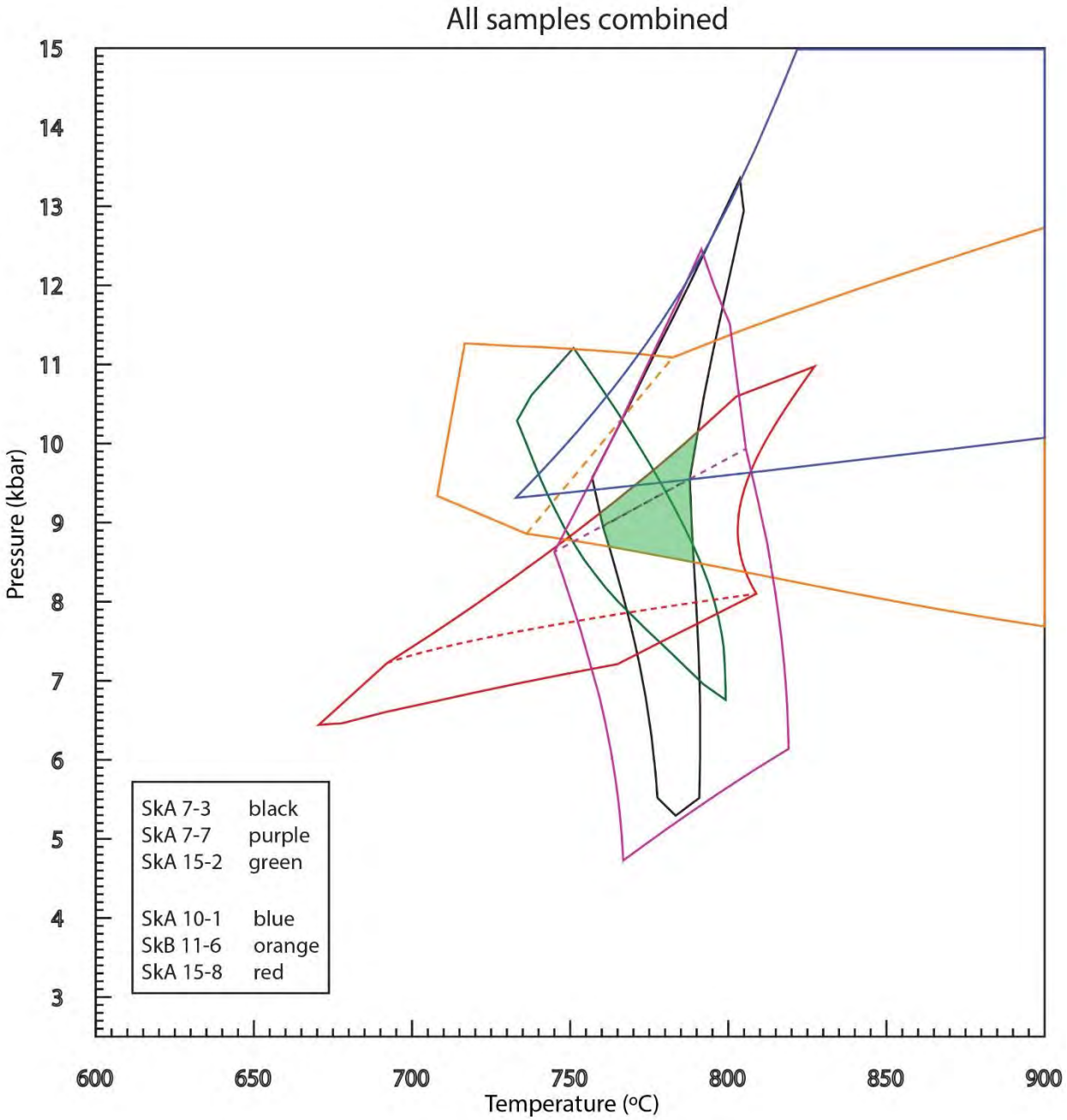

Figure 9.1: Peak P-T conditions (in green, shaded area) experienced by rocks from Salknappen.

The adjusted peak P-T estimate in Figure 9.1 does not lie within the titanite-present phase field from sample SkB 11-6 but titanite is present as inclusions in hornblende-rich domains in the rock itself. The titanite in the rock has most likely resisted complete re-equilibration since the P-T conditions changed and left the phase field where titanite formed part of the mineral assemblage. Thus, titanite is not considered to form a part of the peak assemblage in SkB 11-6. This uncertainty has been accounted for in the peak P-T estimate in Figure 9.1.

9.1.2 Constraints on the pressure-temperature path

The pressure-temperature path will be constrained by looking at the inferred peak metamorphic conditions from Salknappen as well as mineral textures and mineral assemblages that will be compared to the pseudosections modelled for a particular sample. The P-T path will be reconstructed from the late prograde stages of metamorphism, through peak P-T conditions, to the retrograde metamorphic conditions.

The absence of muscovite and presence of leucosomes and K-feldspar in metapelitic rocks from Salknappen means that these rocks likely underwent a muscovite melting reaction during the prograde history, which could have produced K-feldspar, melt, biotite and garnet, e.g. White *et al.* (2001). All melting did not exclusively take place through the breakdown of muscovite but it is highly likely that this reaction took place during the prograde-to-peak metamorphic history. Because all of these minerals are present in the metapelitic and metagraywacke samples, it is reasonable to say that the metapelites produced melt through the breakdown of muscovite during the prograde path. Other melt-producing reactions involve the removal of free H_2O and breakdown of biotite, (e.g. Brown, 2001, White *et al.*, 2004) and likely also contributed to the partial melting process in these rocks. Although it is highly likely that some biotite contributed to forming melt, biotite is still abundant in the metapelitic rocks and therefore the temperatures were not high enough for enough time to break the biotite down completely. In the pseudosection for metapelitic sample SkA 7-7 the breakdown of muscovite in the residuum composition occurs as a narrow field between 750 ºC – 820 ºC at 8.5 – 15 kbar; however, this is an approximation of the position of the muscovite-breakdown reaction because the composition of the prograde rocks is unknown. The addition of water to the system will lower the temperature of the muscovite-breakdown reaction but the gradient of the reaction will stay similar to that in Figure 9.2. Shifting this reaction to a lower temperature does not

change the nature of the prograde-to-peak metamorphic history inferred from the melt residuum bulk compositions in SkA 7-3 and SkA 7-7.

The prograde P-T path is further constrained by the presence of titanite in metamafic sample SkB 11-6. As discussed, the peak P-T estimate for the rocks in Salknappen overlap with a titanite-absent phase field; however, there is titanite present in the rock. The titanite-present phase field lies between 700 ºC – 770 ºC at 9 – 11 kbar, at approximately 50 ºC less than the peak P-T estimate for all the rocks investigated from Salknappen. It is likely that during the prograde history, the rocks passed through this phase field in order to preserve titanite in SkB 11-6 but it is also possible that the prograde path crossed through a relatively narrow, garnet-absent phase field where diopside, hornblende, plagioclase, ilmenite and titanite were present, at temperatures between ~635 ºC – 740 ºC at 3 – 9.5 kbar. Therefore, the titanite does not provide a tight constraint on the pressures and temperatures crossed during the prograde-to-peak path but it does support a clockwise P-T path.

In order to reach the inferred peak P-T conditions after the muscovite-melting reaction the rocks need to follow a short segment of a clockwise P-T path involving heating at high pressure (Fig. 9.2). The aluminosilicate textures in metapelitic sample where sillimanite mats have formed after kyanite further validate a clockwise P-T path, as this transition occurs through a combination of heating and decompression.

The peak-to-retrograde section of the P-T path is derived by taking into consideration the residuum solidus for each of the metapelitic / metagraywacke rocks, the pervasive garnet breakdown microstructures in metamafic rocks, the presence of retrograde cummingtonite in one of the metamafic rocks and the lack of retrograde chlorite in the metamafic samples.

The preservation of peak assemblages in metapelitic / metagraywacke samples SkA 7-3, SkA 7-7 and SkA 15-2 requires the residuum solidus for each rock to be crossed early along the retrograde path, (e.g. White and Powell, 2002, 2010). The residuum solidus phase boundary for each of these rocks is shown in Figure 9.2 and permits the retrograde P-T path to occur over a relatively wide range of pressure and temperature conditions. When used in conjunction with the pervasive garnet breakdown microstructures found in metamafic rocks and garnet-absent phase fields from their respective pseudosections, the retrograde path is characterised by near-isothermal decompression of ~4-6 kbar to retrograde conditions of between ~550 – 750 °C and ~2 – 5 kbar (Fig. 9.2). Significant near-isothermal decompression is also supported by the lack of retrograde chlorite in metamafic sample SkA 15-8 because the retrograde P-T path would

have had to be below 5 kbar at 600 °C to preclude the formation of retrograde chlorite in this rock.

Retrograde cummingtonite described in mafic rocks SkA 10-1 and SkA 15-8 can possibly further constrain the retrograde P-T path by highlighting retrograde conditions. Cummingtonite is stable over a narrower P-T range in sample SkA 15-8 compared to SkA 10-1 and therefore focus will be placed on SkA 15-8. The pseudosection for metamafic sample SkA 15-8 shows that cummingtonite is present at pressures below ~3 kbar and at temperatures between ~600 – 750 °C for condition (i), where it is assumed that cummingtonite is was formed in a volume of equilibration greater than or equal to the size of the sample crushed to obtain a bulk composition which was later used to construct pseudosections.

In SkA 15-8, fine-grained cummingtonite is present in patches throughout the sample in small quantities and grain sizes and is also generally restricted to the margins of hornblende crystals. The effects of changing the bulk composition of the equilibration volume were quantified and are shown in Figure 9.2 in cummingtonite-bearing phase fields marked by (ii), (iii) and (iv). The bulk compositions used to model these changes was approximated to increase the composition to that of hornblende but this was done in a way to stabilise the cummingtonite-bearing assemblage. The actual bulk compositions are impossible to determine and therefore the retrograde conditions are not tightly constrained. The results show that for a reduction in the size of the equilibration volume, i.e. an increase in relative proportions of oxides that constitute a typical hornblende crystal, the size of the retrograde cummingtonite phase field in SkA 15-8 increases. Consequently, a reduction in the size of the equilibration volume means that retrogression could have occurred at higher pressures up to 5 or 6 kbar.

The precise size and composition of the volume of equilibration during the formation of cummingtonite in SkA 15-8 is unknown but due to the fine-grained nature of the incipient cummingtonite and the fact that they are typically restricted to grain boundaries, the interpretation is favoured that they were formed at a volume of equilibration significantly smaller than the size of the bulk composition used to construct the pseudosection. Retrograde conditions are constrained to below the garnet phase boundary from metamafic sample SkA 10-1 and it is therefore likely that the retrograde conditions that formed cummingtonite in SkA 15-8 also occurred below the garnet phase boundary of SkA 10-1. Therefore retrogression probably occurred over a relatively wide pressure-temperature range between ~3 – 4.5 kbar and 550 – 750 °C (Fig. 9.2). A P-T path with some degree of near-isothermal decompression

is favoured by the author because this is typical in orogenic environments, during orogenic collapse; however, the constraints in Figure 9.2 indicate that more cooling could have occurred during exhumation.

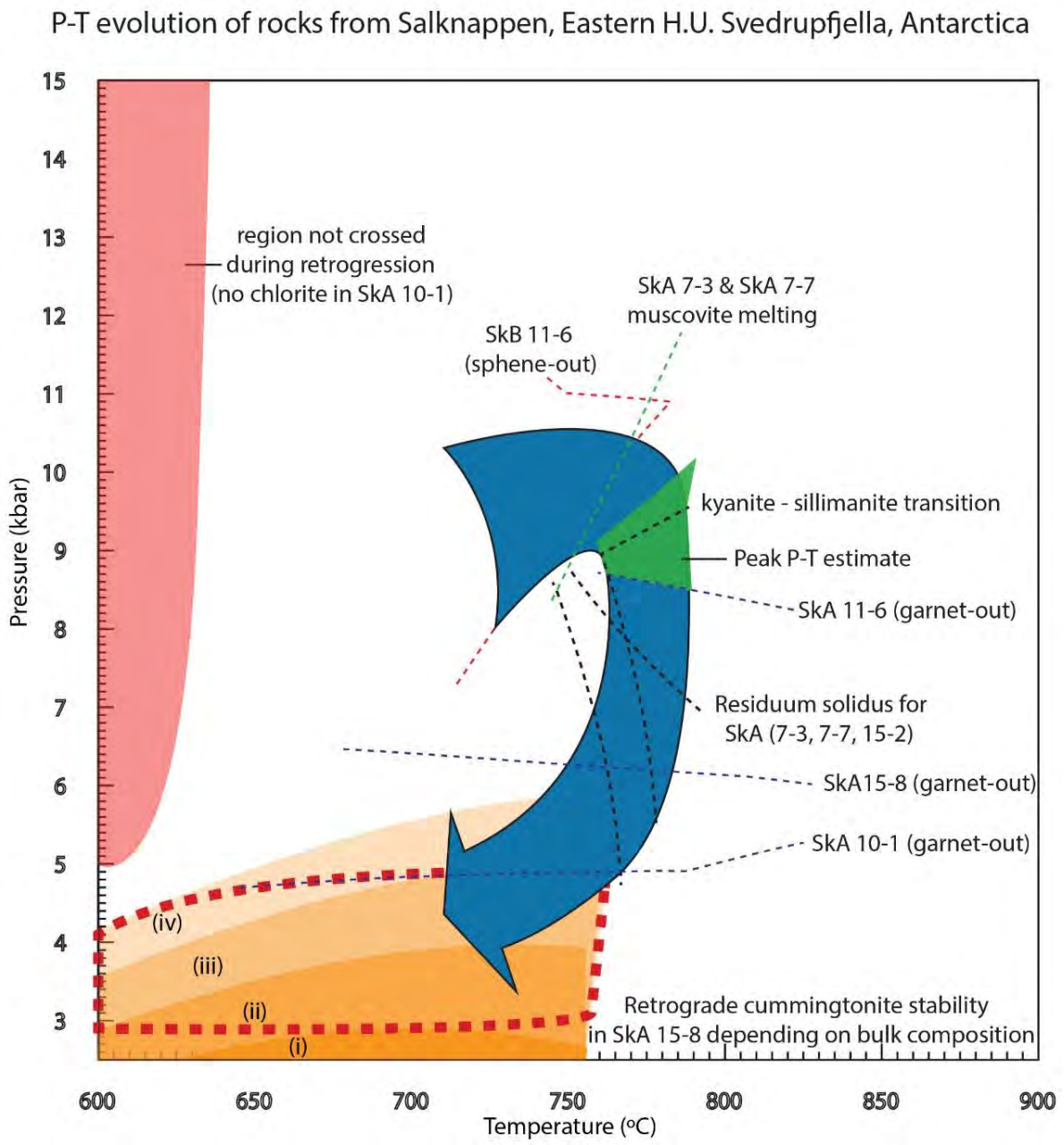

Figure 9.2: Diagram showing the derivation of a possible P-T path for the evolution of the metamorphic rocks from Salknappen, Eastern H.U. Sverdrupfjella. The blue arrow shows the direction and location of possible P-T paths that could have been taken. Red-dashed area indicates the most likely late retrograde conditions. Retrograde cummingtonite phase fields from SkA 15-8: (i), (ii), (iii) and (iv) indicate possible retrogression conditions as a product of varying bulk compositions, as described in Figure 8.6.

9.1.3 Likely timing of metamorphism

Radiometric dating to directly constrain the timing of high-grade metamorphism at Salknappen was not carried out as part of this study but the majority of previous research on granulite facies metamorphism in eastern H.U. Sverdrupfjella point to a Grenvillian age (Moyes and Barton, 1990; Grantham *et al.*, 1995; Groenewald *et al.*, 1995), whereas eclogite facies metamorphism inferred by Board *et al.* (2005) is either Grenvillian or Pan-African. Although Board *et al.* (2005) acknowledge a Grenvillian high-grade metamorphic event, they prefer a model whereby a Pan-African eclogite decompression event extensively overprinted the earlier event. This is possible but the P-T path and peak conditions inferred by Board *et al.* (2005) are at lower temperatures than the peak conditions inferred in this study and by several other studies in H.U. Sverdrupfjella. Their interpretation becomes an issue in reworked high grade metamorphic rocks because dehydration melting reactions from an earlier metamorphic event that occurred at a higher grade than the subsequent one would preclude to formation of overprinting mineral assemblages during the subsequent metamorphic event. The peak metamorphic conditions estimated in this study are not consistent with Board *et al.* (2005) and are consistent with studies that ascribe peak granulite facies metamorphism to the Grenvillian (Grantham *et al.*, 1995; Groenewald *et al.*, 1995; Moyes and Groenewald, 1996). In addition to this, the high grade rocks from Salknappen do not exhibit any evidence for substantial reworking because the structural evidence recorded in this study is for one episode of distributed, penetrative, fabric-forming deformation with localised deformation occurring later on. Therefore this study prefers the interpretation that the granulite facies metamorphism at Salknappen occurred during the Grenvillian.

The pressure-temperature path derived in Figures 9.2 attains peak conditions at lower granulite facies conditions and is retrogressed at low-pressure, amphibolite facies conditions. Combining the prograde and retrograde P-T paths, a coherent clockwise P-T path is derived with approximately 4 to 6 kbar of near-isothermal decompression occurring shortly after peak metamorphism. When this P-T path is compared to P-T paths typical of high-grade orogenic metamorphism (Fig. 9.3), there are striking similarities. The P-T path from this study also follows a clockwise path and exhibits significant near-isothermal decompression to ~5 kbar, where the degree of cooling likely starts to increase significantly. The penetrative fabric in these rocks suggests that there was only one main phase of deformation. Additionally, Pan-African aged Dalmation granites have only accumulated a little strain and can signify that extensive deformation during the Pan-African was not recorded in Salknappen. Thus, the P-T

evolution of Salknappen could easily be attributed to a single orogenic cycle and does not need two metamorphic events to explain the P-T history.

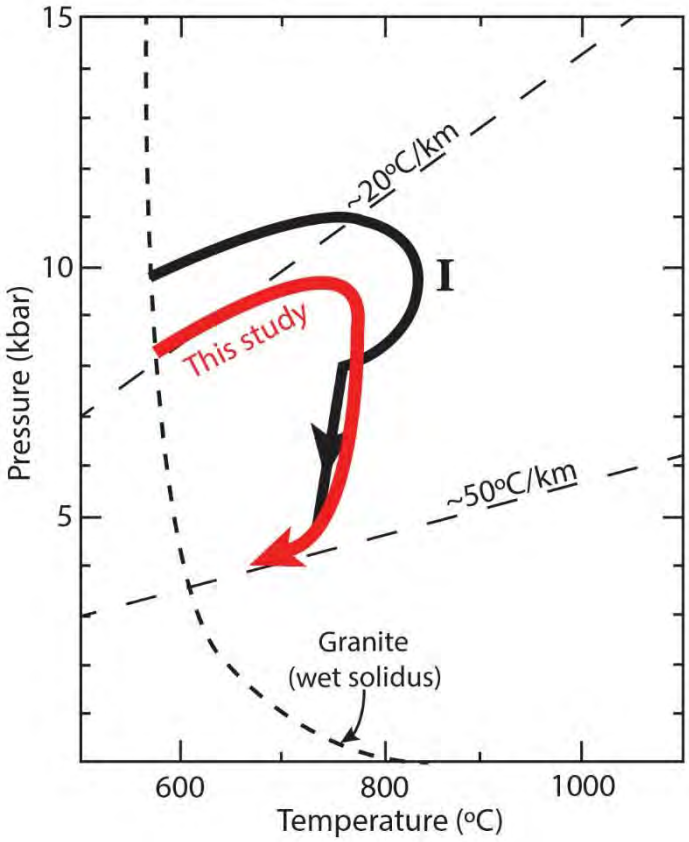

Figure 9.3: Schematic diagram comparing the clockwise P-T path with near-isothermal decompression, from this study with P-T paths characteristic of orogenic environments, where: (I) represents a lower granulite facies, clockwise P-T path with a component of near-isothermal decompression.

An interpretation made by Grantham *et al.* (1995), Groenewald *et al.* (1995), Moyes and Groenewald (1996), McGibbon (2014) and Thomas (2014) incorporates both the Grenvillian and Pan-African into the P-T evolution of H.U. Sverdrupfjella. In this interpretation, they ascribe the peak metamorphic conditions to the Grenvillian event and the retrogression to the Grenvillian or Pan-African. McGibbon (2014) recently identified Pan-African structures as discrete, localised shear zones – none of which were found at Salknappen. Due to the fact that there are no discrete shear zones in Salknappen and the retrograde assemblages are pervasively distributed, it is more likely that retrogression occurred as part of the Grenvillian tectonic cycle.

The retrograde assemblages preserved in these rocks have most likely not formed during the Pan-African because it would require the preservation of a peak Pan-African assemblage that overprints earlier Grenvillian peak assemblages, which we do not see. Nevertheless, it is not

impossible that the retrograde assemblages could have formed during the Pan-African if they have completely overprinted retrograde mineral assemblages formed during the Grenvillian. This is still unlikely because existing zoning profiles and the lack of zoning only suggest that one retrograde event took place.

9.1.4 Comparison of peak pressure-temperature conditions and P-T evolution with previous work done in H.U. Sverdrupfjella

The peak P-T conditions determined from samples collected in this study are generally similar to peak P-T estimates made by Groenewald and Hunter (1991), Grantham *et al.* (1995); Moyes and Groenewald (1996) and Thomas (2014) and are markedly different to those of Board *et al.* (2005). The peak and retrograde P-T estimates for this study and previous work done in H.U. Sverdrupfjella are summarised in Figure 9.4, where all studies envisage clockwise P-T evolution paths.

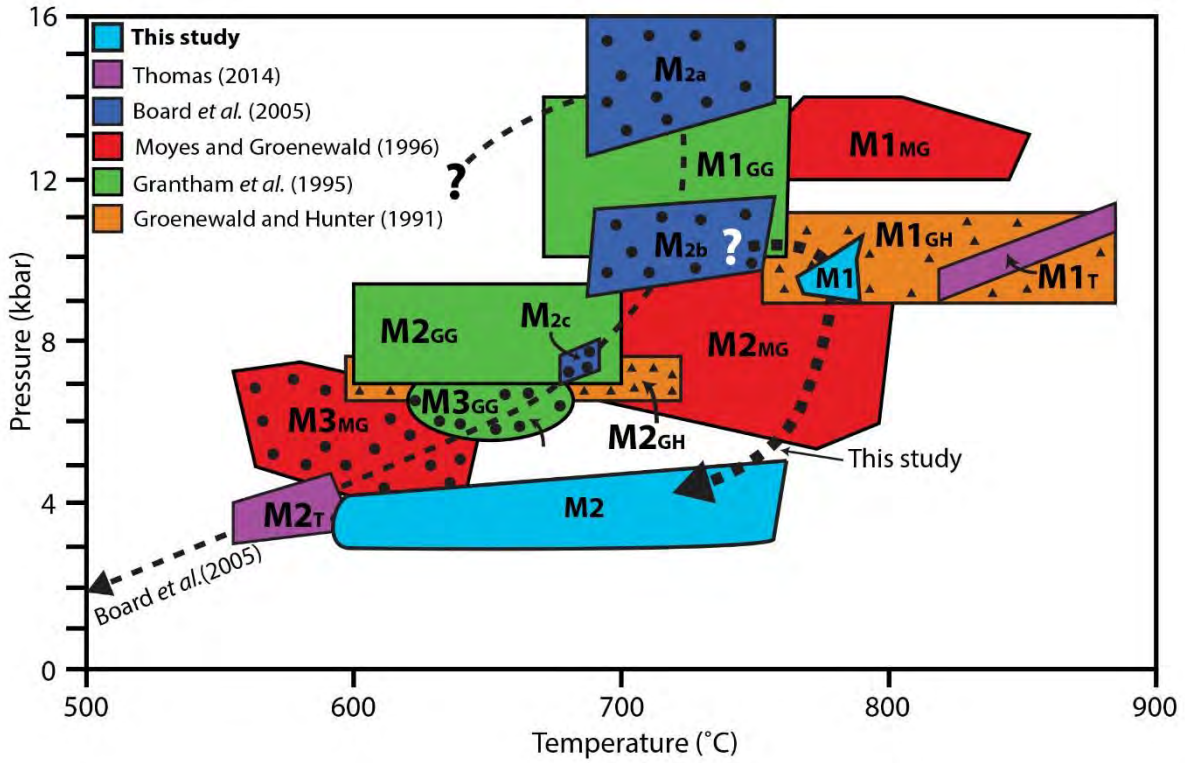

Figure 9.4: Comparison of P-T evolution of Salknappen with previous studies done in H.U. Sverdrupfjella. Metamorphic events that contain black dots are Pan-African in age and events with no texture fill are Grenvillian. P-T estimates that do not differentiate the timing of metamorphism contain black triangles.

Peak metamorphic conditions in this study (M1) overlap with $M1_{GH}$ calculated by Groenewald and Hunter (1991) and the $M2_{MG}$ inferred by Moyes and Groenewald (1996). The peak P-T estimate (M1) from this study almost overlaps with $M1_{GG}$ estimated by Grantham *et al.* (1995), is ~2 kbar below peak pressures summarised in Moyes and Groenewald *et al.* (1996) and is ~20 °C less than the peak estimate made by Thomas (2014). M1 is ~2-3 kbar less and ~10-20 ºC more than the peak P-T estimate (M_{2a}) made by Board *et al.* (2005); however, temperature estimates for M1 are only ~20-30 ºC greater than those made for M_{2b} by Board *et al.* (2005). Groenewald and Hunter (1991) do not differentiate between the ages of peak and retrograde metamorphism but the other studies in Figure 9.5 do. This study has assigned a Grenvillian age to peak metamorphic estimates, which agrees with the timing of peak metamorphism in studies by Grantham *et al.* (1995), Moyes and Groenewald (1996) and Thomas (2014); whereas a study by Board *et al.* (2005) does not reflect a Grenvillian age for peak metamorphism.

The retrograde metamorphic conditions inferred from this study (M2) overlap with Pan-African retrograde events in $M2_T$ (Thomas, 2014) and $M3_{MG}$ (Moyes and Groenewald, 1996), are 2-3 kbar lower than Pan-African retrograde events $M3_{GG}$ and M_{2c} (Grantham *et al.*, 1995; Board *et al.*, 2005) and are ~2 kbar lower than the retrograde event $M2_{GH}$ (Groenewald and Hunter, 1991).

9.1.4.1 Likely causes of peak P-T estimate variations between studies

Differences between the peak estimates constrained here and those from other studies can be attributed to the different sampling localities used for each study but we would expect them to preserve roughly the same apparent geotherm if they were formed in the same orogenic environment. Therefore, differences in peak estimates are most likely due to the different thermobarometry methods used to infer P-T conditions. The older studies, i.e. those of Groenewald and Hunter (1991), Grantham *et al.* (1995), Moyes and Groenewald (1996) and Board *et al.* (2005) largely relied on conventional and optimal thermobarometry to estimate their peak and retrograde P-T conditions, whereas Thomas (2014) and this study modelled the metamorphic conditions using pseudosections calculated from updated activity-composition models and recent versions of THERMOCALC. Conventional and optimal thermobarometry relies on the mineral compositions to infer peak metamorphic conditions but in granulite facies rocks with long retrograde histories there is quite a large uncertainty as to what the composition of the minerals were during peak metamorphism. Pseudosection modelling does not require

mineral compositions to estimate peak P-T conditions and uses bulk rock compositions to model likely mineral assemblages present over a P-T range (Kelsey, 2008). Thus, the P-T estimates made by Thomas (2014) will be considered as more reliable than the studies that made used of conventional and optimal thermobarometry.

The preservation of these compositions in rocks from the study region is problematic because high-grade rocks have a long retrograde history which permits more time for retrogression and the diffusion of elements to occur (Harley *et al.*, 1992). Thus, optimal thermobarometry done on rocks from H.U. Sverdrupfjella could more accurately elucidate retrograde conditions than peak P-T conditions because peak compositions could easily be affected during retrogression. More robust minerals such as garnet that preserve evidence of retrograde zoning likely have core compositions representative of peak conditions but other minerals commonly used in association with garnet in conventional thermobarometry estimates, e.g. biotite and plagioclase are not as robust and can easily be re-equilibrated during retrogression and lose the composition representative of peak metamorphism (e.g. Cross, 2013). Additional uncertainties in conventional and optimal thermobarometry stem from possibly underestimated uncertainties assigned to P-T estimates and the fact that the significant extrapolations have been made from experimental data to infer end-member compositions of minerals in high-grade metamorphic rocks (Powell and Holland, 2008).

The use of different thermobarometers in other studies and the use of pseudosection modelling in this study is most likely the cause of the variation between P-T estimates (especially peak estimates) from this study and those that have relied largely on thermobarometry to estimate the P-T history. Significant differences between the timing and peak P-T conditions between Board *et al.* (2005) and this study could occur if Board *et al.* (2005) collected samples used to estimate P-T conditions from a major, localised deformation zone that was reworked during the Pan-African.

The slight discrepancy between this study and Thomas (2014) is less intuitive because both studies have used phase diagram modelling and pseudosections to estimate their metamorphic conditions. This study uses more recent activity-composition models from White *et al.* (2014) and unpublished data from Diener and Powell (2012) to calculate phase boundaries in pseudosections, and Thomas (2014) used activity-composition models from several older

sources. The adjustments made in White *et al.* (2014) had more of an impact on pseudosections created for subsolidus metapelites than suprasolidus rocks such as those dealt with in this study.

The study conducted by Thomas (2014) was done at the southern section of Eastern H.U. Sverdrupfjella – ~40 km away from where the samples were collected for this study. This horizontal distance could translate to a difference of several kilometres depth between the central and southern domains of Eastern H.U. Sverdrupfjella, assuming that the Maud Belt was not exhumed at the same level throughout. Assuming an average rock density of ~3000 $kg.m^{-3}$, a variation of 1 km in depth translates to ~0.3 kbar. Assuming the vertical distance between the central and southern domains of H.U. Sverdrupfjella was 5-10 km, there could be discrepancy of 1.5-3 kbar and 20-100 °C, assuming geothermal gradients of between 2-10 °C/km at depths in the crust where peak metamorphism occurred. Within the uncertainty of peak phase fields from this study and Thomas (2014), it is possible to have a difference of ~2 kbar between the peak P-T estimates in each study. The estimates in both studies are similar enough to suggest that the region between Salknappen and Nupskåpa is intact without major faults in between. The slight discrepancy in peak pressures could be due to slight tilting of the crustal block or differential exhumation between the two localities.

9.1.4.2 Likely causes of retrograde P-T estimate variations between studies

The largest uncertainty with the retrograde P-T estimate is the size and composition of the volume of equilibration that formed cummingtonite in mafic rocks during retrogression. Varying the composition had significant effects on the pressure stability of the retrograde assemblage and it is likely that the equilibrium assemblage could be stabilised to slightly higher pressures. A bias towards higher pressure would be more in agreement with studies made by Groenewald and Hunter (1991), Grantham *et al.* (1995) and Board *et al.* (2005). Although retrogression occurred well below peak metamorphic conditions, they still took place under low-pressure amphibolite facies conditions. Again, the time taken to exhume the rocks after retrogression had occurred at upper medium grade conditions could impact the final composition preserved in the minerals if the time was sufficient enough for a significant amount of subsolidus re-equilibration to occur. For example, biotite was unzoned in the rocks sampled for this study, whereas garnets were usually zoned and uncommonly plagioclase and hornblende were zoned. The zoning preserved in these rocks is entirely attributed to retrogression but in minerals that are unzoned it is possible that they have completely re-

equilibrated during the retrograde history. Therefore this also creates significant uncertainty with using thermobarometry to estimate P-T conditions – even in inferred retrograde assemblages and compositions. Despite the large uncertainty associated with the retrograde temperature range in this study, it overlaps with retrograde estimates made by Thomas (2014) based on mineral assemblage stability.

Shear zones noted by Board (2001) and studied by McGibbon (2014) in SE H.U. Sverdrupfjella and Northern Kirvanweggen, respectively were not seen in this study area. It is uncertain whether or not they are present in NE H.U. Sverdrupfjella but these shear zones might have been sampled in previous studies and record Pan-African deformation and metamorphism not seen in this study.

In conclusion, the peak P-T conditions estimated in this study are broadly similar and consistent with those of previous workers, but constrain the peak conditions to a significantly narrower P-T range than previous studies in central, Eastern H.U. Sverdrupfjella. Therefore, this work provides a robust revision of the metamorphism of central Sverdrupfjella, and confirms that Grenvillian metamorphism occurred along a clockwise P-T path, with peak metamorphic conditions of 760 – 790 ºC at 8.5 – 10 kbar, followed by near-isothermal decompression of ~4-6 kbar to retrograde conditions between ~550 – 750 °C and ~2 – 5 kbar.

9.2 Structural and deformation history at Salknappen, H.U. Sverdrupfjella

Relative age relationships of the different lithologies and deformation zones in addition to deformation mechanisms inferred from microstructures will be used to piece together a deformation history to construct a tectono-metamorphic history for the area.

9.2.1 Relative age relationships and kinematics

Concordant and discordant megacrystic leucogranite dykes cross-cut garnet-biotite-feldspar gneisses, metamafic bodies and leucosome-rich migmatites and are, in turn, cross-cut by the Dalmatian granites. Therefore, the oldest lithologies in the area are the garnet-biotite-feldspar gneisses, mafic bodies and leucosome-rich migmatites. The Dalmatian granites intruded at *c.* 470 Ma (Grantham *et al.*, 1991), thus the megacrystic leucogranite dykes, garnet-biotite-feldspar gneisses, mafic bodies and leucosome-rich migmatites must be older than *c.* 470 Ma.

North-south striking foliations, south-east plunging mineral lineations and top-to-NW shear sense indicators in the garnet-biotite-feldspar gneisses indicate that the gneisses were deformed by NW-directed thrusting which could be as a result of NW – SE greatest compression. It is assumed that the foliations and lineations were formed during the same tectonic event and that the rocks have undergone rigid block rotation after fabric formation so that the lineations are no longer down-dip. The peak mineral assemblages in the metapelitic and metagraywacke gneisses are fabric-defining minerals. Thus, the garnet-biotite-feldspar gneisses formed in response to NW-directed thrusting due to the greatest principal stress being oriented NW – SE.

Leucosomes and leucosome-rich migmatites are oriented subparallel to the gneissic foliation formed by subvertical shortening, therefore melting occurred at the same time as the top-to-NW shearing. In order for the metamafic bodies to be oriented subparallel to the gneissic foliation they must have been deposited or emplaced prior to or concurrently with the top-to-NW shearing.

Concordant and discordant megacrystic leucogranite dykes in the area do not displace any of the surrounding lithologies and most likely formed as a through temporary embrittlement under high melt pressures and low differential stresses in the mid crust, (e.g. Thomas, 2014). Shear zones 1 and 2 are small and most likely formed to accommodate strain locally.

The intrusion of the Dalmation granites at *c.* 470 Ma occurred concurrently with a small component of normal shear, represented by shear zone 3. This means that at the time the Dalmation granite intruded into shear zone 3, the shear zone was weaker than the pre-existing gneissic foliation. They shallow intrusion angles of the Dalmation granites requires a relatively low overburden or a substantial melt pressure. Shear zone 3 appears to be brittle-ductile, which could mean that the Dalmation granites intruded into the country rock close to the brittle-ductile transition zone.

9.2.2 Deformation mechanisms in microstructures

The mineral assemblages in rocks from Salknappen have evolved during the prograde history and have been overprinted by retrograde mineral assemblages, which means that the microstructures preserved in the lithologies from Salknappen only reflect peak-to-retrograde conditions. The overall abundance of curved, lobate quartz grain boundaries in the garnet-biotite-feldspar gneisses within non-leucosome domains indicates that recovery and recrystallisation largely occurred by grain boundary migration through dislocation creep. This

is to be expected in these rocks because grain boundary migration occurs at high temperature conditions in natural, relatively coarse-grained rocks (Stipp *et al.*, 2002b).

Leucosomes are subparallel to matrix minerals and the gneissic foliation which means that leucosomes formed after or whereas foliation was being developed and most likely formed during the peak metamorphism. The leucosomes in garnet-biotite-feldspar gneisses and leucosome-rich migmatites indicate that a melt phase was present and means that whereas the rocks were melt-bearing, the rocks were most likely deformed by diffusion creep (Paterson, 2001). Quartz crystals in leucosomes are not euhedral which means that they were deformed after the melt was crystallised, during retrogression.

Leucosomes from the leucosome-rich migmatites predominantly have curved, lobate quartz grain boundaries which means that at some time after the leucosome crystallised grain boundary migration through dislocation creep occurred. This could have happened if deformation outlasted peak metamorphism or it could indicate that retrogression occurred between ~550 – 700 ºC (Stipp *et al.*, 2002). Considering the retrogression conditions identified from phase diagram modelling, it is most likely due to the latter. Leucosomes in the garnet-biotite-feldspar gneiss, leucosome-rich migmatites and leucosomes that intruded into metamafic lenses from the surrounding gneisses also exhibit less pervasive evidence of subgrain rotation and bulging in quartz which means that small amounts of dynamic recrystallisation occurred during the retrograde history at ~400 ºC (Stipp *et al.*, 2002) through dislocation creep. Retrogression occurred at Salknappen at temperatures between ~600 – 750 °C, therefore the minor amounts of bulging and subgrain rotation in quartz do not reflect any significant retrograde deformation event.

An investigation to determine the effects that more competent mafic rocks have on the deformation mechanisms and flow stresses in less competent surrounding rocks has found that within ~70 cm from a ~20 m long mafic lens, dynamically recrystallised quartz grains are similar in size (180 – 200 μm) and flow stresses are equally low (~1 MPa). Therefore the presence of a ~20 m long mafic lens has no observable effect on the dynamically recrystallised grain sizes of quartz within a metre of the lens. This effect might be more noticeable if samples were collected further away from the mafic lens.

9.3 Tectono-metamorphic history of central, Eastern H.U. Sverdrupfjella

Table 9.1: Timing and sequence of events at Salknappen, Eastern H.U. Sverdrupfjella

Metamorphism / dated intrusions (inferred ages) and [depths]	Relative age relationships and faulting	Quartz microstructures
M1 (Grenvillian) [28 – 34 km]*	Gneiss and leucosome-rich migmatite formation	
	Normal shear zones 1 & 2	
M2 (Grenvillian) [10 – 15 km]*		Grain boundary migration in leucosomes from leucosome-rich migmatites formed during M1
	Megacrystic leucogranite dykes form from melting deeper in the crust in response to Pan-African collision	
c.* 470 Ma [10 – 20 km]*	Normal shear zone 3 and intrusion of the Dalmation granites	

***Depths calculated assume an average crustal density of 3000 kg.m^{-3}**

****Depth calculated from estimated emplacement depth of 6 kbar (Grantham *et al.*, 1991)**

Table 9.1 combines the metamorphic and structural observations, relative age relationships and inferred timing of observations into a sequence of events that make up the geological history at Salknappen, Eastern H.U. Sverdrupfjella. The geological history at Salknappen represents a coherent geological history which starts at peak metamorphism in the mid to lower crust during the Grenvillian and is followed by a period of exhumation prior to the subtle reworking of these rocks during the Grenvillian in the mid crust, and is finally reflected by the continued exhumation following the Pan-African collision.

9.4 Implications for the reworking of granulites

The formation of granulites in an orogenic environment is characterised by the partial melting, melt loss from the protolith and subsequent elevation of the residuum solidus to produce more refractory, volatile-poor rocks. When pressures and temperatures drop to the conditions where melt-producing reactions form melt, the lack of volatiles as a result of melt loss precludes a reversal of the melt-forming reaction to form hydrous minerals and complete retrogression of the peak mineral assemblages.

Similarly, once refractory granulites are formed and they are subjected to another metamorphic event where P-T conditions less than those where the last melt was formed, the later metamorphic event will not pervasively rework the structures and granulites facies mineral assemblages, unless the later event is accompanied by pervasive deformation and fluid influx (Tenczer *et al.*, 2006; Diener *et al.*, 2008). This study presents a case where the granulites formed during the Grenvillian orogenic cycle are still preserved and did not develop or preserve any imprint of the Pan-African conditions they were subjected to. The peak temperature conditions of ~780 °C reached during the Grenvillian orogeny is therefore assumed to have been higher than the peak temperature conditions reached during the Pan-African in central H.U. Sverdrupfjella.

Deformation during the Pan-African was not pervasive and was localised because the fabric formed during the Grenvillian was in the right orientation to be reactivated and reworked over narrow zones (e.g. McGibbon, 2014). Fluid infiltration also plays a major role in retrogressing granulite facies assemblages but a fluid source is necessary. A significant amount of volatiles could potentially be released into the orogenic system if juvenile, volatile-rich metasediments underplated the granulites but there is no sign of thick, juvenile supracrustal sequences in close proximity to central H.U. Sverdrupfjella. Thus, this study also presents a case where mid-crustal reworking was inhibited due to the lack of sufficient rehydration.

Several generations of metamorphic events can easily be masked as a result of earlier or later events. When dealing with granulites that have a lengthy retrograde path caution must be taken with thermobarometry methods that rely on mineral compositions. Pseudosections do not rely on mineral compositions and are thus a more robust method of estimating peak conditions in granulites.

10. Conclusions

A combination of structural and metamorphic data collected from Salknappen, Eastern H.U. Sverdrupfjella, Antarctica provides insight into the geological history of central H.U. Sverdrupfjella. Macroscopic and microscopic structures in the garnet-biotite-feldspar gneisses indicate that pervasive deformation from only one tectonic event is preserved at Salknappen. Quartz microstructures in the matrix of garnet-biotite-feldspar gneisses were not recrystallised differently in response to possible differential deformation within a metre of a large competent lens; however, quartz microstructures in leucosomes were recrystallised during the non-pervasive retrogression. The formation of the gneisses and intrusion of leucogranite dykes are older than *c.* 470 Ma, which is constrained by the intrusion of the Dalmation granites.

A combination of metamafic and metapelitic samples collected from granulites at Salknappen have peak assemblages that reflect robust peak metamorphic estimates of 760 – 790 ºC at 8.5 – 10 kbar and retrograde metamorphic conditions of between ~550 – 750 °C and ~2 – 5 kbar. These are similar to peak P-T estimates made by Thomas (2014) in southern H.U. Sverdrupfjella, are consistent with previous studies made in the region (Groenewald and Hunter, 1991; Grantham *et al.*, 1995; Moyes and Groenewald, 1996) and are markedly different to estimates made by Board *et al.* (2005).

The geological history at Salknappen is characterised by one main orogenic cycle that took place during the Grenvillian. Granulite facies peak metamorphism was followed by a period of near-isothermal decompression and retrogression along a clockwise P-T path. The series of megacrystic leucogranites most likely intruded into the country rock during the Pan-African as melt migrated from deeper levels in the crust. Finally, the gneisses and leucogranites were intruded by the Dalmation granites at *c.* 470 Ma at the brittle-ductile transition.

This study presents a case where the effects of mid-crustal reworking by a high-grade metamorphic event are not shown due to the lack of rehydration, pervasive deformation and an elevated residuum solidus as a result of higher peak temperatures in an earlier granulite facies metamorphic event. Caution must be taken when investigating polymetamorphic environments that have been subjected to more than one granulite facies event, because if earlier metamorphic conditions exceed the P-T conditions of a later event it is likely that the subsequent event will not rework and overprint the earlier event, unless it is coupled with significant and pervasive deformation and the influx of fluids. Similarly, if a late granulite facies metamorphic event occurs at higher pressures and temperatures than all earlier events, the later event can modify

mineral assemblages and destroy evidence of earlier metamorphism. When trying to piece together a metamorphic history for granulites it is crucial to choose a suitable P-T estimation technique. Conventional and optimal thermobarometry methods rely on mineral compositions, which can easily be obscured and altered during the long retrograde history in a granulites; however, pseudosection modelling does not rely on mineral compositions and as seen in this study, can provide more robust and precise peak P-T estimates in granulites.

References

Anderson, E. M., 1951. The dynamics of faulting and dyke formation with applications to Britain. *Oliver & Boyd, Edinburgh. 2nd edition,* 206 pp.

Arndt, N. T., Todt, W., Chauvel, M., Tapfer, M. & Weber, K., 1991. U-Pb zircon age and Nd isotopic composition of granitoids, charnockites and supracrustal rocks from Heimefrontfjella, Antarctica. *Geologische Rundschau,* **80,** 759-777.

Aucamp, A. P. H, Wolmerans, G. & Neethling, D. C., 1972. The Urfjell Group, a deformed (?) early Palaeozoic sedimentary sequence, Kirwanveggen, western Dronning Maud Land. In: Adie, R. J. (ed.) *Antarctic Geology and Geophysics, Universitetsforlaget, Oslo*. 557-562

Barton, J. M. Klemd, R., Allsopp, H. L., Auret, S. H. & Copperthwaite, Y. E., 1987. The geology and geochronology of the Annandagstopanne granite, Western Dronning Maud Land, Antarctica. *Contributions to Mineralogy and Petrology*, **97,** 488-496.

Basson, I. J., Perrit, S., Watkeys, M. K. & Menzies, A. H., 2004. Geochemical correlation between metasediments of the Mfongosi Group of the Natal Sector of the Namaqua-Natal Metamorphic Province, South Africa and the Ahlmannryggen Group of the Grunehogna Province, Antarctica. *Gondwana Research*, **7,** 5-73.

Bhowmik, S. K., Sarbadhikari, A. B., Spiering, B. & Raith, M. M., 2005. Mesoproterozoic reworking of Palaeoproterozoic ultrahigh-temperature granulites in the Central Indian Tectonic Zone and its implications. *Journal of Petrology*, **46,** 1085-1119.

Bisnath, A., Frimmel, H. E., Armstrong, R. A. & Board, W. S., 2006. Tectono-thermal evolution of the Maud Belt: New SHRIMP U-Pb data from Gjelsviksfjella, Dronning Maud Land, East Antarctica. *Precambrian Research*, **150,** 95-121.

Board, W. S., 2001. *Tectonothermal evolution of the southern H. U. Sverdrupfjella, western Dronning Maud Land, Antarctica*. Ph.D. thesis, University of Cape Town, 205 pp.

Board, W. S., Frimmel, H. E. & Armstrong, R. A., 2005. Pan-African tectonism in the Western Maud Belt: P-T-t path for high-grade gneisses in H.U. Sverdrupfjella, East Antarctica. *Journal of Petrology*, **46,** 671-699.

Brown, M., 2001. Orogeny, migmatites and leucogranites: A review. *Journal of Earth System Science*, **110:4,** 313-336.

Brown, M., 2002. Retrograde processes in migmatites and granulites revisited. *Journal of Metamorphic Geology*, **20,** 25-40.

Brown, M. & Raith, M., 1996. First evidence of ultrahigh-temperature decompression from the granulite province of southern India. *Journal of the Geological Society, London,* **153,** 819-822.

Brown, M. & Solar, G. S., 1998a. Shear-zone systems and melts: feedback relations and self-organization in orogenic belts. *Journal of Structural Geology*, **20,** 211-227.

Brown, M. & Solar, G. S., 1998b. Granite ascent and emplacement during contractional deformation in convergent orogens. *Journal of Structural Geology*, **20,** 1365-1393.

Connolly, J. A. D., 1997. Devolatilization-generated fluid pressure and deformation-propagated fluid flow during prograde regional metamorphism. *Journal of Geophysical Research*, **102,** 149-173.

Cross, C., 2013. *The Metamorphic Evolution of an Ancient Accretionary Prism in the Southern Zone of the Damara Belt in Namibia*. Unpublished M.Sc. thesis. University of Cape Town, Cape Town, pp. 105

Curtis, M. L. & Riley, T. R., 2003. Mobilization of fluidized sediment during sill emplacement, western Dronning Maud Land, East Antarctica. *Antarctic Science,* **15,** 393-398.

Dalziel, I. W. D., 1992. Antarctica; a tale of two supercontinents? *Annual Review of Earth and Planetary Sciences*, **20,** 501-526.

Dasgupta, S., Sengupta, S., Bose, S., Fukuoka, M. & Dasgupta, S., 2001. Polymetamorphism in the Schirmacher Hills Granulites, East Antarctica: Implications for Tectonothermal Reworking of an Isobarically Cooled Deep Continental Crust. *Gondwana Research*, **4:3,** 337-357.

Davidson, C., Schmid, S. M. & Hollister, L. S., 1994. Role of melt during deformation in the deep crust. *Terra Nova*, **6,** 133-142.

Dewey, J. F., 1988. Extensional collapse of orogens. *Tectonics,* **7,** 1123-1139.

Diener, J. F. A. & Powell, R., 2012. Unpublished updates of activity-composition models compatible with the Holland and Powell, 2011 dataset.

Diener, J. F. A., White, R. W. & Powell, R., 2008. Granulite facies metamorphism and subsolidus fluid-absent reworking, Strangways Range, Arunta Block, central Australia. *Journal of Metamorphic Geology*, **26,** 603-622.

Droop, G. T. R., 1987. A general equation for estimating Fe^{3+} concentrations in ferromagnesian silicates and oxides from microprobe analyses, using stoichiometric criteria. *Mineralogical Magazine*, **51,** 431-435.

Dunlap, W. J., Hirth, G. & Teyssier, C., 1997. Thermomechanical evolution of a ductile duplex. *Tectonics*, **16,** 983-1000.

Dutch, R. A., Hand, M., & Kelsey, D. E., 2010. Unravelling the tectonothermal evolution of reworked Archean granulite facies metapelites using *in situ* geochronology: an example from the Gawler Craton, Australia. *Journal of Metamorphic Geology*, **28,** 293-316.

Dziggel, A., Diener, J. F. A., Stoltz, N. B. & Kolb, J., 2012. Role of H_2O in the formation of garnet coronas during near-isobaric cooling of mafic granulites: The Tasiusarsuaq terrane: southern West Greenland. *Journal of Metamorphic Geology*, **30,** 957-972.

England, P. C. & Thompson, A. B., 1984. Pressure-temperature-time paths of regional metamorphism I. Heat transfer during the evolution of regions of thickened continental crust. *Journal of Petrology*, **25,** 894-928.

Faak, K., Chakraborty, S. & Dasgupta, S., 2012. Petrology and tectonic significance of metabasite slivers in the Lesser and Higher Himalayan domains of Sikkim, India. *Journal of Metamorphic Geology*, **30,** 599-622.

Ferrar, G. R., 1995. *The metamorphic geology of the Armalsryggen, northern Kirwanveggen, western Dronning Maud Land, Antarctica*. Unpublished M.Sc. Thesis, University of Natal, Pietermaritzburg, 116 pp.

Fitzsimons, I. C. W., 2000. A review of tectonic events in the East Antarctic Shield and their implications for Gondwana and earlier supercontinents. *Journal of African Earth Sciences*, **31:1,** 3-23.

Frimmel, H. E., 2004. Formation of a late Mesoproterozoic supercontinent: the South Africa-East Antactica connection. In: Eriksson, P. G., Altermann, W., Nelson, D. R., Mueller, W. U., Catuneanu, O. (eds.), *The Precambrian Earth: Tempos and Events*, *vol. 12 of Developments in Precambrian Geology. Elsevier, Amsterdam*, 240-255.

Fyfe, W. S., 1973. The granulites facies, partial melting and the Archaean crust. *Philosophical Transactions of the Royal Society, London*, **A273,** 457-461.

Geng, Y., Du, L. & Ren, L., 2012. Growth and reworking of the early Precambrian continental crust in the North China Craton: Constraints from zircon Hf isotopes. *Gondwana Research*, **21,** 517-529.

Golynsky, A. & Jacobs, J., 2001. Grenville-age versus Pan-Africa magnetic anomaly imprints in Western Dronning Maud Land, East Antarctica. *Journal of Geology*, **109,** 136-142.

Goscombe, B., 1992. High-grade reworking of central Australian granulites. Part 1: structural evolution. *Tectonophysics*, **204,** 361-399.

Goscombe, B., Armstrong, R. & Barton, J.M., 1998. Tectonometamorphic evolution of the Chewore Inliers: Partial re-equilibration of high-grade basement during the Pan-African orogeny. *Journal of Petrology*, **39,** 1347-1384.

Grantham, G. H., 1992. *Geological evolution of Western H.U. Sverdrupfjella, Dronning Maud Land, Antarctica.* PhD Thesis. University of Natal, Pietermaritzburg, 322 pp.

Grantham, G. H., 1996. Aspects of Jurassic magmatism and faulting in western Dronning Maud Land, Antarctica: implications for Gondwana break-up. In: Storey, B. C., King, E. C. & Livermore, R. A. (eds.), *Weddell Sea tectonics and Gondwana break-up*. *Geological Society Special Publications, London*, **108**, 63-71.

Grantham, G. H., Groenewald, P. B. & Hunter, D. R., 1988. Geology of the northern H.U. Sverdrupfjella, western Dronning Maud Land, and implications for Gondwana reconstructions. *South African Journal of Antarctica Research*, **18,** 2-10.

Grantham, G. H., Jackson, C., Moyes, A. B., Groenewald, P. B., Harris, P. D., Ferrar, G. & Krynauw, J. R., 1995. The tectonothermal evolution of the Kirwanveggen-H.U. Sverdrupfjella areas, Dronning Maud Land, Antarctica. *Precambrian Research*, **75,** 209-229.

Grantham, G. H., Manhica, A. D. S. T., Armstrong, R. A., Kruger, F. J. & Loubster, M., 2011. New SHRIMP, Rb/Sr and Sm/Nd isotope and whole rock chemical data from central Mozambique and western Dronning Maud Land, Antarctica: implications for the nature of the eastern margin of the Kalahari Craton and the amalgamation of Gondwana. *Journal of African Earth Sciences*, **59,** 74-100.

Grantham, G. H., Moyes, A. B. & Hunter, D. R., 1991. The age, petrogenesis and emplacement of the Dalmation Granite, H.U. Sverdrupfjella, Dronning Maud Land, Antarctica. *Antarctic Science*, **3,** 197-204.

Groenewald, P. B., 1995. *The geology of northern H.U. Sverdrupfjella and its bearing on crustal evolution in Dronning Maud Land, Antarctica*. Unpublished Ph.D. Thesis, University of Natal, Pietermaritzburg, 320 pp.

Groenewald, P. B. & Hunter, D. R., 1991. Granulites of the northern H.U. Sverdrupfjella, western Dronning Maud Land: metamorphic history from garnet-pyroxene assemblages, coronas and hydration reactions. In: Thomson, M. R. A. Crame, J. A. & Thomson, J. W. (eds.), *Geological Evolution of Antarctica. Cambridge University Press, Cambridge*, 61-66.

Groenewald, P. B., Grantham, G. H. & Watheys, M. K., 1991. Geological evidence for a Proterozoic to Mesozoic link between southeastern Africa and Dronning Maud Land, Antarctica. *Journal of the Geological Society, London*, **148,** 1115-1123.

Groenewald, P. B., Moyes, A. B., Grantham, G. H. & Krynauw, J. R., 1995. East Antarctic crustal evolution: geologic constraints and modelling in western Dronning Maud Land. *Precambrian Research*, **75,** 231-250.

Grosch, E. G., Bisnath, A., Frimmel, H. E. & Board, W. S., 2007. Geochemistry and tectonic setting of mafic rocks in western Dronning Maud Land, East Antarctica: implications for the geodynamic evolution of the Proterozoic Maud Belt. *Journal of the Geological Society, London,* **164,** 465-475.

Guiraud, M., Powell, R. & Rebay, G., 2001. H_2O in metamorphism and unexpected behaviour in the preservation of metamorphic mineral assemblages. *Journal of Metamorphic Geology*, **19,** 445-454.

Halpern, M. 1970. Rubidium-strontium date of possibly 3 billion years for a granitic rock from Antarctica. *Science*, **164,** 977-978.

Hand, M. & Buick, I. S., 2001. Tectonic evolution of the Reynolds-Anmatjira Ranges: a case study in terrain reworking from the Arunta Inlier, central Australia. In: Miller, J. A., Holdsworth, R. E., Buick, I. S. & Hand, M. (eds.), *Continental reactivation and reworking*. *Geological Society, Special Publications*, *London*, **184,** 237-260.

Harley, S. L., Fitzsimmons, I. C. W., Buick, I. S. & Watt, G., 1992. The significance of reworking, fluids and partial melting in granulite metamorphism, East Prydz Bay, Antarctica. *Recent Progress in Antarctic Earth Science*, 119-127

Harley, S. L., Fitzsimons, I. C. W. & Zhao, Y., 2013. Antarctica and supercontinent evolution: historical perspectives, recent advances and unresolved issues. In: *Antarctica and Supercontinent Evolution. Geological Society, London, Special Publications*, **383,** 1-34.

Harris, C. & Grantham, G. H., 1993. Geology and petrogenesis of the Straumsvola nepheline syenite complex, Dronning Maud Land. *Antarctica Geological Magazine*, **130,** 523-532.

Harris, C., Marsh, J. S., Duncan, A. R. & Erlank, A. J., 1990. The petrogenesis of the Kirwan Basalts of Dronning Maud Land, Antarctica. *Journal of Petrology,* **31,** 341-369.

Harris, P. D., 1999. *The geological evolution of Neumayerskarvet in the Northern Kirwanveggen, Western Dronning Maud Land, Antarctica.* Unpublished Ph.D. Thesis, Rand Afrikaans University, Johannesburg, 249 pp.

Harris, P. D., Moyes, A. B., Fanning, C. M. & Armstrong, R. A., 1995. Zircon ion microprobe results from the Maudheim high-grade gneiss terrane, western Dronning Maud Land, Antarctica. *Extended Abstracts, Centennial Geocongress, Rand Afrikaans University, Johannesburg, South Africa*, 240-243.

Hirth, G. & Tullis, J., 1992. Dislocation creep regimes in quartz aggregates. *Journal of Structural Geology,* **14,** 145-159.

Hirth, G., Teyssier, C. & Dunlap, W. J., 2001. An evaluation of quartzite flow laws based on comparisons between experimentally and naturally deformed rocks. *International Journal of Earth Sciences*, **90,** 77-87.

Hjelle, A., 1972. Some observations on the geology of H.U. Sverdrupfjella, Dronning Maud Land. *Norsk Polarinstitutt, Arbok*, 7-22.

Holdsworth, R. E., Handa, M., Miller, J. A., & Buick, I. S., 2001. Continental reactivation and reworking: an introduction. In: Miller, J. A., Holdsworth, R. E., Buick, I. S. & Hand, M. (eds.), *Continental reactivation and reworking*. *Geological Society, Special Publications*, *London*, **184,** 1-12.

Hollister, L. S., 1969. Metastable paragenetic sequence of andalusite, kyanite, and sillimanite, Kwoiek area, British Colombia. *American Journal of Science,* **267,** 352-370.

Hutton, D. H. W., 1988. Granite emplacement mechanisms and tectonic controls: inferences from deformation studies. *Transactions of the Royal Society of Edinburgh: Earth Sciences,* **79,** 245-255.

Jackson, C., 1997. Characterisation of Mesoproterozoic to Palaeozoic Crustal Evolution of Western Dronning Maud Land. Study three: Deformation history and thermochronology of the central Kirwanveggen. *South African National Antarctic Program final report*, 40 pp.

Jackson, C., 1999. Characterisation of Mesoproterozoic to Palaeozoic Crustal Evolution of Western Dronning Maud Land. Study three: Deformation history and thermochronology of the central Kirwanveggen. *South African National Antarctic Program final report*, 79 pp.

Jacobs, J. & Thomas, R. J., 2004. Himalayan-type indenter-escape tectonics model for the southern part of the late Neoproterozoic-early Palaeozoic East African-Antarctic orogeny. Geology. *Geology,* **32,** 721-724.

Jacobs, J., Ahrendt, H., Kreutzer, H. & Weber, K., 1995. K-Ar, ^{40}Ar-^{39}Ar and apatite fission-track evidence for Neoproterozoic and Mesozoic basement rejuvenation events in the Heimefrontfjella and Mannefallknausane (East Antarctica). *Precambrian Research,* **75,** 251-262.

Jacobs, J., Bauer, W., Spaeth, G, Thomas, R. J. & Weber, K., 1996. Lithology and structure of the Grenville-aged (~1.1 Ga) basement of Heimefrontfjella (East Antarctica). *Geologische Rundschau,* **85,** 800-821.

Jacobs, J., Fanning, C. M., Henjes-Kunst, F., Olesch, M. & Paech, H. -J., 1998. Continuation of the Mozambique Belt into East Antarctica: Grenville-aged metamorphism and polyphase Pan-African high-grade events in central Dronning Maud Land, *Journal of Geology*, **106,** 385-406.

Jacobs, J., Fanning, C. M. & Bauer, W., 2003. Timing on Grenville-age v. Pan-African medium- to high-grade metamorphism in western Dronning Maud Land (East Antarctica) and significance for correlations in Rodinia and Gondwana. *Precambrian Research*, **125,** 1-20.

Jacobs, J., Hansen, B. T., Henjes-Kunst, F., Thomas, R. J., Bauer, W., Weber, K., Armstrong, R. A. & Cornell, D. H., 1999. New age constraints on the Proterozoic/lower Palaeozoic evolution of Heimefrontfjella, East Antarctica, and its bearing on Rodinia/Gondwana correlations. *Terra Antarctica*, **6,** 377-387.

Jacobs, J. Thomas, R. J. & Weber, K., 1993. Accretion and indentation tectonics at the southern edge of the Kaapvaal craton during the Kibaran (Grenville) orogeny. *Geology,* **21,** 203-206.

Jamieson, R.A. & Beaumont, C., 2013. On the origin of orogens. *Geological Society of America Bulletin*, **125,** 1671-1702.

Kelsey, D. E., 2008. On ultrahigh-temperature crustal metamorphism. *Gondwana Research*, **13,** 1-29.

Kleinschmidt, G., Helferich, S., Henjes-Kunst, F., Jackson, C. & Frimmel, H. E., 2000. The pre-Permo-Carboniferous rocks and structures from southern Kirwanveggen, Dronning Maud Land, Antarctica. *Polarforschung*, **6,** 7-18.

Krynauw, J. R., 1996. A review of the geology of East Antarctica, with special reference to the c.1000 Ma and c.500 Ma events. *Terra Antarctica,* **3,** 77-89.

Liu, Y. & Zhong, D., 1997. Petrology of high-pressure granulites from the eastern Himalayan syntaxis. *Journal of Metamorphic Geology*, **15,** 451-466.

Liu, X., Zhao, Y. & Hu, J., 2013. The c. 1000–900 Ma and c. 550–500 Ma tectonothermal events in the Prince Charles Mountains–Prydz Bay region, East Antarctica, and their relations to supercontinent evolution. In: Harley, S. L., Fitzsimons, I. C. W. & Zhao, Y. (eds.), *Antarctica and supercontinent evolution. Geological Society, Special Publications*, *London*, **383,** 95-112.

Mahar, E. M., Baker, J. M., Powell, R., Holland, T. J. B. & Howell, N., 1997. The effect of Mn on mineral stability in metapelites. *Journal of Metamorphic Geology*, **15,** 223-238.

Manhica, A. D. S. T., Grantham, G. H., Armstrong, R. A., Guise, P. G. & Kruger, F. J., 2013. Polyphase deformation and metamorphism at the Kalahari Craton – Mozambique Belt

boundary. In: Miller, J.A., Holdsworth, R.E., Buick, I.S. and Hand, M. (eds.), *Continental reactivation and reworking. Geological Society, Special Publications*, *London*, **184,** 303-322.

Marschall, H. R., Hawkesworth, C. J. & Leat, P. T., 2013. Mesoproterozoic subduction under the eastern edge of the Kalahari-Grunehogna Craton preceding Rodinia assembly: The Ritscherflya detrital zircon record, Ahlmannryggen (Dronning Maud Land, Antarctica). *Precambrian Research,* **236,** 31-45.

Marschall, H. R., Hawkesworth, C. J., Storey, C. D., Dhuime, B., Leat, P. T., Meyer, H-P & Tamm-Buckle, S., 2010. The Annandagstoppane granite, East Antarctica: evidence for Archaean intracrustal recycling in the Kaapvaal-Grunehogna craton from zircon O and Hf isotopes. *Journal of Petrology*, **51,** 2277-2301.

Martin, A. K. & Hartnady, C. J. H. 1986. Plate tectonic development of the south-west Indian Ocean: a revised reconstruction of east Antarctica and Africa. *Journal of Geophysical Research,* **91,** 4767-4778.

McGibbon, D., 2014. *Shear zones of the Maud Belt, Antarctica: Kinematics and deformation mechanisms.* Unpublished M.Sc. thesis. University of Cape Town, Cape Town, 120 pp.

Morimoto, N., Fabries, J., Ferguson, A. K., Ginzburg, I. V., Ross, M., Seifert, F. A. & Zussman, J., 1988. Nomenclature of pyroxenes. *Mineralogical magazine*, **52,** 535-550.

Moyes, A. B. & Barton, J. M., Jr., 1990. A review of isotopic data from western Dronning Maud Land, Antarctica. Z. Geol. *Paläontologie*, **1,** 19-31.

Moyes, A. B. & Groenewald, P. B., 1996. Isotopic constraints on Pan-African metamorphism in Dronning Maud Land, Antarctica. *Chemical Geology*, **129,** 247-256.

Moyes, A. B., Groenewald, P. B. & Brown, R. W., 1993. Isotopic constraints on the age and origin of the Brattskarvet intrusive suite, Dronning Maud Land, Antarctica. *Chemical Geology*, **107,** 453-466.

Moyes, A. B., Knoper, M. W. & Harris, P. D., 1997. The age and significance of the Urfjell Group, western Dronning Maud Land. In: Ricci, C. A. (ed.), *The Antarctic Region: Geological Evolution and Progress, Terra Antarctica Publications, Siena,* 31-36.

Moyes, A. B., Krynauw, J. R. & Barton, J. M., 1995. The age of the Richtersflya Supergroup and Borgmassivet intrusions, Dronning Maud Land (Antarctica). *Antarctica Science,* **7,** 87-97.

Newton, R. C., 1983. Geobarometry of high-grade metamorphic rocks. *American Journal of Science*, **283A,** 1-28.

Ohta, Y. (ed.), 1996. Nature environment map, H.U. Sverdrupfjella 1:150 000, *Norsk Polarinstitutt Ternakaart,* **nr. 28,** 1996.

Parrish, R. R., 2001. The response of mineral chronometers to metamorphism and deformation in orogenic belts. In: Miller, J.A., Holdsworth, R.E., Buick, I.S. and Hand, M. (eds.), *Continental reactivation and reworking. Geological Society, Special Publications*, *London*, **184,** 289-301.

Passchier, C. W., & Trouw, R. A., 1996. Microtectonics. *Springer, Berlin.* 366 pp.

Paterson, M. S., 2001. A granular flow theory for the deformation of partially molten rock. *Tectonophysics*, **335,** 51-61.

Peters, M., Haverkamp, B., Emmermann, R., Kohnen, H. & Weber, K., 1991. Paleomagnetism, K-Ar dating and geodynamic setting of igneous rocks in western and central Neuschwabenland, Antarctica. In: Thomsan, M. R. A., Crame, J. A., Thomson, J. W. (eds.) *Geological Evolution of Antarctica, vol. 1 of World and Regional Geology. Cambridge University Press, Cambridge,* 549-555.

Petford, N., Cruden, A. R., McCaffrey, K. J. W. & Vigneresse, J. –L, 2000. Granite magma formation, transport and emplacement in the Earth's crust. *Nature*, **408,** 669-673.

Phillips, G., Kelsey, D. E., Corvino, A. F. & Dutch, R. A., 2009. Continental Reworking during Overprinting Orogenic Events, Southern Prince Charles Mountains, East Antarctica. *Journal of Petrology*, **50,** 2017-2041.

Powell, R. & Holland, T. J. B., 2008. On thermobarometry. *Journal of Metamorphic Geology*, **26,** 155-179.

Raase, P., Raith, M., Achermand, D. & Lal, R. K., 1986. Progressive metamorphism of mafic rocks from greenschist to granulite facies in the Dharwar Craton of South India. *The Journal of Geology,* **94,** 261-282.

Ravich, M. G. & Solo'vev, D. S., 1966. Geology and petrology of the mountains of central Queen Maud Land (East Antarctica). *Transactions Scientific Research Institute Antarctic*

Geology, **141,** 348 pp. *Ministry of Geology of the U.S.S.R. (Israel Program for Scientific Translations, Jerusalem, 1969).*

Ring, U., 1994. The influence of pre-existing structure on the evolution of the Cenozoic Malawi Rift (East African Rift System). *Tectonics*, **13:2,** 313-326.

Roots, E. F., 1969. Geology of Western Dronning Maud Land. *Explanation of Plate VI, Folio 12, Antarctic Map Series, American Geophysical Union*.

Santosh, M., Yokoyama, K., Biju-Sekhar, S., & Rogers, J. J. W. 2003. Multiple tectonothermal events in the granulite blocks of southern India revealed from EPMA dating: implications on the history of supercontinents. *Gondwana Research*, **6,** 29-63.

Sarkar, M., Gupta, S. & Panigrahi, M. K., 2007. Disentangling tectonic cycles along a multiply deformed terrane margin: Structural and metamorphic evidence for mid-crustal reworking of the Angul granulite complex, Eastern Ghats Belt, India. *Journal of Structural Geology*, **29,** 802-818.

Sawyer, E. W., 2001. Melt segregation in the continental crust: distribution and movement of melt in anatectic rocks. *Journal of Metamorphic Geology*, **19,** 291-309.

Scrimgeour, I. R. & Raith, J. G., 2001. High-grade reworking of Proterozoic granulites during Ordovician intraplate tranpression, eastern Arunta Inlier, central Australia. In: Miller, J.A., Holdsworth, R.E., Buick, I.S. and Hand, M. (eds.), *Continental Reworking and Reactivation. Geological Society, Special Publications*, *London*, **184,** 261-287.

Scrimgeour, I. R., Kinny, P. D., Close, D. F. & Edgoose, C. J., 2005. High-T granulites and polymetamorphism in the southern Arunta region, central Australia: Evidence for a 1.64 Ga accretional event. *Precambrian Research*, **142,** 1-27.

Shaw, R. K., Arima, M., Kagami, H., Fanning, C. M., Shiraishi, K. & Motoyoshi, Y., 1997. Proterozoic events in the Eastern Ghats granulite Belt, India: Evidence from Rb-Sr, Sm-Nd systematics and SHRIMP dating. *The Journal of Geology*, **105:5,** 645-656.

Shiraishi, K., Ellis, D. J., Hiroi, Y., Fanning, C. M., Motoyoshi, Y. & Nakai, Y., 1994. Cambrian Orogenic Belt in East Antarctica and Sri Lanka: Implications for Gondwana Assembly. *Journal of Geology*, **102,** 47-65.

Simmat, R. & Raith, M. M., 2008. U-Th-Pb monazite geochronometry of the Eastern Ghats Belt, India: timing and spatial disposition of poly-metamorphism. *Precambrian Research*, **162,** 16-39.

Sommer, H., Kröner, A., Hauzenberger, C. & Muhongo, S., 2005. Reworking of Archaean and Palaeoproterozoic crust in the Mozambique belt of central Tanzania as documented by SHRIMP zircon geochronology. *Journal of African Earth Sciences*, **43,** 447-463.

Stipp, M. & Tullis, J., 2003. The recrystallised grain size piezometer for quartz. *Geophysical Research Letters*, **30,** 2088-2093.

Stipp, M., Stünitz, H., Heilbronner, R. & Schmid, S., 2002a. Dynamic recrystallisation of quartz: correlation between natural and experimental conditions. *Geological Society, Special Publications, London*, **200,** 171-190.

Stipp, M., Stünitz, H., Heilbronner, R. & Schmid, S., 2002b. The eastern Tonale fault zone: a natural laboratory for crystal plastic deformation of quartz over a temperature range from 250 to 700 ºC. *Journal of Structural Geology*, **24,** 1861-1884.

Tenczer, V., Powell, R. & Stüwe, K., 2006. Evolution of H_2O content in a polymetamorphic terrane: the Plattengneiss Shear Zone (Koralpe, Austria). *Journal of Metamorphic Geology*, **24,** 281-295.

Thomas, S., 2014. *Metamorphic and melt-migration history of midcrustal migmatitic gneisses from Nupskåpa, the Maud Belt, Antarctica*. Unpublished M.Sc. thesis. University of Cape Town, Cape Town. 161 pp.

Tracy, R. J. & Robinson, P., 1976. Garnet composition and zoning in the determination of temperature and pressure of metamorphism, central Massachusetts. *American Mineralogist*, **61,** 762-775.

Tuccillo, M. E., Essene, E. J. & van der Pluijm, B. A., 1990. Growth and retrograde zoning in garnets from high-grade, metapelites: Implications for pressure-temperature paths. *Geology,* **18,** 839-842.

Twiss, R. J., 1977. Theory and applicability of a recrystallized grain size paleopiezometer. *Pure and Applied Geophysics,* **115,** 227-244.

Van Reenen, D. D., Barton, J. M., Jr., Roering, C., Smith, C. A. & Van Schalkwyk, J. F., 1987. Deep crustal response to continental collision: The Limpopo belt of southern Africa. *Geology*, **15,** 11-14.

Vanderhaeghe, O., 2001. Melt segregation, pervasive melt migration and magma mobility in the continental crust: The structural record from pores to orogens. *Physics and Chemistry of the Earth,* **26,** 213-223.

Vauchez, A., Barruol, G. & Tommasi, A., 1997. Why do continents break up parallel to ancient orogenic belts? *Terra Nova*, **9,** 62-66.

Vielzeuf, D., Vidal, P. (Eds), Granulites and Crustal Evolution. *NATO Scientific Publication, Kluwer Academic Publishers, Dordrecht,* **311,** 59-85.

Watson, J. V., 1973. Effects of reworking on high-grade gneiss complexes. *Philosophical Transactions of the Royal Society of London*, **A273,** 443-455.

White, R. W. & Powell, R., 2002. Melt loss and the preservation of granulite facies mineral assemblages. *Journal of Metamorphic Geology*, **20,** 621-632.

White, R. W. & Powell, R., 2010. Retrograde melt-residue interaction and the formation of near-anhydrous leucosomes in migmatites. *Journal of Metamorphic Geology*, **28,** 579-597.

White, R. W., Powell, R. & Haplin, J., 2004. Spatially-focussed melt formation in aluminous metapelites from Broken Hill, Australia. *Journal of Metamorphic Geology*, **22,** 825-845.

White, R.W., Powell, R. & Holland, T. J. B., 2001. Calculation of partial melting equilibria in the system Na_2O-CaO-K_2O-FeO-MgO-Al_2O-SiO_2-H_2O (NCKFMASH). *Journal of Metamorphic Geology*, **19,** 139-153.

Wolmarans, L. G. & Kent, L. E., 1982. Geological investigations in Western Dronning Maud Land, Antarctica – a synthesis. *South African Journal of Antarctic Research,* **Supplement 2,** 93 pp.

Zhao, G., Cawood, P. A., Wilde, S. A., & Sun, M., 2001. Polymetamorphism of mafic granulites in the North China Craton: textural and thermobarometric evidence and tectonic implications. In: Miller, J.A., Holdsworth, R.E., Buick, I.S. and Hand, M. (eds.), *Continental Reworking and Reactivation. Geological Society, Special Publications*, *London*, **184,** 323-341.

Appendix: Microprobe results

Table A.1: Garnet

Analysis ID	73g_d1.1	73g_d1.2	73g_d1.3	73g_d1.4	73g_d2.1	73g_d2.2	73g_d2.3	73g_d2.4	73g_d3	73g_d4.1	73g_d4.2	73g_d4.3	73g_d4.4	73g_d5.1	73g_d5.2
area probed in garnet	core	inter	inter	rim	core	inter	inter	rim	core	core	inter	inter	rim	core	inter
SiO2	37.41	37.46	37.46	37.45	37.77	37.58	37.58	37.55	37.44	37.61	37.62	37.76	37.26	37.94	37.68
TiO2	0.00	0.03	0.03	0.00	0.01	0.01	0.01	0.01	0.02	0.00	0.02	0.04	0.00	0.00	0.00
Al2O3	22.05	22.04	22.51	22.01	22.32	22.10	22.39	22.37	22.19	21.90	21.82	22.05	21.58	21.75	21.74
Cr2O3	0.03	0.04	0.00	0.03	0.03	0.00	0.00	0.03	0.07	0.02	0.00	0.01	0.03	0.00	0.05
FeO	33.13	33.28	33.40	33.64	32.95	33.13	33.31	33.69	34.08	32.93	33.01	33.29	33.68	33.15	33.58
MnO	3.13	3.05	3.12	3.47	2.83	2.84	3.02	3.44	3.36	2.78	3.06	2.99	3.28	3.00	3.05
MgO	2.97	3.07	2.99	2.59	3.31	3.31	3.30	2.81	2.64	3.30	3.16	3.04	2.90	3.22	3.21
CaO	1.32	1.24	1.16	1.29	1.52	1.32	1.32	1.03	1.14	1.64	1.67	1.35	1.15	1.55	1.46
Na2O	0.00	0.00	0.00	0.00	0.00	0.03	0.00	0.01	0.00	0.03	0.00	0.00	0.00	0.00	0.00
K20	0.00	0.00	0.00	0.00	0.00	0.00	0.00	0.00	0.00	0.00	0.00	0.00	0.00	0.00	0.00
Total	100.04	100.22	100.67	100.48	100.74	100.34	100.93	100.93	100.94	100.21	100.36	100.53	99.89	100.61	100.77
Si	2.99	2.99	2.98	2.99	2.99	2.99	2.98	2.98	2.98	3.00	3.00	3.00	3.00	3.01	3.00
Ti	0.00	0.00	0.00	0.00	0.00	0.00	0.00	0.00	0.00	0.00	0.00	0.00	0.00	0.00	0.00
Al	2.08	2.07	2.11	2.07	2.08	2.07	2.09	2.09	2.08	2.06	2.05	2.07	2.05	2.04	2.04
Cr	0.00	0.00	0.00	0.00	0.00	0.00	0.00	0.00	0.00	0.00	0.00	0.00	0.00	0.00	0.00
Fe	2.22	2.22	2.22	2.25	2.18	2.21	2.21	2.24	2.27	2.19	2.20	2.21	2.27	2.20	2.23
Mn	0.21	0.21	0.21	0.23	0.19	0.19	0.20	0.23	0.23	0.19	0.21	0.20	0.22	0.20	0.21
Mg	0.35	0.37	0.35	0.31	0.39	0.39	0.39	0.33	0.31	0.39	0.38	0.36	0.35	0.38	0.38
Ca	0.11	0.11	0.10	0.11	0.13	0.11	0.11	0.09	0.10	0.14	0.14	0.11	0.10	0.13	0.12
Na	0.00	0.00	0.00	0.00	0.00	0.01	0.00	0.00	0.00	0.00	0.00	0.00	0.00	0.00	0.00
K	0.00	0.00	0.00	0.00	0.00	0.00	0.00	0.00	0.00	0.00	0.00	0.00	0.00	0.00	0.00
Total	7.97	7.97	7.97	7.97	7.97	7.97	7.98	7.97	7.97	7.98	7.98	7.96	7.98	7.97	7.98

Analysis ID format = (sample number, mineral abbreviation _ probe session, grain number and number of spot on grain)

Table A.1: Garnet (continued)

Analysis ID	73g_d5.3	77g_a1	77g_a2	77g_a3	77g_b3.1	77g_b3.2	77g_b3.3	77g_b4	77g_b5.1	77g_b5.2	77g_b6.2	77g_b7.3	101g_c1.2	101g_c1.3	101g_c2.1
area probed in garnet	rim	core	core	core	core	core	rim	core	core	rim	rim	rim	inter	rim	core
SiO2	37.72	36.95	37.35	37.08	37.47	37.77	37.40	37.34	37.51	37.35	37.55	37.00	38.23	37.91	38.61
TiO2	0.00	0.01	0.02	0.01	0.00	0.02	0.03	0.02	0.03	0.00	0.02	0.00	0.04	0.01	0.02
Al2O3	21.77	21.74	21.47	21.44	21.73	21.78	21.58	21.90	21.60	21.62	21.50	21.58	22.19	21.74	22.31
Cr2O3	0.00	0.00	0.04	0.03	0.02	0.04	0.02	0.04	0.01	0.06	0.07	0.07	0.00	0.03	0.04
FeO	33.73	34.07	34.01	34.53	33.49	33.73	34.45	34.08	34.17	34.34	34.71	34.41	25.77	28.10	25.16
MnO	3.49	3.05	3.41	3.22	2.74	2.83	3.29	3.07	3.10	3.62	3.63	3.34	1.20	1.85	0.88
MgO	2.72	2.76	2.53	2.35	3.17	3.04	2.42	2.96	2.68	2.00	2.09	2.50	3.59	3.11	4.31
CaO	1.12	1.30	1.15	1.27	1.51	1.58	1.28	1.36	1.52	1.11	1.14	1.15	9.24	6.76	9.36
Na2O	0.00	0.00	0.03	0.02	0.00	0.00	0.00	0.00	0.01	0.04	0.01	0.03	0.00	0.00	0.00
K20	0.00	0.00	0.00	0.00	0.00	0.00	0.00	0.00	0.00	0.00	0.00	0.00	0.00	0.00	0.00
Total	100.55	99.88	100.01	99.96	100.13	100.80	100.47	100.77	100.63	100.13	100.71	100.07	100.26	99.51	100.69
Si	3.01	2.98	3.01	2.99	3.00	3.00	3.00	2.98	3.00	3.01	3.01	2.98	2.99	3.01	2.99
Ti	0.00	0.00	0.00	0.00	0.00	0.00	0.00	0.00	0.00	0.00	0.00	0.00	0.00	0.00	0.00
Al	2.05	2.06	2.04	2.04	2.05	2.04	2.04	2.06	2.04	2.05	2.03	2.06	2.04	2.03	2.04
Cr	0.00	0.00	0.00	0.00	0.00	0.00	0.00	0.00	0.00	0.00	0.00	0.00	0.00	0.00	0.00
Fe	2.25	2.30	2.29	2.33	2.24	2.24	2.31	2.27	2.28	2.31	2.33	2.32	1.68	1.86	1.63
Mn	0.24	0.21	0.23	0.22	0.19	0.19	0.22	0.21	0.21	0.25	0.25	0.22	0.08	0.12	0.06
Mg	0.32	0.33	0.30	0.28	0.38	0.36	0.29	0.35	0.32	0.24	0.25	0.29	0.42	0.37	0.50
Ca	0.10	0.11	0.10	0.11	0.13	0.13	0.11	0.12	0.13	0.10	0.10	0.10	0.77	0.57	0.78
Na	0.00	0.00	0.01	0.00	0.00	0.00	0.00	0.00	0.00	0.01	0.00	0.00	0.00	0.00	0.00
K	0.00	0.00	0.00	0.00	0.00	0.00	0.00	0.00	0.00	0.00	0.00	0.00	0.00	0.00	0.00
Total	7.97	7.99	7.98	7.99	7.98	7.98	7.98	7.99	7.98	7.97	7.97	7.99	7.99	7.97	7.99

Analysis ID format = (sample number, mineral abbreviation _ probe session, grain number and number of spot on grain)

Table A.1: Garnet (continued)

Analysis ID	101g_c2.2	101g_c3.1	101g_c3.2	101g_c3.3	101g_c3.4	101g_c3.5	101g_c3.6	101g_c3.7	101g_c4.2	101g_c4.3	101g_c4.4	101g_c4.5	101g_c5.1	101g_c5.2
area probed in garnet	inter	core	inter	inter	inter	inter	inter	rim	inter	inter	inter	rim	core	inter
SiO2	38.20	38.80	38.82	38.77	38.39	38.25	38.62	38.29	38.44	38.86	38.34	38.23	38.90	38.61
TiO2	0.00	0.01	0.04	0.02	0.06	0.03	0.04	0.01	0.00	0.07	0.04	0.03	0.04	0.03
Al2O3	21.89	22.36	22.39	22.17	22.16	21.93	22.16	22.05	22.15	22.32	21.99	22.08	22.27	22.14
Cr2O3	0.04	0.00	0.00	0.02	0.00	0.00	0.03	0.04	0.00	0.00	0.00	0.00	0.02	0.00
FeO	26.71	24.81	24.70	24.98	26.22	27.49	26.86	28.02	25.00	21.98	26.61	28.63	24.10	24.05
MnO	1.27	1.02	0.91	1.03	1.19	1.38	1.50	2.03	1.09	0.51	1.51	2.57	0.88	0.93
MgO	3.73	4.17	4.01	3.93	3.97	3.42	3.27	3.10	3.47	4.38	3.43	2.62	4.60	4.44
CaO	8.14	9.94	9.96	9.93	8.92	8.24	8.94	6.89	10.18	12.36	8.36	6.42	9.72	10.02
Na2O	0.02	0.00	0.02	0.04	0.02	0.01	0.00	0.01	0.03	0.00	0.00	0.07	0.00	0.01
K20	0.00	0.00	0.00	0.00	0.00	0.00	0.00	0.00	0.00	0.00	0.00	0.00	0.00	0.00
Total	100.00	101.11	100.84	100.89	100.93	100.75	101.42	100.44	100.37	100.48	100.28	100.65	100.52	100.23
Si	3.00	2.99	3.00	3.00	2.98	2.99	3.00	3.01	3.00	2.99	3.00	3.01	3.00	3.00
Ti	0.00	0.00	0.00	0.00	0.00	0.00	0.00	0.00	0.00	0.00	0.00	0.00	0.00	0.00
Al	2.03	2.03	2.04	2.02	2.03	2.02	2.03	2.04	2.03	2.03	2.03	2.05	2.03	2.02
Cr	0.00	0.00	0.00	0.00	0.00	0.00	0.00	0.00	0.00	0.00	0.00	0.00	0.00	0.00
Fe	1.75	1.60	1.60	1.62	1.70	1.80	1.74	1.84	1.63	1.42	1.74	1.88	1.56	1.56
Mn	0.08	0.07	0.06	0.07	0.08	0.09	0.10	0.14	0.07	0.03	0.10	0.17	0.06	0.06
Mg	0.44	0.48	0.46	0.45	0.46	0.40	0.38	0.36	0.40	0.50	0.40	0.31	0.53	0.51
Ca	0.68	0.82	0.82	0.82	0.74	0.69	0.74	0.58	0.85	1.02	0.70	0.54	0.80	0.83
Na	0.00	0.00	0.00	0.01	0.00	0.00	0.00	0.00	0.00	0.00	0.00	0.01	0.00	0.00
K	0.00	0.00	0.00	0.00	0.00	0.00	0.00	0.00	0.00	0.00	0.00	0.00	0.00	0.00
Total	7.99	7.99	7.98	7.99	8.00	8.00	7.99	7.97	7.99	7.99	7.98	7.97	7.98	7.99

Analysis ID format = (sample number, mineral abbreviation _ probe session, grain number and number of spot on grain)

Table A.1: Garnet (continued)

Analysis ID	101g_c5.3	101g_c5.4	101g_c5.5	101g_c6.1	101g_c6.2	101g_c6.3	101g_c6.4	116g_d1.1	116g_d1.2	152g_b1.1	152g_b1.2	152g_b2.1	152g_b3.1	152g_b3.2
area probed in garnet	inter	inter	rim	core	inter	inter	rim	core	rim	core	rim	core	core	rim
SiO2	38.84	38.64	38.29	38.79	38.68	38.57	38.47	38.38	38.52	38.39	38.14	38.76	39.00	38.19
TiO2	0.03	0.04	0.02	0.00	0.04	0.05	0.03	0.06	0.00	0.00	0.00	0.12	0.09	0.00
Al2O3	22.06	22.02	21.84	22.22	22.24	21.78	22.00	21.12	20.54	22.11	21.95	22.30	22.57	22.33
Cr2O3	0.05	0.01	0.01	0.01	0.05	0.05	0.03	0.00	0.04	0.05	0.00	0.11	0.09	0.07
FeO	24.82	25.88	28.36	24.94	25.00	25.90	28.28	25.15	26.15	24.40	27.23	20.29	19.61	26.85
MnO	0.98	1.23	2.24	0.92	0.99	1.30	2.04	0.90	1.17	1.40	2.64	1.21	1.23	2.58
MgO	3.94	3.65	2.83	4.05	4.00	3.69	3.18	3.19	2.82	5.41	5.02	5.73	5.73	4.87
CaO	9.63	9.30	6.71	9.90	9.52	8.86	6.78	10.96	10.85	8.32	4.61	11.27	12.50	5.62
Na2O	0.00	0.00	0.00	0.01	0.03	0.02	0.00	0.03	0.06	0.00	0.00	0.05	0.00	0.01
K20	0.00	0.00	0.00	0.00	0.00	0.00	0.00	0.00	0.00	0.00	0.00	0.00	0.00	0.00
Total	100.35	100.77	100.31	100.84	100.55	100.21	100.81	99.80	100.15	100.08	99.59	99.84	100.81	100.52
Si	3.02	3.00	3.02	3.00	3.00	3.01	3.01	3.02	3.04	2.98	3.00	2.98	2.97	2.98
Ti	0.00	0.00	0.00	0.00	0.00	0.00	0.00	0.00	0.00	0.00	0.00	0.01	0.00	0.00
Al	2.02	2.02	2.03	2.03	2.03	2.01	2.03	1.96	1.91	2.02	2.04	2.02	2.03	2.05
Cr	0.00	0.00	0.00	0.00	0.00	0.00	0.00	0.00	0.00	0.00	0.00	0.01	0.01	0.00
Fe	1.61	1.68	1.87	1.61	1.62	1.69	1.85	1.65	1.72	1.58	1.79	1.31	1.25	1.75
Mn	0.06	0.08	0.15	0.06	0.07	0.09	0.14	0.06	0.08	0.09	0.18	0.08	0.08	0.17
Mg	0.46	0.42	0.33	0.47	0.46	0.43	0.37	0.37	0.33	0.63	0.59	0.66	0.65	0.57
Ca	0.80	0.77	0.57	0.82	0.79	0.74	0.57	0.92	0.92	0.69	0.39	0.93	1.02	0.47
Na	0.00	0.00	0.00	0.00	0.01	0.00	0.00	0.01	0.01	0.00	0.00	0.01	0.00	0.00
K	0.00	0.00	0.00	0.00	0.00	0.00	0.00	0.00	0.00	0.00	0.00	0.00	0.00	0.00
Total	7.97	7.98	7.97	7.99	7.98	7.98	7.97	8.00	8.01	8.01	7.98	8.00	8.01	7.99

Analysis ID format = (sample number, mineral abbreviation _ probe session, grain number and number of spot on grain)

Table A.1: Garnet (continued)

Analysis ID	152g_b5.1	152g_b7.1	152g_b7.2	152g_b8.1	152g_b9.1	152g_b9.2	152g_c1.2	152g_c1.3	152g_c2.1	152g_c2.2	152g_c2.3	152g_c2.4	152g_c2.5	152g_c3.1
area probed in garnet	core	core	rim	core	core	rim	core	inter	rim	inter	inter	inter	core	core
SiO2	39.02	38.61	38.24	39.23	38.82	38.03	39.25	38.93	38.51	38.55	39.13	39.41	39.38	39.02
TiO2	0.07	-	0.02	0.01	0.12	0.00	0.03	0.10	0.00	0.00	0.03	0.00	0.01	0.03
Al2O3	22.46	22.79	22.31	22.58	22.52	22.28	22.46	22.51	22.20	22.42	22.61	22.43	22.66	22.49
Cr2O3	0.05	0.12	0.09	0.10	0.05	0.14	0.08	0.08	0.05	0.09	0.09	0.07	0.07	0.06
FeO	19.74	20.84	27.25	21.10	20.49	27.64	20.18	20.26	26.77	23.41	21.14	19.98	19.94	21.48
MnO	0.86	0.78	3.24	0.88	0.77	2.67	0.71	0.67	3.10	2.00	0.94	0.76	0.69	0.94
MgO	6.14	6.69	4.52	6.50	5.70	5.02	6.43	6.55	4.59	4.46	6.04	6.60	6.61	5.69
CaO	12.36	10.76	4.95	10.30	12.01	4.76	10.75	10.83	5.05	9.27	10.48	10.38	10.36	9.87
Na2O	0.00	0.00	0.03	0.01	0.02	0.00	0.01	0.00	0.02	0.00	0.00	0.02	0.01	0.02
K20	0.00	0.00	0.00	0.00	0.00	0.00	0.00	0.00	0.00	0.00	0.00	0.00	0.00	0.00
Total	100.70	100.59	100.65	100.71	100.50	100.55	99.91	99.93	100.29	100.20	100.45	99.64	99.73	99.60
Si	2.97	2.95	2.99	2.99	2.97	2.97	3.00	2.98	3.01	2.99	2.99	3.01	3.01	3.01
Ti	0.00	0.00	0.00	0.00	0.01	0.00	0.00	0.01	0.00	0.00	0.00	0.00	0.00	0.00
Al	2.02	2.05	2.05	2.03	2.03	2.05	2.02	2.03	2.04	2.05	2.04	2.02	2.04	2.04
Cr	0.00	0.01	0.01	0.01	0.00	0.01	0.01	0.00	0.00	0.01	0.01	0.00	0.00	0.00
Fe	1.26	1.33	1.78	1.34	1.31	1.81	1.29	1.30	1.75	1.52	1.35	1.28	1.27	1.38
Mn	0.06	0.05	0.21	0.06	0.05	0.18	0.05	0.04	0.21	0.13	0.06	0.05	0.04	0.06
Mg	0.70	0.76	0.53	0.74	0.65	0.58	0.73	0.75	0.53	0.52	0.69	0.75	0.75	0.65
Ca	1.01	0.88	0.41	0.84	0.98	0.40	0.88	0.89	0.42	0.77	0.86	0.85	0.85	0.81
Na	0.00	0.00	0.00	0.00	0.00	0.00	0.00	0.00	0.00	0.00	0.00	0.00	0.00	0.00
K	0.00	0.00	0.00	0.00	0.00	0.00	0.00	0.00	0.00	0.00	0.00	0.00	0.00	0.00
Total	8.01	8.02	7.98	8.00	8.01	8.00	7.98	8.00	7.97	7.98	7.99	7.97	7.97	7.97

Analysis ID format = (sample number, mineral abbreviation _ probe session, grain number and number of spot on grain)

Table A.1: Garnet (continued)

Analysis ID	152g_c3.2	152g_c3.3	152g_c4.1	152g_c4.2	152g_c4.3	152g_c4.4	152g_c5.2	152g_c5.3	152g_c5.4	152g_c6.1	152g_c6.2	152g_c6.3	152g_c7.1	158g_d1.1
area probed in garnet	inter	rim	core	inter	inter	inter	inter	inter	rim	core	inter	rim	core	core
SiO2	38.69	38.69	39.62	39.39	39.10	38.72	38.96	38.61	38.24	39.41	39.34	39.13	39.69	38.23
TiO2	0.00	0.00	0.02	0.04	0.06	0.02	0.01	0.00	0.02	0.08	0.08	0.02	0.01	0.00
Al2O3	22.20	22.16	22.31	22.42	22.38	22.25	22.15	22.87	22.04	22.54	22.47	22.41	22.52	22.18
Cr2O3	0.03	0.11	0.04	0.00	0.00	0.03	0.02	0.02	0.06	0.09	0.08	0.04	0.03	0.04
FeO	24.17	25.39	21.14	20.93	21.52	24.77	25.69	27.24	27.87	20.03	20.21	24.79	19.44	25.36
MnO	1.54	2.50	0.85	0.80	0.92	1.97	2.12	2.63	2.67	0.64	0.62	1.42	0.71	3.45
MgO	5.69	4.55	6.19	5.89	5.71	5.15	4.66	4.81	4.21	6.66	6.26	5.92	5.93	3.65
CaO	7.37	6.85	10.71	11.11	10.71	7.71	6.69	4.29	4.71	11.10	11.19	6.76	12.43	7.39
Na2O	0.00	0.02	0.00	0.01	0.00	0.02	0.00	0.14	0.00	0.03	0.01	0.00	0.01	0.00
K20	0.00	0.00	0.00	0.00	0.00	0.00	0.00	0.00	0.00	0.00	0.00	0.00	0.00	0.00
Total	99.69	100.28	100.89	100.58	100.40	100.64	100.30	100.61	99.83	100.57	100.26	100.49	100.77	100.31
Si	3.00	3.01	3.01	3.00	3.00	2.99	3.03	3.00	3.01	2.99	3.00	3.01	3.01	2.99
Ti	0.00	0.00	0.00	0.00	0.00	0.00	0.00	0.00	0.00	0.00	0.00	0.00	0.00	0.00
Al	2.03	2.03	2.00	2.02	2.02	2.03	2.03	2.09	2.04	2.02	2.02	2.03	2.01	2.05
Cr	0.00	0.01	0.00	0.00	0.00	0.00	0.00	0.00	0.00	0.01	0.00	0.00	0.00	0.00
Fe	1.57	1.65	1.34	1.33	1.38	1.60	1.67	1.77	1.83	1.27	1.29	1.60	1.23	1.66
Mn	0.10	0.16	0.05	0.05	0.06	0.13	0.14	0.17	0.18	0.04	0.04	0.09	0.05	0.23
Mg	0.66	0.53	0.70	0.67	0.65	0.59	0.54	0.56	0.49	0.75	0.71	0.68	0.67	0.43
Ca	0.61	0.57	0.87	0.91	0.88	0.64	0.56	0.36	0.40	0.90	0.91	0.56	1.01	0.62
Na	0.00	0.00	0.00	0.00	0.00	0.00	0.00	0.02	0.00	0.00	0.00	0.00	0.00	0.00
K	0.00	0.00	0.00	0.00	0.00	0.00	0.00	0.00	0.00	0.00	0.00	0.00	0.00	0.00
Total	7.98	7.97	7.99	7.99	7.99	7.99	7.96	7.97	7.96	7.99	7.98	7.97	7.98	7.98

Analysis ID format = (sample number, mineral abbreviation _ probe session, grain number and number of spot on grain)

Table A.1: Garnet (continued)

Analysis ID	158g_d2	158g_d3.1	158g_d3.2	158g_d3.3	158g_d3.4	158g_d3.5	158g_d3.6	158g_d4
area probed in garnet	core	core	inter	inter	rim	inter	rim	core
SiO2	38.21	39.41	39.60	39.04	38.36	39.20	38.28	38.35
TiO2	0.02	0.06	0.03	0.03	0.00	0.06	0.01	0.04
Al2O3	21.98	21.63	21.50	21.53	21.12	21.67	20.96	21.48
Cr2O3	0.03	0.00	0.04	0.05	0.02	0.00	0.00	0.00
FeO	26.89	18.18	18.44	20.27	26.40	18.40	25.14	24.90
MnO	3.90	0.54	0.66	0.82	3.40	0.68	3.00	2.15
MgO	3.90	6.70	6.12	5.55	3.40	6.21	3.66	4.04
CaO	5.70	12.71	12.81	12.76	7.03	13.20	8.32	9.05
Na2O	0.02	0.01	0.02	0.00	0.02	0.00	0.00	0.00
K20	0.00	0.00	0.00	0.00	0.00	0.00	0.00	0.00
Total	100.65	99.24	99.22	100.05	99.76	99.42	99.37	100.01
Si	3.00	3.02	3.04	3.01	3.04	3.01	3.03	3.01
Ti	0.00	0.00	0.00	0.00	0.00	0.00	0.00	0.00
Al	2.03	1.96	1.95	1.95	1.97	1.96	1.96	1.98
Cr	0.00	0.00	0.00	0.00	0.00	0.00	0.00	0.00
Fe	1.76	1.17	1.19	1.31	1.75	1.18	1.66	1.63
Mn	0.26	0.04	0.04	0.05	0.23	0.04	0.20	0.14
Mg	0.46	0.77	0.70	0.64	0.40	0.71	0.43	0.47
Ca	0.48	1.04	1.05	1.05	0.60	1.09	0.71	0.76
Na	0.00	0.00	0.00	0.00	0.00	0.00	0.00	0.00
K	0.00	0.00	0.00	0.00	0.00	0.00	0.00	0.00
Total	7.99	8.00	7.98	8.01	7.98	8.00	7.99	8.00

Analysis ID format = (sample number, mineral abbreviation _ probe session, grain number and number of spot on grain)

Table A.2: Biotite

Analysis ID	73bi_d1	73bi_d2.1	73bi_d2.2	73bi_d2.3	73bi_d4	73bi_d5	73bi_d6	73bi_d7.1	73bi_d7.2	73bi_d8	73bi_d9.1	73bi_d9.2	77bi_a1	77bi_a2	77bi_b1
area probed in sample	GBS: core	GBS: rim	GBS: inter	GBS: core	matrix	GBS: rim	matrix	GBS: rim	matrix	matrix	matrix	matrix	matrix	matrix	matrix
SiO2	35.55	35.60	35.66	35.78	35.96	35.59	36.13	34.63	35.48	35.25	35.53	35.24	35.18	35.01	35.30
TiO2	2.79	2.86	2.82	2.94	2.97	2.86	2.75	2.85	2.81	2.73	2.92	2.91	2.33	2.48	2.42
Al2O3	20.19	20.92	20.83	20.72	20.64	20.71	20.54	20.50	20.53	20.36	20.21	20.22	20.70	20.45	20.30
Cr2O3	0.02	0.05	0.04	0.06	0.04	0.02	0.02	0.07	0.08	0.05	0.11	0.11	0.06	0.04	0.04
FeO	22.06	21.99	21.97	21.85	21.75	21.39	21.73	21.39	21.29	21.32	22.07	21.19	20.23	21.54	21.60
MnO	0.14	0.11	0.08	0.12	0.12	0.07	0.10	0.14	0.09	0.09	0.03	0.07	0.11	0.12	0.05
MgO	8.12	8.39	8.13	8.27	8.14	8.24	8.11	8.07	8.07	7.86	7.87	7.90	8.19	7.62	7.70
CaO	0.00	0.00	0.00	0.00	0.00	0.00	0.02	0.01	0.02	0.00	0.00	0.00	0.00	0.00	0.00
Na2O	0.33	0.20	0.19	0.20	0.20	0.29	0.28	0.38	0.24	0.26	0.20	0.31	0.23	0.27	0.28
K20	9.30	9.57	9.60	9.93	9.94	9.57	9.48	9.81	9.89	10.09	10.05	9.84	9.15	8.86	9.88
Total	98.49	99.69	99.33	99.87	99.76	98.74	99.16	97.85	98.48	98.01	99.00	97.79	96.18	96.40	97.57
Si	2.64	2.61	2.63	2.63	2.64	2.63	2.66	2.60	2.64	2.64	2.64	2.64	2.65	2.65	2.65
Ti	0.16	0.16	0.16	0.16	0.16	0.16	0.15	0.16	0.16	0.15	0.16	0.16	0.13	0.14	0.14
Al	1.77	1.81	1.81	1.79	1.79	1.81	1.78	1.81	1.80	1.80	1.77	1.78	1.84	1.82	1.80
Cr	0.00	0.00	0.00	0.00	0.00	0.00	0.00	0.00	0.00	0.00	0.01	0.01	0.00	0.00	0.00
Fe	1.37	1.35	1.35	1.34	1.33	1.32	1.34	1.34	1.32	1.33	1.37	1.33	1.28	1.36	1.36
Mn	0.01	0.01	0.01	0.01	0.01	0.00	0.01	0.01	0.01	0.01	0.00	0.00	0.01	0.01	0.00
Mg	0.90	0.92	0.89	0.90	0.89	0.91	0.89	0.90	0.89	0.88	0.87	0.88	0.92	0.86	0.86
Ca	0.00	0.00	0.00	0.00	0.00	0.00	0.00	0.00	0.00	0.00	0.00	0.00	0.00	0.00	0.00
Na	0.05	0.03	0.03	0.03	0.03	0.04	0.04	0.06	0.03	0.04	0.03	0.04	0.03	0.04	0.04
K	0.88	0.90	0.90	0.93	0.93	0.90	0.89	0.94	0.94	0.96	0.95	0.94	0.88	0.86	0.95
Total	7.78	7.78	7.78	7.79	7.78	7.78	7.76	7.83	7.79	7.81	7.80	7.79	7.75	7.74	7.80

Analysis ID format = (sample number, mineral abbreviation _ probe session, grain number and number of spot on grain)

Table A.2: Biotite (continued)

Analysis ID	77bi_b2	77bi_b3	77bi_b4	77bi_b5	77bi_b6	77bi_b7	77bi_b8	77bi_b9	77bi_b10	77bi_b11	77bi_b12	77bi_b13	77bi_b14	77bi_b15	77bi_b16
area probed in sample	matrix	matrix	matrix	matrix	matrix	matrix	matrix	matrix	matrix	matrix	matrix	matrix	matrix	matrix	matrix
SiO2	35.44	35.62	35.55	35.77	35.62	35.67	35.43	35.38	35.80	35.89	35.36	35.88	35.61	35.11	35.49
TiO2	2.46	2.43	2.38	2.37	2.46	2.50	2.49	2.52	2.47	2.48	2.46	2.51	2.56	2.36	2.47
Al2O3	20.44	20.49	20.70	20.43	20.67	20.72	21.09	20.94	20.86	20.52	20.66	20.60	20.48	20.52	21.05
Cr2O3	0.04	0.06	0.05	0.05	0.02	0.02	0.02	0.07	0.06	0.04	0.05	0.03	0.01	0.03	0.10
FeO	21.57	21.28	21.55	21.57	21.39	21.49	21.56	21.62	21.57	21.61	21.89	21.70	21.32	21.36	21.80
MnO	0.08	0.11	0.04	0.12	0.10	0.05	0.13	0.05	0.10	0.04	0.11	0.09	0.13	0.02	0.13
MgO	7.75	7.87	7.87	7.65	7.86	7.86	7.83	7.73	7.99	7.88	7.84	7.74	7.78	8.02	8.02
CaO	0.00	0.00	0.00	0.16	0.00	0.00	0.00	0.00	0.00	0.00	0.00	0.00	0.00	0.00	0.00
Na2O	0.26	0.26	0.21	0.27	0.23	0.25	0.25	0.25	0.33	0.24	0.23	0.27	0.24	0.29	0.25
K20	9.54	9.40	9.24	8.95	9.29	9.76	9.86	9.86	9.88	9.28	9.59	9.43	9.37	9.38	9.28
Total	97.58	97.52	97.59	97.35	97.63	98.32	98.66	98.41	99.07	97.98	98.19	98.25	97.51	97.09	98.59
Si	2.66	2.66	2.66	2.68	2.66	2.65	2.63	2.63	2.64	2.67	2.64	2.67	2.66	2.64	2.63
Ti	0.14	0.14	0.13	0.13	0.14	0.14	0.14	0.14	0.14	0.14	0.14	0.14	0.14	0.13	0.14
Al	1.81	1.81	1.82	1.80	1.82	1.82	1.84	1.84	1.82	1.80	1.82	1.80	1.81	1.82	1.84
Cr	0.00	0.00	0.00	0.00	0.00	0.00	0.00	0.00	0.00	0.00	0.00	0.00	0.00	0.00	0.01
Fe	1.35	1.33	1.35	1.35	1.34	1.34	1.34	1.35	1.33	1.34	1.37	1.35	1.33	1.34	1.35
Mn	0.01	0.01	0.00	0.01	0.01	0.00	0.01	0.00	0.01	0.00	0.01	0.01	0.01	0.00	0.01
Mg	0.87	0.88	0.88	0.85	0.87	0.87	0.87	0.86	0.88	0.87	0.87	0.86	0.87	0.90	0.89
Ca	0.00	0.00	0.00	0.01	0.00	0.00	0.00	0.00	0.00	0.00	0.00	0.00	0.00	0.00	0.00
Na	0.04	0.04	0.03	0.04	0.03	0.04	0.04	0.04	0.05	0.03	0.03	0.04	0.04	0.04	0.04
K	0.91	0.90	0.88	0.85	0.88	0.93	0.93	0.94	0.93	0.88	0.91	0.89	0.89	0.90	0.88
Total	7.78	7.76	7.75	7.73	7.75	7.78	7.79	7.79	7.80	7.75	7.79	7.76	7.75	7.78	7.77

Analysis ID format = (sample number, mineral abbreviation _ probe session, grain number and number of spot on grain)

Table A.2: Biotite (continued)

Analysis ID	101bi_c1	101bi_c2.1	152bi_c1	152bi_c3	152bi_c4	152bi_c5	152bi_c6	152bi_c7.1	152bi_c7.2	152bi_c7.3	158bi_d1.1	158bi_d1.2	158bi_d1.3	158bi_d4.1	158bi_d4.2
area probed in sample	matrix	matrix	inclusion	matrix	matrix	matrix	matrix	GBS: rim	GBS: core	GBS: rim	core	inter	rim	matrix	matrix
SiO2	36.66	36.90	38.55	37.94	37.54	37.89	37.57	37.79	37.67	37.65	38.11	37.97	37.62	38.10	37.64
TiO2	4.13	3.52	0.63	2.54	2.34	2.37	2.66	2.70	2.73	2.73	3.36	3.19	3.17	2.96	2.94
Al2O3	16.08	16.15	18.58	17.08	17.08	17.22	16.92	17.14	16.99	17.09	16.17	15.99	16.11	15.86	15.96
Cr2O3	0.02	0.03	0.07	0.14	0.07	0.11	0.16	0.09	0.10	0.08	0.11	0.10	0.09	0.07	0.04
FeO	20.12	18.34	11.09	14.61	14.39	14.44	14.49	15.01	14.79	14.87	17.63	17.64	17.46	17.34	17.35
MnO	0.10	0.02	0.10	0.15	0.12	0.09	0.05	0.11	0.08	0.13	0.15	0.13	0.09	0.09	0.08
MgO	11.10	12.26	18.70	15.02	15.20	14.90	14.97	14.73	14.51	14.94	13.10	13.04	13.42	13.56	13.56
CaO	0.11	0.00	0.15	0.02	0.06	0.12	0.00	0.00	0.07	0.08	0.01	0.01	0.02	0.00	0.01
Na2O	0.25	0.16	0.41	0.29	0.35	0.31	0.27	0.26	0.28	0.27	0.17	0.18	0.22	0.27	0.27
K20	9.88	9.43	7.85	8.41	8.47	8.33	8.30	8.96	8.80	8.93	9.28	9.59	9.48	8.89	8.75
Total	98.45	96.82	96.13	96.19	95.61	95.79	95.40	96.79	96.03	96.78	98.10	97.84	97.68	97.14	96.60
Si	2.72	2.75	2.76	2.77	2.76	2.78	2.77	2.76	2.77	2.75	2.79	2.79	2.77	2.80	2.79
Ti	0.23	0.20	0.03	0.14	0.13	0.13	0.15	0.15	0.15	0.15	0.18	0.18	0.18	0.16	0.16
Al	1.41	1.42	1.57	1.47	1.48	1.49	1.47	1.48	1.47	1.47	1.39	1.38	1.40	1.38	1.39
Cr	0.00	0.00	0.00	0.01	0.00	0.01	0.01	0.01	0.01	0.00	0.01	0.01	0.01	0.00	0.00
Fe	1.25	1.14	0.66	0.89	0.89	0.89	0.89	0.92	0.91	0.91	1.08	1.08	1.07	1.07	1.07
Mn	0.01	0.00	0.01	0.01	0.01	0.01	0.00	0.01	0.01	0.01	0.01	0.01	0.01	0.01	0.01
Mg	1.23	1.36	1.99	1.64	1.67	1.63	1.64	1.60	1.59	1.63	1.43	1.43	1.47	1.49	1.50
Ca	0.01	0.00	0.01	0.00	0.00	0.01	0.00	0.00	0.01	0.01	0.00	0.00	0.00	0.00	0.00
Na	0.04	0.02	0.06	0.04	0.05	0.04	0.04	0.04	0.04	0.04	0.02	0.03	0.03	0.04	0.04
K	0.94	0.90	0.72	0.78	0.80	0.78	0.78	0.83	0.83	0.83	0.87	0.90	0.89	0.83	0.83
Total	7.83	7.80	7.81	7.76	7.79	7.76	7.75	7.79	7.77	7.80	7.77	7.80	7.82	7.78	7.79

Analysis ID format = (sample number, mineral abbreviation _ probe session, grain number and number of spot on grain)

Table A.3: Plagioclase

Analysis ID	73pl_d1	73pl_d2.1	73pl_d2.2	73pl_d3	73pl_d4	73pl_d5	77pl_a1	77pl_b1	77pl_b2	77pl_b3	77pl_b4	77pl_b5	77pl_b6	101pl_c1.1	101pl_c1.2
area probed in sample	matrix	GBS	GBS	GBS	matrix	matrix	matrix	GBS	matrix	matrix	matrix	matrix	GBS	matrix	matrix
SiO2	62.32	61.86	61.97	62.22	62.86	61.98	62.54	61.87	62.18	61.65	62.72	62.89	62.48	44.94	45.81
TiO2	0.00	0.00	0.00	0.00	0.01	0.03	0.00	0.01	0.00	0.00	0.02	0.00	0.02	0.00	0.00
Al2O3	25.20	25.06	24.73	24.95	23.64	24.24	24.72	24.97	24.88	25.39	24.61	24.51	24.95	36.44	35.75
Cr2O3	0.00	0.00	0.00	0.00	0.00	0.00	0.00	0.00	0.00	0.00	0.00	0.00	0.00	0.00	0.00
FeO	0.03	0.04	0.19	0.10	0.03	0.17	0.11	0.06	0.09	0.04	0.05	0.02	0.00	0.11	0.13
MnO	0.01	0.05	0.03	0.08	0.03	0.01	0.03	0.07	0.00	0.02	0.00	0.02	0.02	0.06	0.02
MgO	0.00	0.00	0.01	0.00	0.00	0.00	0.00	0.00	0.00	0.00	0.00	0.01	0.02	0.00	0.00
CaO	5.21	5.39	5.15	5.49	4.81	5.19	4.99	5.40	5.21	5.64	4.96	4.98	5.30	18.39	17.48
Na2O	8.00	8.20	8.07	7.87	8.09	7.86	7.51	7.56	8.07	7.73	7.84	7.98	7.89	0.74	1.03
K20	0.12	0.10	0.10	0.11	0.16	0.11	0.09	0.16	0.18	0.20	0.22	0.18	0.19	0.03	0.07
Total	100.89	100.70	100.25	100.82	99.62	99.58	99.99	100.10	100.60	100.68	100.42	100.59	100.87	100.72	100.29
Si	2.73	2.72	2.74	2.73	2.78	2.75	2.76	2.73	2.73	2.71	2.76	2.76	2.74	2.06	2.10
Ti	0.00	0.00	0.00	0.00	0.00	0.00	0.00	0.00	0.00	0.00	0.00	0.00	0.00	0.00	0.00
Al	1.30	1.30	1.29	1.29	1.23	1.27	1.28	1.30	1.29	1.32	1.27	1.27	1.29	1.96	1.93
Cr	0.00	0.00	0.00	0.00	0.00	0.00	0.00	0.00	0.00	0.00	0.00	0.00	0.00	0.00	0.00
Fe	0.00	0.00	0.01	0.00	0.00	0.01	0.00	0.00	0.00	0.00	0.00	0.00	0.00	0.00	0.01
Mn	0.00	0.00	0.00	0.00	0.00	0.00	0.00	0.00	0.00	0.00	0.00	0.00	0.00	0.00	0.00
Mg	0.00	0.00	0.00	0.00	0.00	0.00	0.00	0.00	0.00	0.00	0.00	0.00	0.00	0.00	0.00
Ca	0.24	0.25	0.24	0.26	0.23	0.25	0.24	0.26	0.25	0.27	0.23	0.23	0.25	0.90	0.86
Na	0.68	0.70	0.69	0.67	0.69	0.68	0.64	0.65	0.69	0.66	0.67	0.68	0.67	0.07	0.09
K	0.01	0.01	0.01	0.01	0.01	0.01	0.01	0.01	0.01	0.01	0.01	0.01	0.01	0.00	0.00
Total	4.96	4.98	4.97	4.96	4.95	4.96	4.93	4.95	4.97	4.97	4.95	4.95	4.96	5.00	4.99

Analysis ID format = (sample number, mineral abbreviation _ probe session, grain number and number of spot on grain)

Table A.3: Plagioclase (continued)

Analysis ID	101pl_c2.2	101pl_c3	116pl_d1.1	116pl_d1.2	116pl_d2	116pl_d3	152pl_b1	152pl_b2	152pl_b3	152pl_b4	152pl_b5	152pl_c1	152pl_c2	152pl_c3
area probed in sample	GBS	matrix	matrix	matrix	GBS	GBS	matrix	matrix	matrix	matrix	matrix	matrix	GBS (rim)	GBS (core)
SiO2	45.52	45.26	59.49	58.76	59.47	59.42	59.01	62.35	59.89	61.05	59.03	59.24	53.12	52.24
TiO2	0.00	0.00	0.01	0.02	0.02	0.03	0.03	0.01	0.02	0.00	0.00	0.00	0.02	0.00
Al2O3	35.85	35.82	25.20	25.86	25.51	25.01	27.11	24.65	26.77	25.59	27.25	26.69	30.91	31.51
Cr2O3	0.00	0.00	0.00	0.00	0.00	0.00	0.00	0.00	0.00	0.00	0.00	0.00	0.00	0.00
FeO	0.18	0.05	0.03	0.18	0.04	0.09	0.00	0.05	0.02	0.01	0.08	0.02	0.16	0.11
MnO	0.00	0.03	0.00	0.05	0.05	0.06	0.08	0.06	0.00	0.01	0.07	0.05	0.05	0.02
MgO	0.00	0.03	0.00	0.01	0.00	0.00	0.01	0.00	0.00	0.02	0.00	0.00	0.00	0.02
CaO	18.26	18.69	9.22	9.13	9.22	9.17	7.46	4.94	6.81	5.78	7.49	7.57	12.50	12.91
Na2O	1.00	0.83	5.51	5.74	5.58	5.60	6.69	7.72	6.89	7.44	6.56	6.61	4.11	3.87
K20	0.02	0.00	0.21	0.20	0.20	0.22	0.08	0.18	0.12	0.12	0.09	0.09	0.08	0.05
Total	100.83	100.71	99.67	99.96	100.10	99.60	100.47	99.96	100.53	100.02	100.56	100.28	100.95	100.74
Si	2.08	2.07	2.66	2.63	2.65	2.66	2.61	2.75	2.64	2.70	2.61	2.63	2.38	2.35
Ti	0.00	0.00	0.00	0.00	0.00	0.00	0.00	0.00	0.00	0.00	0.00	0.00	0.00	0.00
Al	1.93	1.93	1.33	1.36	1.34	1.32	1.42	1.28	1.39	1.33	1.42	1.40	1.63	1.67
Cr	0.00	0.00	0.00	0.00	0.00	0.00	0.00	0.00	0.00	0.00	0.00	0.00	0.00	0.00
Fe	0.01	0.00	0.00	0.01	0.00	0.00	0.00	0.00	0.00	0.00	0.00	0.00	0.01	0.00
Mn	0.00	0.00	0.00	0.00	0.00	0.00	0.00	0.00	0.00	0.00	0.00	0.00	0.00	0.00
Mg	0.00	0.00	0.00	0.00	0.00	0.00	0.00	0.00	0.00	0.00	0.00	0.00	0.00	0.00
Ca	0.89	0.92	0.44	0.44	0.44	0.44	0.35	0.23	0.32	0.27	0.36	0.36	0.60	0.62
Na	0.09	0.07	0.48	0.50	0.48	0.49	0.57	0.66	0.59	0.64	0.56	0.57	0.36	0.34
K	0.00	0.00	0.01	0.01	0.01	0.01	0.00	0.01	0.01	0.01	0.01	0.01	0.00	0.00
Total	5.00	5.00	4.92	4.95	4.93	4.93	4.97	4.94	4.96	4.95	4.96	4.96	4.98	4.99

Analysis ID format = (sample number, mineral abbreviation _ probe session, grain number and number of spot on grain)

Table A.3: Plagioclase (continued)

Analysis ID	152pl_c5	152pl_c6.1	152pl_c6.2	152pl_c6.3	152pl_c6.5	152pl_c7.1	152pl_c7.2	152pl_c7.4	152pl_c11	158pl_d1	158pl_d2.1	158pl_d2.2	158pl_d3	158pl_d4.1
area probed in sample	GBS (rim)	GBS (rim)	GBS (inter)	GBS (core)	GBS (rim)	GBS (rim)	GBS (core)	GBS (rim)	matrix	matrix	GBS	matrix	matrix	GBS
SiO2	50.46	51.02	52.46	52.03	57.34	51.93	52.54	53.26	59.99	45.00	46.00	46.06	45.67	45.33
TiO2	0.01	0.04	0.01	0.00	0.03	0.00	0.00	0.06	0.00	0.01	0.00	0.02	0.00	0.02
Al2O3	32.37	32.12	30.78	31.65	28.02	30.82	30.93	30.74	26.31	35.83	35.13	35.03	35.31	34.34
Cr2O3	0.00	0.00	0.00	0.00	0.00	0.00	0.00	0.00	0.00	0.00	0.00	0.00	0.00	0.00
FeO	0.29	0.32	0.14	0.13	0.10	0.06	0.09	0.12	0.03	0.13	0.30	0.07	0.32	0.05
MnO	0.04	0.05	0.05	0.01	0.03	0.06	0.06	0.00	0.04	0.03	0.07	0.04	0.05	0.02
MgO	0.02	0.00	0.00	0.04	0.01	0.01	0.00	0.00	0.00	0.00	0.00	0.00	0.04	0.00
CaO	13.98	13.37	12.25	12.71	8.89	12.69	12.85	12.08	7.12	18.11	17.75	17.75	17.83	18.59
Na2O	3.03	3.35	4.05	3.77	6.11	3.99	4.05	4.40	7.24	0.59	0.96	0.94	0.78	0.70
K20	0.08	0.03	0.04	0.03	0.07	0.04	0.04	0.07	0.10	0.00	0.00	0.00	0.25	0.01
Total	100.27	100.28	99.78	100.37	100.60	99.59	100.56	100.72	100.83	99.69	100.21	99.91	100.25	99.07
Si	2.29	2.31	2.38	2.35	2.55	2.36	2.37	2.39	2.65	2.08	2.11	2.12	2.10	2.11
Ti	0.00	0.00	0.00	0.00	0.00	0.00	0.00	0.00	0.00	0.00	0.00	0.00	0.00	0.00
Al	1.73	1.71	1.64	1.68	1.47	1.65	1.64	1.63	1.37	1.95	1.90	1.90	1.91	1.88
Cr	0.00	0.00	0.00	0.00	0.00	0.00	0.00	0.00	0.00	0.00	0.00	0.00	0.00	0.00
Fe	0.01	0.01	0.01	0.01	0.00	0.00	0.00	0.00	0.00	0.00	0.01	0.00	0.01	0.00
Mn	0.00	0.00	0.00	0.00	0.00	0.00	0.00	0.00	0.00	0.00	0.00	0.00	0.00	0.00
Mg	0.00	0.00	0.00	0.00	0.00	0.00	0.00	0.00	0.00	0.00	0.00	0.00	0.00	0.00
Ca	0.68	0.65	0.59	0.61	0.42	0.62	0.62	0.58	0.34	0.89	0.87	0.87	0.88	0.93
Na	0.27	0.29	0.36	0.33	0.53	0.35	0.35	0.38	0.62	0.05	0.09	0.08	0.07	0.06
K	0.00	0.00	0.00	0.00	0.00	0.00	0.00	0.00	0.01	0.00	0.00	0.00	0.01	0.00
Total	4.98	4.98	4.98	4.98	4.98	4.99	4.99	4.99	4.98	4.98	4.98	4.98	4.99	4.98

Analysis ID format = (sample number, mineral abbreviation _ probe session, grain number and number of spot on grain)

Table A.4: Amphiboles

Analysis ID	101hb_c1.1	101hb_c1.2	101hb_c2.2	101hb_c3.1	101hb_c3.2	101hb_c3.3	101hb_c3.4	101hb_c4.1	101hb_c4.2	101hb_c4.4	116hb_d1.1	116hb_d2.1	116hb_d2.2
area probed in sample	rim	core	rim	core	inter	inter	rim	inclusion	core	inter	symplectite	GBS (core)	GBS (rim)
SiO2	45.78	43.34	45.49	44.77	44.95	45.39	45.57	44.89	44.05	44.35	46.75	42.34	42.93
TiO2	1.19	1.56	1.20	1.44	1.40	1.44	1.33	1.55	1.55	1.61	1.23	1.26	1.10
Al2O3	11.31	13.35	11.30	12.59	12.15	11.56	11.76	12.06	13.01	12.90	7.84	12.29	11.59
Cr2O3	0.00	0.01	0.00	0.03	0.03	0.02	0.05	0.02	0.03	0.02	0.06	0.02	0
FeO	16.99	17.55	17.74	17.57	17.06	18.40	17.50	18.61	17.63	17.60	18.87	21.62	21.17
MnO	0.17	0.24	0.21	0.19	0.18	0.20	0.17	0.21	0.25	0.29	0.29	0.33	0.41
MgO	10.15	9.30	10.29	9.70	10.07	10.35	10.30	10.12	9.31	9.23	9.47	6.81	7.26
CaO	12.35	11.50	11.49	11.63	11.82	10.84	11.14	10.55	11.67	11.79	12.17	11.69	11.56
Na2O	0.68	0.95	0.71	0.90	0.84	0.77	0.63	0.96	1.01	0.84	0.63	1.21	1.33
K20	0.49	0.72	0.50	0.61	0.50	0.51	0.46	0.69	0.75	0.65	0.60	1.09	0.91
Total	99.11	98.53	98.93	99.43	99.00	99.48	98.91	99.64	99.25	99.28	97.91	98.67	98.26
Si	6.71	6.43	6.69	6.56	6.60	6.65	6.68	6.58	6.48	6.52	7.01	6.44	6.53
Ti	0.13	0.17	0.13	0.16	0.15	0.16	0.15	0.17	0.17	0.18	0.14	0.14	0.13
Al	1.95	2.33	1.96	2.17	2.10	1.99	2.03	2.08	2.26	2.23	1.38	2.20	2.08
Cr	0.00	0.00	0.00	0.00	0.00	0.00	0.01	0.00	0.00	0.00	0.01	0.00	0.00
Fe	2.08	2.18	2.18	2.15	2.09	2.25	2.14	2.28	2.17	2.16	2.37	2.75	2.69
Mn	0.02	0.03	0.03	0.02	0.02	0.03	0.02	0.03	0.03	0.04	0.04	0.04	0.05
Mg	2.22	2.06	2.26	2.12	2.20	2.26	2.25	2.21	2.04	2.02	2.12	1.54	1.65
Ca	1.94	1.83	1.81	1.83	1.86	1.70	1.75	1.66	1.84	1.86	1.95	1.90	1.88
Na	0.19	0.27	0.20	0.25	0.24	0.22	0.18	0.27	0.29	0.24	0.18	0.36	0.39
K	0.09	0.14	0.09	0.11	0.09	0.10	0.09	0.13	0.14	0.12	0.11	0.21	0.18
Total	15.33	15.44	15.35	15.38	15.36	15.35	15.29	15.41	15.43	15.37	15.31	15.60	15.59

Analysis ID format = (sample number, mineral abbreviation _ probe session, grain number and number of spot on grain). Hb = hornblende.

Table A.4: Amphiboles (continued)

Analysis ID	116hb_d3	116hb_d4	116hb_d5	116hb_d6.1	116hb_d6.2	158hb_d1.1	158hb_d1.2	158hb_d2.1	158hb_d2.2	158hb_d3
area probed in sample	GBS (core)	GBS (rim)	matrix	matrix	matrix	core	rim	core	rim	rim
SiO2	41.93	42.52	42.41	42.52	42.69	42.72	43.17	42.44	43.00	42.36
TiO2	1.23	1.43	2.04	2.01	1.70	1.49	1.47	1.36	1.49	1.65
Al2O3	12.16	11.56	11.21	10.90	11.02	14.64	14.03	14.49	14.20	14.36
Cr2O3	0.00	0.00	0.00	0.02	0.00	0.04	0.00	0.00	0.03	0.06
FeO	21.77	21.40	21.54	20.71	20.78	16.31	15.67	15.81	15.52	15.65
MnO	0.37	0.28	0.26	0.33	0.30	0.21	0.36	0.38	0.31	0.39
MgO	6.49	6.95	6.80	6.98	6.79	9.46	9.87	9.59	9.80	9.46
CaO	11.98	12.02	12.16	11.99	11.99	10.13	11.41	11.72	11.87	11.55
Na2O	1.23	1.11	1.19	1.17	1.05	0.74	0.88	0.86	1.02	1.01
K20	1.09	1.05	1.06	1.01	1.01	0.97	0.79	1.09	0.74	0.83
Total	98.25	98.32	98.67	97.64	97.33	96.71	97.64	97.75	97.97	97.33
Si	6.42	6.49	6.46	6.52	6.56	6.39	6.40	6.32	6.36	6.32
Ti	0.14	0.16	0.23	0.23	0.20	0.17	0.16	0.15	0.17	0.19
Al	2.20	2.08	2.01	1.97	2.00	2.58	2.45	2.54	2.48	2.53
Cr	0.00	0.00	0.00	0.00	0.00	0.00	0.00	0.00	0.00	0.01
Fe	2.79	2.73	2.75	2.66	2.67	2.04	1.94	1.97	1.92	1.95
Mn	0.05	0.04	0.03	0.04	0.04	0.03	0.04	0.05	0.04	0.05
Mg	1.48	1.58	1.54	1.60	1.56	2.11	2.18	2.13	2.16	2.11
Ca	1.97	1.96	1.99	1.97	1.97	1.62	1.81	1.87	1.88	1.85
Na	0.36	0.33	0.35	0.35	0.31	0.21	0.25	0.25	0.29	0.29
K	0.21	0.20	0.21	0.20	0.20	0.19	0.15	0.21	0.14	0.16
Total	15.63	15.58	15.57	15.53	15.50	15.35	15.41	15.49	15.45	15.45

Analysis ID format = (sample number, mineral abbreviation _ probe session, grain number and number of spot on grain). Hb = hornblende.

Table A.4: Amphiboles (continued)

Analysis ID	101cu_c1	101cu_c2	152cu_a1	158cu_d2	158cu_d3	158cu_d4
area probed in sample	matrix	matrix	matrix	matrix	matrix	matrix
SiO2	53.67	53.61	54.97	53.87	54.52	53.92
TiO2	0.04	0.10	0.08	0.09	0.00	0.06
Al2O3	0.65	1.13	1.04	1.00	0.47	0.81
Cr2O3	0.01	0.00	0.06	0.01	0.02	0.00
FeO	26.77	27.46	22.84	24.48	24.51	24.58
MnO	0.52	0.61	0.72	0.93	1.01	0.76
MgO	15.80	15.31	19.19	17.26	17.19	16.92
CaO	0.95	0.90	0.66	1.09	0.73	0.83
Na2O	0.04	0.02	0.04	0.11	0.00	0.07
K20	0.00	0.00	0.01	0.03	0.00	0.03
Total	98.45	99.13	99.63	98.87	98.45	97.99
Si	7.91	7.87	7.85	7.84	7.95	7.91
Ti	0.00	0.01	0.01	0.01	0.00	0.01
Al	0.11	0.19	0.18	0.17	0.08	0.14
Cr	0.00	0.00	0.01	0.00	0.00	0.00
Fe	3.30	3.37	2.73	2.98	2.99	3.02
Mn	0.06	0.08	0.09	0.11	0.12	0.09
Mg	3.47	3.35	4.09	3.75	3.74	3.70
Ca	0.15	0.14	0.10	0.17	0.11	0.13
Na	0.01	0.01	0.01	0.03	0.00	0.02
K	0.00	0.00	0.00	0.00	0.00	0.00
Total	15.03	15.02	15.06	15.08	15.00	15.02

Analysis ID format = (sample number, mineral abbreviation _ probe session, grain number and number of spot on grain). Cu = cummingtonite

Table A.5: Clinopyroxenes and oxides

Analysis ID	116cpx_e1.1	116cpx_e1.4	116cpx_e1.5	116cpx_e1.6	116cpx_e1.8	116cpx_e1.9	116cpx_e1.14	73sp_c1	73sp_c2	73sp_c3	101ilm_c1
area probed in sample	matrix	matrix	matrix	matrix	matrix	matrix	matrix	matrix	matrix	matrix	matrix
SiO2	51.59	52.82	52.99	52.60	52.27	51.84	52.56	0.01	0.00	0.00	0.00
TiO2	0.24	0.08	0.08	0.11	0.17	0.15	0.12	0.05	0.06	0.03	52.18
Al2O3	1.83	0.43	0.67	0.84	1.26	1.58	0.92	54.39	53.42	53.69	0.00
Cr2O3	0.02	0.00	0.03	0.04	0.00	0.00	0.02	0.38	0.76	0.55	0.00
FeO	13.70	11.95	12.32	12.52	13.36	13.37	12.86	15.31	14.30	15.30	46.22
MnO	0.37	0.38	0.36	0.41	0.33	0.36	0.41	0.13	0.19	0.17	0.64
MgO	11.37	11.33	11.50	11.36	11.26	11.27	11.37	1.37	1.22	1.36	0.41
CaO	19.84	21.66	21.27	21.08	20.17	19.90	21.38	0.00	0.00	0.01	0.10
Na2O	0.31	0.13	0.22	0.23	0.22	0.26	0.24	1.17	1.25	0.95	0.00
K20	0.06	0.00	0.00	0.00	0.02	0.07	0.03	0.00	0.04	0.00	0.00
Total	99.32	98.78	99.45	99.20	99.06	98.81	99.90	72.81	71.24	72.07	99.55
Si	1.97	2.02	2.01	2.00	2.00	1.99	1.99	0.00	0.00	0.00	0.00
Ti	0.01	0.00	0.00	0.00	0.00	0.00	0.00	0.00	0.00	0.00	0.99
Al	0.08	0.02	0.03	0.04	0.06	0.07	0.04	2.27	2.28	2.27	0.00
Cr	0.00	0.00	0.00	0.00	0.00	0.00	0.00	0.01	0.02	0.02	0.00
Fe	0.44	0.38	0.39	0.40	0.43	0.43	0.41	0.45	0.43	0.46	0.98
Mn	0.01	0.01	0.01	0.01	0.01	0.01	0.01	0.00	0.01	0.01	0.01
Mg	0.65	0.65	0.65	0.65	0.64	0.64	0.64	0.07	0.07	0.07	0.02
Ca	0.81	0.89	0.86	0.86	0.83	0.82	0.87	0.00	0.00	0.00	0.00
Na	0.02	0.01	0.02	0.02	0.02	0.02	0.02	0.08	0.09	0.07	0.00
K	0.00	0.00	0.00	0.00	0.00	0.00	0.00	0.00	0.00	0.00	0.00
Total	3.99	3.97	3.98	3.98	3.98	3.99	3.99	2.90	2.89	2.89	2.01

Analysis ID format = (sample number, mineral abbreviation _ probe session, grain number and number of spot on grain). Sp = spinel; ilm = ilmenite.